

# Recent Advances in Non-Ti MXenes: Synthesis, Properties, and Novel Applications

Karim Khan,\* Ayesha Khan Tareen, Waqas Ahmad, Iftikhar Hussain, Mujeeb U. Chaudhry, Asif Mahmood, Muhammad Farooq Khan, Han Zhang,\* and Zhongjian Xie\*


One of the most fascinating 2D nanomaterials (NMs) ever found is various members of MXene family. Among them, the titanium-based MXenes, with more than 70% of publication-related investigations, are comparatively well studied, producing fundamental foundation for the 2D MXene family members with flexible properties, familiar with a variety of advanced novel technological applications. Nonetheless, there are still more candidates among transitional metals (TMs) that can function as MXene NMs in ways that go well beyond those that are now recognized. Systematized details of the preparations, characteristics, limitations, significant discoveries, and uses of the novel M-based MXenes (M-MXenes), where M stands for non-Ti TMs (M = Sc, V, Cr, Y, Zr, Nb, Mo, Hf, Ta, W, and Lu), are given. The exceptional qualities of the 2D non-Ti MXene outperform standard Ti-MXene in several applications. There is many advancement in top-down as well as bottom-up production of MXenes family members, which allows for exact control of the M-characteristics MXene NMs to contain cutting-edge applications. This study offers a systematic evaluation of existing research, covering everything in producing complex M-MXenes from primary limitations to the characterization and selection of their applications in accordance with their novel features. The development of double metal combinations, extension of additional metal candidates beyond group-(III–VI)B family, and subsequent development of the 2D TM carbide/TMs nitride/TM carbonitrides to 2D metal boride family are also included in this overview. The possibilities and further recommendations for the way of non-Ti MXene NMs are in the synthesis of NMs will discuss in detail in this critical evaluation.

## 1. Introduction: MXene in Brief

Generally, depending on dimensionality, a material has a variety of qualities.<sup>[1]</sup> Recently, 2D materials have received numerous scientific study research interests. The 2D materials have distinctive features that set them distinct from their bulk counterparts.<sup>[2–11]</sup> The 2D materials with high aspect ratio structure, extended lateral dimension, and an atomic/molecular thickness have been intensively explored in the materials research community in recent era. Graphene, the first invented 2D nanomaterial (NM), has demonstrated a broad range of possible novel devices applications in advanced nanotechnological world. Since the discovery of Nobel Prize awarded material, graphene (2004), a range of other novel 2D NMs, for example, MXenes, transition metal dichalcogenides (TMDs), Xenes, and 3D structure of 2D materials as metal organic frameworks (MOFs), etc., were widely discovered as functional materials for energy producing/storage, environmental protection, sensing, biomedical, catalysis, etc., applications. By now 2D materials family has over 150 members, with hundreds more expected to join by modifying transition metal (TM) components

K. Khan  
School of Electrical Engineering and Intelligentization  
Dongguan University of Technology  
Dongguan 523808, China  
E-mail: karim\_khan\_niaz@szu.edu.cn

K. Khan  
Shenzhen Nuohan Environmental and Safety Inc.  
Shenzhen 518107, China

 The ORCID identification number(s) for the author(s) of this article can be found under <https://doi.org/10.1002/adv.202303998>

© 2023 The Authors. Advanced Science published by Wiley-VCH GmbH. This is an open access article under the terms of the Creative Commons Attribution License, which permits use, distribution and reproduction in any medium, provided the original work is properly cited.

DOI: 10.1002/adv.202303998

K. Khan  
Additive Manufacturing Institute  
Shenzhen University  
Shenzhen 518060, China

K. Khan, H. Zhang  
Shenzhen Engineering Laboratory of Phosphorene and Optoelectronics  
International Collaborative Laboratory of 2D Materials for  
Optoelectronics Science and Technology of Ministry of Education  
Institute of Microscale Optoelectronics Engineering  
Shenzhen University  
Shenzhen 518060, China  
E-mail: hzhang@szu.edu.cn

A. K. Tareen  
School of Mechanical Engineering  
Dongguan University of Technology  
Dongguan 523808, China

ranging from metals, semimetals, semiconductors, and insulators.<sup>[2–4,8,12–31]</sup>

For the first time, 2D titanium carbide ( $\text{Ti}_3\text{C}_2$ ) was accidentally invented in 2011 by selective etching of Al layer of  $\text{Ti}_3\text{AlC}_2$  precursor via employing acid, like, HF, called a first member of 2D MXene NMs family.<sup>[32]</sup> Later on, further members of 2D MXenes family were discovered and now consists of all 2D transition metals (TMs) carbides (TMCs), TM nitrides (TMNs), and TM carbonitrides. Now this family consists of more than 50 members, who are experimentally investigated and the discovery of further more than 100 MXene NMs members is theoretically studied, causes it as a future biggest family of 2D materials, till date.  $\text{M}_{n+1}\text{X}_n\text{T}_x$  ( $n = 1$  to 4) is a general formula for MXene-based NMs, where M indicate early TMs (e.g., Sc, Ti, V, Cr, Hf, Zr, Nb, Mo, Ta, and so on), and X shows carbon or nitrogen,<sup>[33]</sup> and  $\text{T}_x$  (where  $x$  varies) denotes single or mixed termination groups (e.g., T = F, O, NH, S, OH, Cl, Br, Te, and Se). Mono-M elements (like,  $\text{Ti}_2\text{C}$ ,  $\text{Nb}_4\text{C}_3$ , etc.), solid solutions at least from two different “M” elements (such as  $(\text{Ti},\text{V})_3\text{C}_2$  and  $(\text{Cr},\text{V})_3\text{C}_2$ ), and ordered double-“M” elements (where one TM occupies the perimeter layers while another fills a central “M” layer) are all possible (e.g.,  $\text{Mo}_2\text{TiC}_2$ ,  $\text{Mo}_2\text{Ti}_2\text{C}_3$ , etc., where the outer “M” layers are “Mo” and the central “M” layers are “Ti”). Carbonitrides are formed by solid solutions on “X” site (Figure 1). Regarding to applications, 2D MXene NMs have raised to prominence as a next-generation NMs for the investigation of ecologically acceptable catalysis for energy storage devices, optoelectronics, electromagnetic interference shielding, biomedicine, sensors environmental technology solutions, etc., thanks to their fascinating electrical and structural features (Figure 1).

W. Ahmad

Institute of Fundamental and Frontier Sciences University of Electronic Science and Technology of China  
Chengdu 610054, China

I. Hussain

Department of Mechanical Engineering  
City University of Hong Kong  
83 Tat Chee Avenue, Kowloon 999077, Hong Kong

I. Hussain

A. J. Drexel Nanomaterials Institute and Department of Materials Science and Engineering  
Drexel University  
Philadelphia, PA 19104, USA

M. U. Chaudhry

Department of Engineering  
Durham University  
Lower Mountjoy  
South Rd, Durham DH1 3LE, UK

A. Mahmood

School of Chemical and Biomolecular Engineering  
The University of Sydney  
Sydney 2006, Australia

M. F. Khan

Department of Electrical Engineering  
Sejong University  
Seoul 05006, Republic of Korea

Z. Xie

Shenzhen Children's Hospital  
Clinical Medical College of Southern University of Science and Technology  
Shenzhen, Guangdong 518038, P. R. China  
E-mail: xiezj2022@sustech.edu.cn

In contrast to other 2D NMs mostly MXene NMs are not commonly bonded via van der Waals (vdWs) forces in their precursors. The link between MXene layers is really given by the monoatomic group 13 and 14 elements, which make up most of MAX A-layer atoms (e.g., Si, Al, and Ga). Elemental layer from MAX precursors can be removed to produce various MXene NMs. Various chemical reactivates in metallic bonds (M–A) and mixed metallic/ionic/covalent bonds (M–X) in the MAX-based precursors make this technique theoretically feasible.<sup>[35]</sup> MXenes have hydrophilic surfaces termination with hydroxyl, oxygen, and fluorine groups. They can be turned into films, devices, and coatings because of easy processing and least required stabilization.

As first  $\text{Ti}_3\text{C}_2\text{T}_x$  MXene was experimentally synthesized in 2011 by Al layers etching of  $\text{Ti}_3\text{AlC}_2$  MAX in HF-acid.<sup>[32]</sup> The resulting  $\text{Ti}_3\text{C}_2\text{T}_x$  exhibited an accordion-like composition with several layers linked together by hydrogen and vdWs bonds (Figure 2a–c).<sup>[36]</sup> The 2D  $\text{Ti}_3\text{C}_2\text{T}_x$  nanosheets (NSs) maintain the same stoichiometry of titanium (Ti) as well as carbon (C) as in bulk  $\text{Ti}_3\text{AlC}_2$  precursor while having a different shape, with surface-bound functional O, OH, and F groups (Figure 2d). Reactivity of each MAX precursor differs depends on various bonding strengths in M–A and M–X, it should be noted that the etching method of the 2D  $\text{Ti}_3\text{C}_2\text{T}_x$  NSs cannot be used as a generic method for various 2D MXene NMs.<sup>[34]</sup> Figure 2e shows the comparison of Ti- and non-Ti based MXene NMs, which clear that mostly studied 2D MXene NMs are based on Ti-MXene NMs.<sup>[37]</sup> MXene NMs' crystals have closed packed M atoms, while X atoms reside in octahedral interstitial positions, resulting in hexagonal closed packed configuration with  $P63/mmc$  space group symmetry.<sup>[38]</sup>  $\text{Ti}_3\text{C}_2$  investigation laid the groundwork for the production of  $\text{Ti}_2\text{C}$ ,  $\text{Ta}_4\text{C}_3$ , and additional 2D MXene NMs from their MAX-based predecessors, exhibiting three special kinds of potential configurations (such as  $\text{M}_2\text{X}$ ,  $\text{M}_3\text{X}_2$ , and  $\text{M}_4\text{X}_3$ ).  $\text{M}_5\text{C}_4$  was afterward introduced; boosting structural variety and getting theoretically achievable compositions are over 100, including in-plane MXene (i-MXenes) as well as out-of-plane TM atom ordered MXene (O-MXenes). When different  $\text{T}_x$  on MXene NMs surface are considered, the figure of special compositions developed by order of magnitude. MXene NMs' capacity to create carbonitrides and solid solutions implies a theoretically infinite quantity of compositions and leads in a novel period of theoretically determined atomistic formation of the 2D NMs.

Most members of 2D materials are dielectrics, semiconductors, or semimetals in nature but MXene-based NMs are mostly metallic conductors because TMs can give free electrons and function as carriers<sup>[39]</sup> (e.g., phosphorene and molybdenum disulfide). The 2D MXene NMs, especially  $\text{Ti}_3\text{C}_2\text{T}_x$  with few defects can achieve a highest conductivity of  $20\,000\text{ S cm}^{-1}$ . Furthermore, abundance of surface terminations allows them to be very hydrophilic, in contradiction of various hydrophobic 2D NMs (e.g., graphene).<sup>[40,41]</sup> Its high conductivity enables their application in current collectors, interconnects, with conductive type ink, etc. MXene NMs can be used in photothermal therapy and electrochromics because of their interband transitions and plasmon resonance peaks that widen an entire UV, visible (vis), as well as NIR bands. These plasmonic properties are chemically and electrochemically tunable. As a consequence of their large interfaces with electromagnetic waves at frequencies range from tera-to-giga hertz, they are applicable in electromagnetic

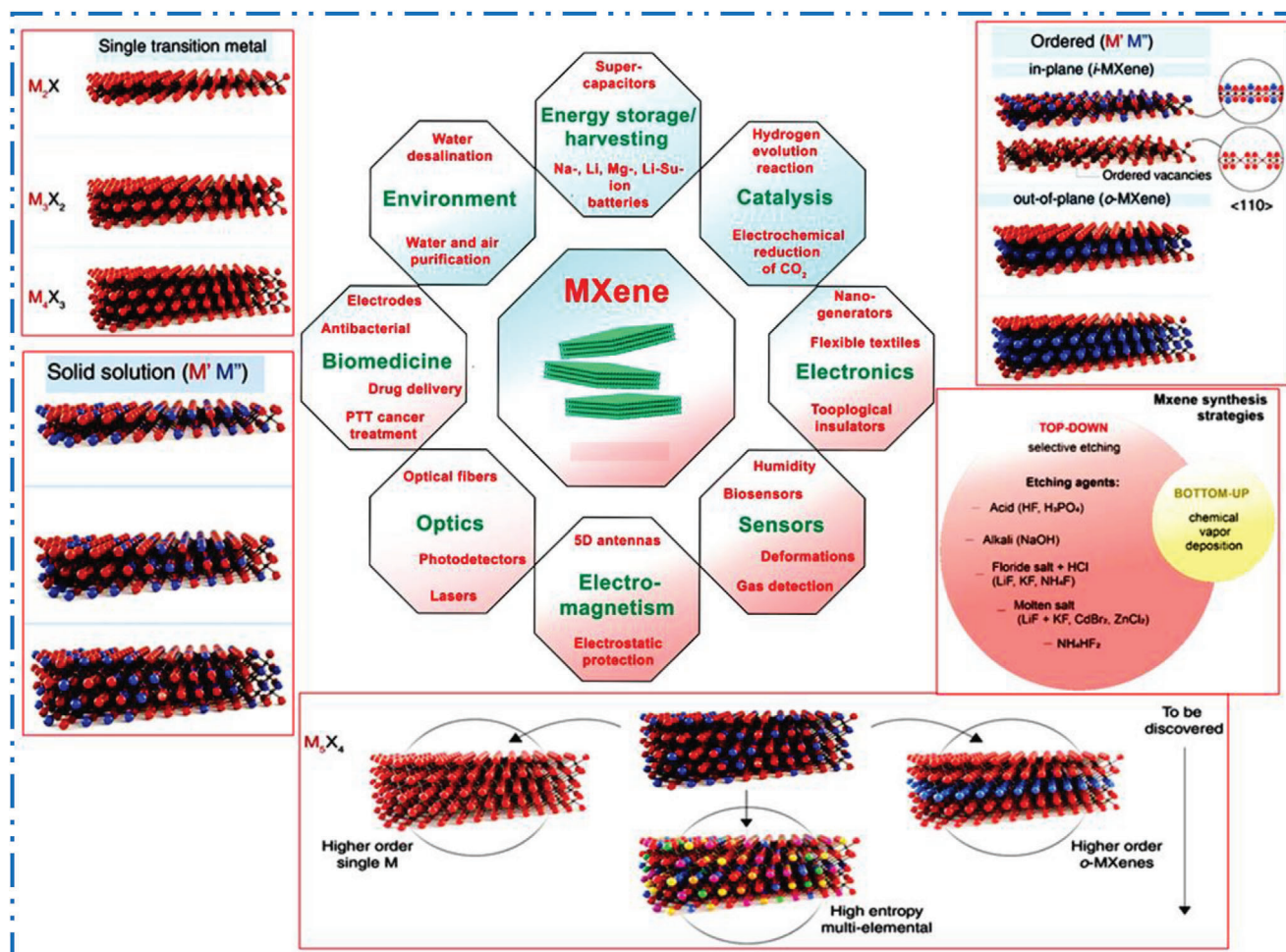


**Figure 1.** Scheme shows MXenes structures, synthesis methods, and applications. Reproduced with permission.<sup>[34]</sup> Copyright 2021, American Association for the Advancement of Science (AAAS).

interference shielding and communication. The redox activity of TMs atoms on MXene NMs surface allows electrocatalysis; rechargeable batteries as well as supercapacitors (SCs).

The 2D NSs are regulated spaced apart to conduct dialysis, gas separation, and water purification. MXenes' high surface charges enable liquid crystal growth and aqueous molecule hanging out with no requirement of surfactants or binders. For the purpose of synthesizing multilayer (ML) structures and modifying property, 2D MXene NMs' layer can intercalate organic molecules, polymers, and ions. As the 2D MXene NMs have revealed various chemical, optical, electrical, and mechanical capacities so, the proposal of MXetronics (all-MXene optoelectronics) was suggested. The 2D Ti-based MXene NMs, their hybrids and composites with polymers, ceramics, and metals are mostly drawing attentions and since they are readily accessible materials, which are nontoxic and environmental friendly. On the other hand, in this article we will spotlight on current discoveries of non-Ti based MXene NMs, which use various possible metal atoms in substitution of Ti. The  $\approx 70\%$  above studied MXene NMs are Ti-based MXenes while the other part is subdivided to other less studied early TM-based M-MXenes-based NM (Figure 2e). On the other hand, there are a small number of articles related to the 2D non-

Ti MXene NMs generally because of their difficult production process based on conventional synthesis techniques. Regardless of their complexity of synthesis, each metal has potential intrinsic properties, with abundance at market price, and once integrated in the M-based 2D MXene NMs, have extremely fascinating devices uses and even provide amazing properties than the usual Ti-based MXenes.<sup>[43]</sup> A summary representation in Figure 2f shows the regions covered in this article. The enormous attractiveness of the 2D MXene NMs over past 11 years was outcome in important number of research articles; especially review articles that include their synthesis mechanisms, properties, intercalations, and novel devices applications.<sup>[5,13,24,44]</sup> Yet the majority of these articles are relied in the region of Ti-based MXene NMs classification that was intensely examined in broad applications, for example, optoelectronics, UV-type photodetector, biosensor, batteries, electro(photo)catalysts, membranes, and so on.<sup>[5,13,24,44]</sup> At this time, in this article we will give a distinctive evaluation on the challenges related to synthesis, their novel properties and uses of 2D non-Ti MXene NMs. In other words, we will explain their definite atomic configurations, various properties that occur, and possible uses that these properties allow. Particularly, an evaluation of advantage and disadvantage relative to the 2D non-Ti



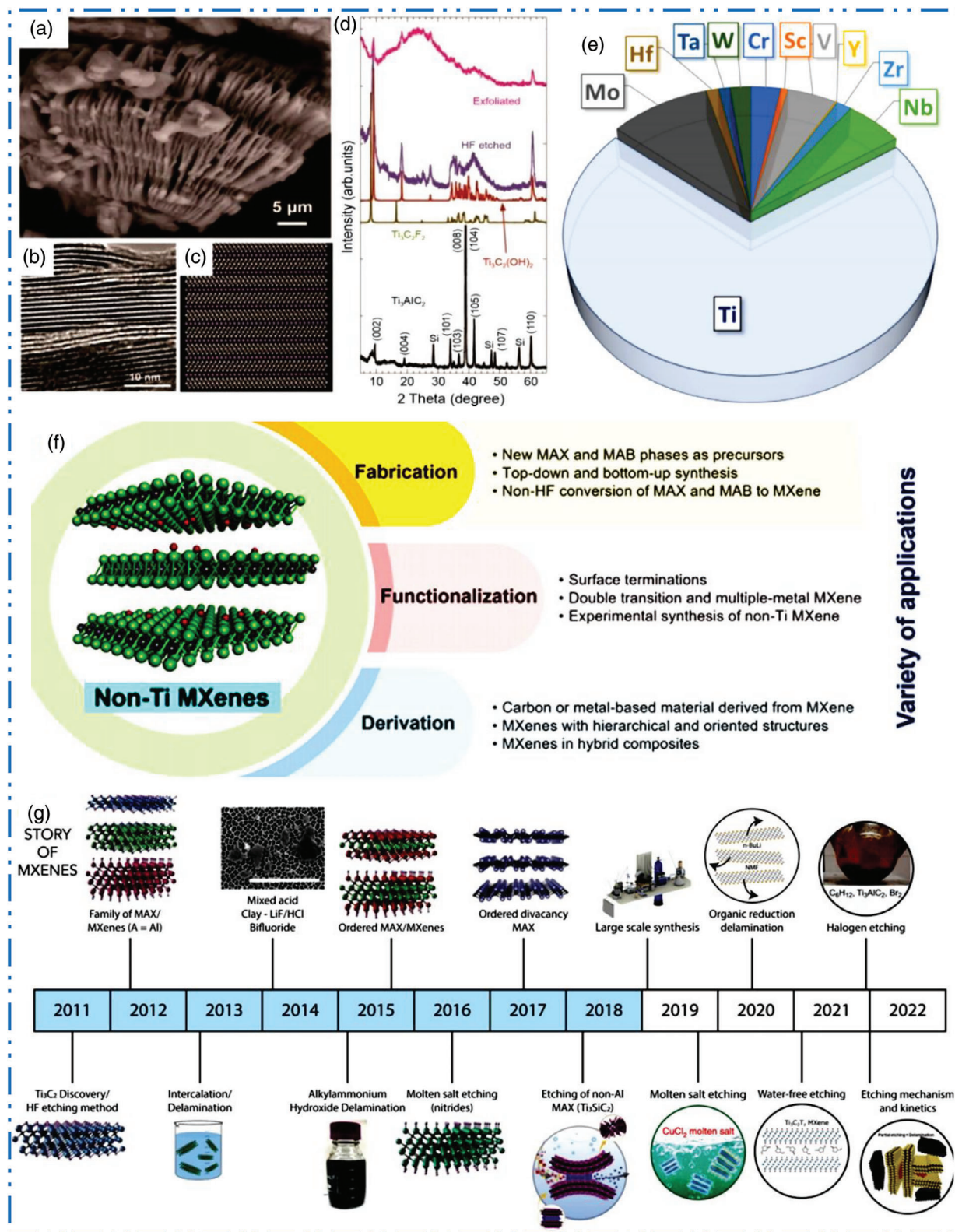


**Figure 2.** a,b) SEM, along with TEM of ML  $\text{Ti}_3\text{C}_2\text{T}_x$  etched by using HF, c) atomic model of  $\text{Ti}_3\text{C}_2\text{T}_x$  after Li insertion ( $\text{Ti}_3\text{C}_2\text{Li}_2$ ), d) XRD of  $\text{Ti}_3\text{AlC}_2$ , computational-XRD of  $\text{Ti}_3\text{C}_2\text{F}_2$  as well as  $\text{Ti}_3\text{C}_2(\text{OH})_2$ , and  $\text{Ti}_3\text{C}_2\text{T}_x$  gained by etching/exfoliation. Reproduced with permission.<sup>[42]</sup> Copyright 2022, Wiley. e) Chart shows the comparison of Ti-based and non-Ti MXene. Reproduced with permission.<sup>[37]</sup> Copyright 2023, Elsevier. f) Summary of article focuses areas and future directions of non-Ti MXene NMs. g) Story of MXenes family production. Reproduced with permission.<sup>[34]</sup> Copyright 2021, American Association for the Advancement of Science (AAAS).



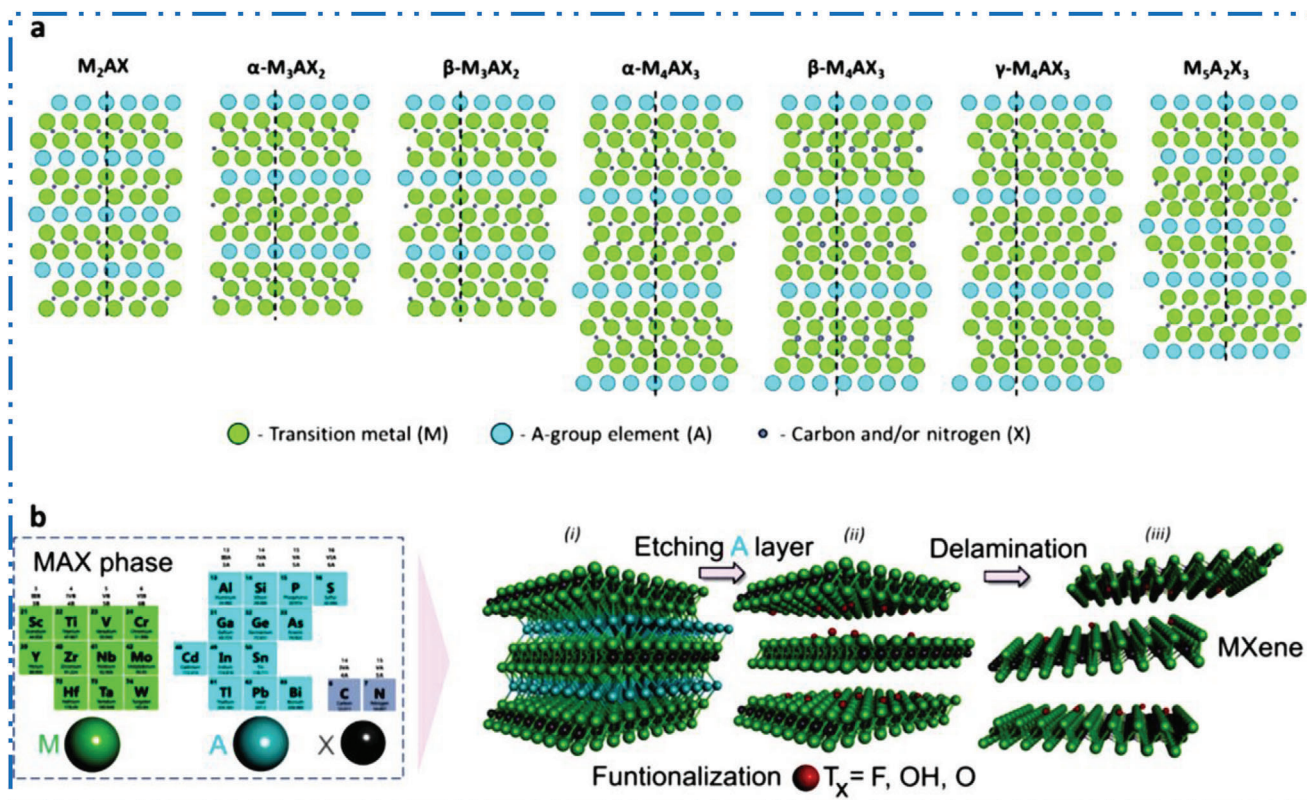


**Figure 3.** a) Various MAX crystal structures, schematics of the (1120) planes in various MAX phases. Reproduced with permission.<sup>[45,50]</sup> Copyright 2013, John Wiley & Sons. b) schematic illustration of MAX to MXene transformation. Reproduced with permission.<sup>[37]</sup> Copyright 2023, Elsevier.

MXene NMs family is obtainable to demonstrate their possible impact for increasing this novel materials research field of NMs. At the end we will explain in detail about the future views as well as suggestions to the direction of non-Ti MXene NMs growth, properties, and novel applications.

## 2. Important Factor to Know before MXenes Synthesis

### 2.1. Why Non-Ti MXenes Are Important to Study

Here are a few reasons why 2D non-Ti MXene NMs based research should be taken seriously.

- 1) Unique properties: Non-Ti MXenes exhibit unique properties, such as high electrical conductivity, mechanical strength, thermal stability, and good electrochemical and thermal properties, which make them attractive for a variety of applications. Exploring the potential of these materials could lead to the discovery of new materials with novel properties and applications.
- 2) Broad range of applications: Non-Ti MXenes have been shown to have potential applications in areas such as energy storage, catalysis, sensors, electromagnetic interference (EMI) shielding, structural materials, coatings, and more. As such, exploring non-Ti MXenes could lead to the development of new technologies and materials that could have a significant impact on various industries.

- 3) Sustainability: As previously mentioned, non-Ti MXenes may be synthesized from more abundant and environmentally friendly sources, making them a more sustainable alternative to Ti-based MXenes. With growing concerns about sustainability and environmental impact, the development of sustainable materials is becoming increasingly important.
- 4) Potential economic benefits: The development of new materials and technologies based on non-Ti MXenes could lead to economic benefits for countries and companies investing in research and development. For example, the development of new energy storage materials could have significant economic benefits in the renewable energy industry.

In summary, non-Ti MXenes research should be taken seriously due to their unique properties, broad range of potential applications, potential sustainability benefits, and potential economic benefits. Now we will explain various factors those strongly affect on the properties as well as applications of non-Ti MXene NMs.

### 2.2. Chemistry of MXene Precursors

The beginning of an accomplishment and future of the 2D MXene NMs as NMs was made possible by MAX predecessors. Using the general formula  $M_{n+1}AX_n$ , Barsoum<sup>[45]</sup> studied a new group of solids, where M is early TMs, A is an element from group-(12–16), and X is carbon or nitrogen (Figure 3a). Value of  $n$  signifies the configuration of  $M_{n+1}AX_n$  layers as 211, 312, and

413, for  $M_2AX$ ,  $M_3AX_2$ , and  $M_4AX_3$ , respectively. The majority of MAX phases are reported having  $P63/mmc$  space group hexagonal crystal structures.<sup>[46]</sup> Layers of “A” elements positioned in center of trigonal prisms are placed between layers of edge-shared  $M_6X$ -octahedra in their crystal structure.<sup>[47]</sup> The non-MAX phases of Sc, Zr, and Hf, by contrast, are predicted to form layered compounds with alternate NaCl-type M-C and  $Al_4C_3$ -like Al(A)-C sublayers. The typical formula for the non-MAX precursors is  $(MC)_n[Al(A)]_mC_{m-1}$ , where  $n$  is 2–4,  $m$  is 3–4, and A is Si and/or Ge.<sup>[48]</sup> The formulas  $M_5A_2X_3$  and  $M_7A_2X_5$  have also been used to find hybrid MAX precursors with metastable phases (Figure 3a).<sup>[49]</sup> In Ti–Si–C arrangements of  $Ti_5Si_2C_3$  with combinations of 312 and 211 MAX precursors and  $Ti_7Si_2C_5$  with combinations of 312 and 413 MAX phases, the hybrid MAX phases were first evaluated.<sup>[49]</sup> Recent studies have shown that alloying a new novel MAX precursors can produce quaternary MAX precursors materials that exhibit out-of-plane MAX (o-MAX) or in-plane MAX (i-MAX) type arrangements,<sup>[48]</sup> which then permitted the creation of novel MXene-based NMs.<sup>[33]</sup> More than 155 MAX formulations have been tested experimentally and conceptually as of this writing.<sup>[50]</sup> As their mixed metallic-covalent character, MAX precursors feature laminated structures with comparatively strong M–X along with a weak M–A bonds (Figure 3b(i)). As a result, the solid MAX phase can be broken into MX layers with accordion type structure,<sup>[51]</sup> which is seen in Figure 3b(ii). This renders M–A bond sensitive to careful acid-based etching. Delamination processes, such as ultrasonication, are subsequently utilized to relax the accordion-like configuration in order to create a 2D few layer (FL) MXene NMs, as shown in Figure 3b(iii). Even though bottom-up techniques were employed to synthesize some MXene NMs, but majority of 2D MXene NMs are synthesized by means of top-down technique and so derives their formation and nanocomposition from their particular bulk layered MAX carbide/nitride precursor-phases.<sup>[34]</sup> Because of their stability with M as well as X vacancies or mixed occupancies, bulk TMCs and TMNs have a wide range of chemical compositions and morphologies.<sup>[52,53]</sup> First effective exfoliation of  $Ti_3AlC_2$  MAX precursor in 2D  $Ti_3C_2$  form with ML configurations was reported by Gogotsi and co-workers.<sup>[32]</sup> Since then, as a minimum 100 stoichiometric MXene based compositions were excrementally as well theoretically studied, with  $Ti_3C_2T_x$  receiving more than 70% of attention in MXene NMs novel research.<sup>[54]</sup> In addition, properly designed synthesis of the o-MAX, i-MAX, non-MAX, and hybrid MAX has raised a prospect of the emergence of additional types of MXene NMs, thereby extending the list of MXene NMs. MXene family has recently referred to this historic richness of research on bulk TMCs and TMNs to regulate a chemistry of precursors as well as produce 2D MXene NMs with adjustable and/or great properties. Thus far as MXene precursors, the compositions produced have taken advantage of the chemical variety of layered TMCs/TMNs, e.g., both MAX and non-MAX phases.<sup>[55]</sup> General chemistry of these precursors is discussed in this section, and how their configuration and stoichiometry impact the fabrication and characteristics of resultant MXenes.

### 2.3. Precursor Chemistry to Predict Exfoliation Energy

Generally, majority of experimentally produced novel 2D MXene NMs are synthesized from their bulk MAX precursors, which

are physically characterized via  $M_{n+1}X_n$  layers interleaved by single layer (SL) of group A-atoms in MAX phases (Figure 4a).<sup>[35]</sup> The  $M_{n+1}X_n$  layers are kept jointly in these precursors via strong ionic/covalent M–X bonds inside a layers and weak metallic bonds (M–A) in layers (Figure 4b). A few number of non-MAX precursors were exfoliated into 2D MXene NMs’ feature comparable to M–X and M–A bonds, for example,  $Mo_2CT_x$  from  $Mo_2Ga_2C$  (Figure 4c). As these disparities in binding strength so, exfoliation is possible by a cleave M–A bonds while retaining  $M_{n+1}X_n$  2D layers.<sup>[56]</sup> Precursors are frequently put in liquid acidic etchants<sup>[57]</sup> or molten salts<sup>[58]</sup> to exfoliate the  $M_{n+1}X_n$  layer of MXene NMs. Because early TMCs/TMNs are highly stable in such applied atmosphere.<sup>[59]</sup> The  $M_{n+1}X_n$  layers remain intact while M–A bonds are targeted by particular etchant, resulting in selective etching and loss of A layers. Relative potency of the present chemical bonds, especially a strength of M–X contrast to M–A bonds,<sup>[60]</sup> is an important element in the effective separation of 2D  $M_{n+1}X_n$  MXene NMs layers from their bulk-predecessor phases. As SL crystals of MAX as well as non-MAX precursors were segregated through shearing at M–A interfaces,<sup>[61]</sup> the influence of these differing bond strengths in MAX and non-MAX predecessor phases may be detected in the 2D MXene NMs synthesis using mechanical exfoliation. Differences in composition (M, A, and X) and bond chemistry also have an impact on the configuration, for instance, the ordering of M layers (such as o-MAX compared with i-MAX predecessor phases<sup>[62]</sup>). From a practical standpoint, additional aspects, for instance, etchant solution and synthetic techniques influence the effectiveness of the MAX to 2D MXene family members. These synthesis aspects govern a thermodynamic possibility and kinetics of etching response.

Usually, MAX and non-MAX precursors exfoliation energy to the 2D MXene NMs are determined by comparative M–X (vs M–A) bond strength, which is estimated by bond force constants (Figure 4d).<sup>[60]</sup> When both links are strong then poor exfoliation into 2D MXene NMs take place, and when both bonds are weak, MAX precursor phases dissolve at some point in etching.<sup>[63]</sup> Precursor compositions with 1) very weak M–A bonds and 2) extraordinarily strong M–X bonds, for instance, have reduced exfoliation energy and are therefore simply exfoliated to a various MXene NMs. Trend (1) in computed exfoliation energy and M–A bond force constants is shown in Figure 4e.<sup>[64]</sup>

Regardless of their bulk MAX phase precursors’ configuration ( $M_{n+1}AX_n$ ,  $n = 1–3$ ), the examined MAX predecessor phases were anticipated to have the similar growing exfoliation energy development with greater M–A force constants.<sup>[60]</sup> This finding suggests that the energy of MAX-to-MXene involved is determined less by MAX configuration ( $n$ -value) and further by surface TMs M occupied in both M–X and M–A bonding. The  $n$ -value’s significance is addressed in etching with exfoliation system part. Chemical identity of X (X = C or N)-trend (2) in Figure 4f also substantially influences M–X bonds’ strength and thus exfoliation energy.

Nitrides are projected to have greater exfoliation energy than carbides with a similar configuration and M atoms,<sup>[60]</sup> for example, using  $M_2AlX$  MAX predecessor structure (Figure 4f).<sup>[57,65]</sup> This discrepancy was ascribed to poorer M–N (vs M–C) bond strength caused by an extra valence electron in N (vs C)<sup>[66]</sup> and other electron positions other nitride (vs carbide) MAX



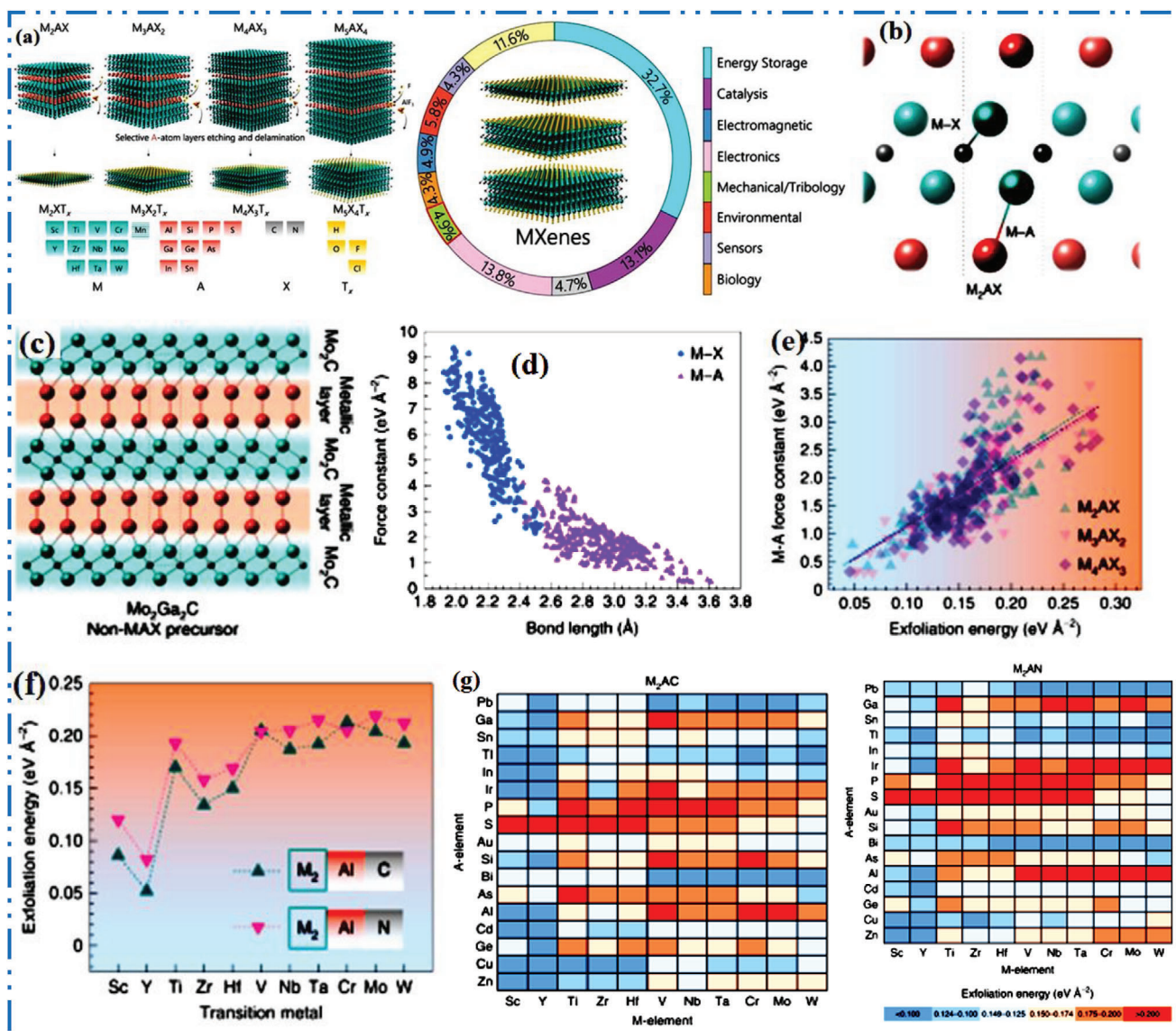


**Figure 4.** a) MAX with probable M–A–X compositions as well as capability to make various  $n$ -based configurations ( $n = 1, 2, 3, 4$ ,  $M_5AX_4$  not shown), b) scheme shows M–X besides M–A bonds in MAX precursors, d) M–A as well as M–X bond lengths, with bond force constants, e) exfoliation energy of precursor raise with higher M–A bond force constants, g) heat map of  $M_2AX$  precursor exfoliation energy with different M (horizontal), A (vertical), and X (top, bottom) compositions. Reproduced with permission.<sup>[63]</sup> Copyright 2022, Springer Nature.

candidates over stability barrier of 3.6 to 4.5 electrons per atom. Therefore, nitride MAX phases are more unstable than carbide MAX phases, which may explain why there are less nitride MXene NMs than carbide MXenes family members.<sup>[67]</sup> The M–A pairings with fewer M and/or A atoms and/or a greater number of valence electrons often make a strong M–A bonds, resulting in a slightly variation in M–X and M–A bond energies.<sup>[68]</sup> MAX exfoliation varies considerably in M–A compositions for both TMCs as well as TMNs are shown in Figure 4g. Consequence of high M-atoms, with high valency expects a lower exfoliation energy,<sup>[68]</sup> and is revealed in comparatively simple exfoliation.<sup>[69]</sup> When contrast the exfoliation energies, the outcome of high valency and small atomic radii in A elements is also obvious.<sup>[57,70]</sup> In addition to MAX precursors phase, which have proven exper-

imentally challenging to exfoliate into various 2D MXene-based NMs, compositional manipulation of chemical bonding was also used in non-MAX precursors phase. For instance, it has not been able to synthesize 2D  $Mo_2CT_x$  MXene by exfoliating a single Ga-layer from the MAX  $Mo_2GaC$  precursor phase. Instead,  $Mo_2CT_x$  was created by synthesizing the non-MAX  $Mo_2Ga_2C$  layered phase (Figure 4c), which relies by etched a weak Mo–Ga along with Ga–Ga metallic connections. This phase has two atomic layers of Ga in layers of 2D  $Mo_2C$  NM. Another illustration is a challenging production of pure  $Hf_3C_2T_x$  because  $Hf_2AlC$  is frequently found in  $Hf_3AlC_2$  MAX phases,<sup>[71]</sup> resulting in low phase purity of produced  $Hf_3AlC_2$  MAX phases.

Non-MAX  $Hf_3Al_4C_6$  precursor, which consists of covalently bound  $Al_4C_4$  layers sandwiched by  $Hf_3C_2$  layers,<sup>[55]</sup> is a novel



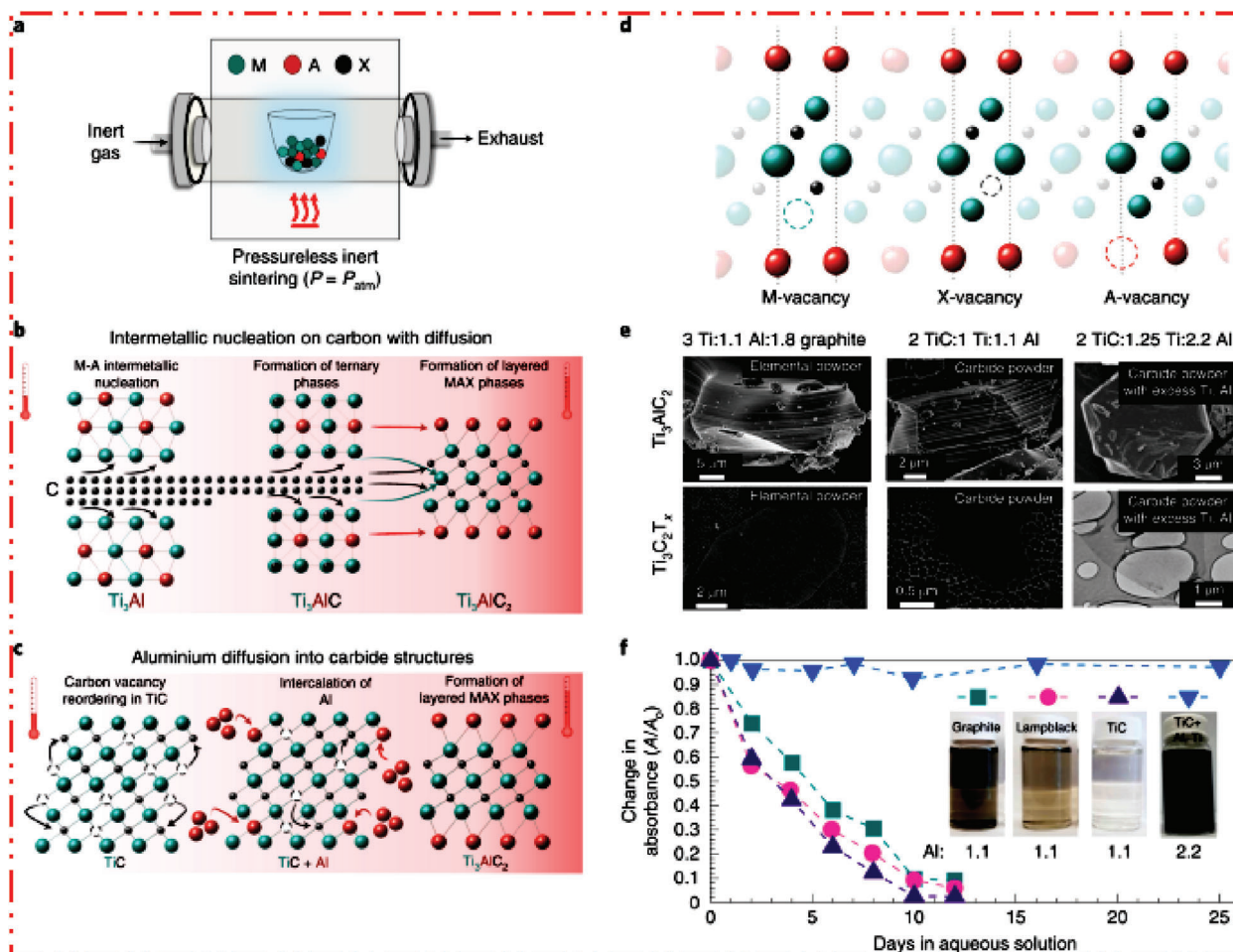


**Figure 5.** a) Production of MAX, b) employing elemental powder type precursors, production of  $Ti_3AlC_2$  precursor starts by Ti–Al intermetallic creation, afterward carbon diffusion in intermetallics to synthesize  $Ti_3AlC_2$ . c) Production of  $Ti_3AlC_2$  precursor phase via carbide powder precursors, d) production of MAX precursors forms M, A, and/or X vacancies, and e) selection of precursors have a diverse impact on MAX grain size/shape and properties of resulting MXene nanoflakes. f) Defects in MAX converted to synthesize expected MXene NMs. Reproduced with permission.<sup>[63]</sup> Copyright 2022, Springer Nature.

approach. The interfacial M–(Al, Si) bonding in the  $Al_4C_4$  layers diminishes when Si is added, resulting in a  $(Al, Si)_4C_4$  solid solution, which lowers the exfoliation energy of the layers toward 2D  $Hf_3C_2T_x$  type MXene based NMs.<sup>[55]</sup> Therefore, 2D MXene NMs that would normally be challenging to exfoliate using MAX precursor phase can be produced by intentional compositional study of non-MAX phases. In summary, both MAX and non-MAX precursors may be designed to a great extent depending on composition because of the distinction between the metallic M–A bonds and the ionic/covalent M–X interactions. Range of 2D MXene precursors and subsequently the 2D MXene NMs will increase with further experimental investigation across various M–A–X chemical compositions, directed by their chemical bonding behavior.

## 2.4. Precursor Synthesis Effect on MXene Structure

Next step is to further evaluate the research study synthesis of the MAX precursor for the 2D MXene NMs after taking into ac-

count how chemical bonding in MAX as well as non-MAX phases affects their exfoliation energy. According to a top-down strategy from precursor to 2D MXene NMs, future MXene characteristics will be significantly influenced by handling actions to synthesize MAX and non-MAX precursor phases. Here, we talk about how characteristics and purity of MAX phases are affected by elemental phase precursors (M, A, and X) and heat treatment. Precursor phases are frequently created at atmospheric pressure, direct sintering in applied inert gas based atmosphere (Figure 5a). This procedure produces porous sintered billets<sup>[72,73]</sup> and makes it easier to convert them into powders for etching. Dense MAX precursor bodies created by hot pressing and hot isostatic pressing, although they are more challenging to crush and grind into powders. A pristine elemental powder combination of M, A, and X or carbide/nitride powder mixes of MX and/or AX, with further elemental powder of M, A, and X were employed to create the majority of MAX precursors for synthesis of various members of 2D MXene NMs family.<sup>[74]</sup> Also metal hydrides are used.<sup>[75]</sup> Additionally, impetus is growing for MAX phase production in molten salts, which can be expanded to include the 2D

MXene production.<sup>[76]</sup> These powder mixture combinations lead to highly unique production routes for MAX-phase (Figure 5b,c).<sup>[72]</sup> Therefore, intermetallic M–A compounds are initially formed during the reactive heat treatment of precursor powders, and that these compounds then nucleate binary carbide layers on a carbon interface to produce nonlayered ternary M–A–X precursors.<sup>[77,78]</sup> According to other studies,  $\text{Ti}_2\text{AlC}$  is transformed into  $\text{Ti}_3\text{AlC}_2$  in the presence of  $\text{TiC}_y$ . According to this research, the formation route for the MAX phase employing powdered carbide or nitride mixes depends on the diffusion of M and/or A atoms into a configuration with assistance of carbon or nitrogen vacancies (Figure 5c). The MAX precursor's structure is significantly influenced by initial precursor powders used and various formation methods employed to synthesize MAX phases. Examples include variances in MAX grain size/shape were on micro/macroscale (Figure 5e, top row) and defects, for example, vacancies (M, A, and/or X; Figure 5d), etc. The resultant 2D MXene NMs form and behavior are directly related to these differences in MAX structure and stoichiometry.<sup>[79]</sup>

MAX-precursor phase sintering temperature has an impact on electrical conductivity. The formation of defects (vacancies) or absences of stoichiometric ratio in elements during higher temperature synthesis are the two main causes of low MXene electrical conductivity. Synthetic MXene NMs with a modest usual nanoflakes' size with noticeably increased conductivity after removal of impurity and HF/HCl etching are observed. This progress was credited to a rise in carbon substance,<sup>[74]</sup> which raises the possibility that abundance of metals may remove oxygen from heat treatment atmosphere as well as avoid carbon removal, which causes reduction in vacancies (or substitutional oxygen). Moreover, because defects in the 2D MXene NMs' structure significantly increase MXene oxidation.<sup>[79]</sup> The rate at which delaminated MXene NMs degrade in aqueous colloidal solutions might qualitatively reflect the defect focus in the bulk MAX precursors employed.<sup>[74]</sup> In conclusion, it is possible to anticipate the exfoliation energy of precursors used for 2D MXene NMs synthesis by using the chemical composition of M–A–X. Formation process, elemental precursors selection, their ratios, and applied heat treating situations all need to be taken into account while manufacturing these MAX as well as non-MAX materials since they have an impact on the characteristics of the precursor that is synthesized and, ultimately, the 2D MXene NMs. Even though these factors can significantly influence the characteristics of 2D MXene NMs, they are still under examined in larger MXene NMs literature, mainly for MXene NMs other than Ti-based carbide MXene NMs. Future research should examine the impacts of M, A, and X composition as well as the processes by which MAX as well as non-MAX precursors are formed.

## 2.5. Surface Terminations, Intercalation, and Delamination Strategies of MXenes

Surface termination of as-synthesized 2D MXene NMs is primarily dependent on the synthesis method we applied. While OH, F, and O are most often mentioned surface terminations in 2D MXene NMs, theoretical calculations that have also demonstrated the potential electrical, magnetic, chemical, as well as optical features of additional nonmetal surface  $\text{T}_x$  including S, Se, Te, and Cl.<sup>[80]</sup>

Therefore, analysis of alternative functional group  $\text{T}_x$  could offer certain surface functions that are useful in some applications. Depending on 2D MXene and etching conditions, mixed O, F, OH, and  $\text{T}_x$  are also typically seen when aqueous HF is utilized.<sup>[81]</sup> By means of liquid chloride salts, Cl-based termination prevailed<sup>[58]</sup> and when  $\text{NH}_4\text{HF}_2$  employed, then F-rich surface termination achieved.<sup>[82]</sup> Termination can also be changed by postsynthesis processes.<sup>[83]</sup> In their as-synthesized 2D MXene NMs, which were produced by etching MAX precursors in molten  $\text{CdBr}_2$  and  $\text{CdCl}_2$ . In the same way, Kamysbayev et al.<sup>[39]</sup> studied Br and Cl based termination with S, Se, Te, and NH via postsynthesis effects with Li and Na salts in molten bromides at 300 °C, afterward heat treatment and anhydrous washing. Their ability to change and modify terminations expands the already vast compositional space available to them. Through intercalation and delamination, ML MXene NMs can further be converted in an SL or FL 2D NSs. The attributes of their resultant 2D MXene nanoflakes are similar to those of accordion like MXene NMs, including rich surface chemistry, strong hydrophilicity, high conductivity, and a number of standout qualities including exceptional flexibility and wide interlayer spacing. To successfully delaminate an ML of 2D MXene NMs, it is essential to dissolve the dominant bonds between them. The use of ultrasonication allowed the delamination of 2D MXene nanoflakes that were only FLs thick. Although the yield is far from acceptable, this is because of strong contacts between 2D MXenes layers that are only sporadically broken by shearing force produced by ultrasonication. It has been demonstrated that introducing intercalators, both organic and inorganic, is a successful tactic for weakening the interlayer connections and promoting delamination (Figure 6a). Since the discovery of 2D MXene NSs, several intercalation and delamination combinations have been produced by intercalator dimethyl sulfoxide (DMSO).<sup>[84]</sup>

Other organic solvents, including as urea and *N,N*-dimethylformamide (DMF) were also utilized as intercalates for delaminating ML 2D MXene NMs in addition to DMSO. However, even with the intercalation of the DMSO and its family, the yield of delaminated NSs is insufficient. Additionally, intercalations using DMSO have failed to prevent the delamination of various other 2D MXene NMs.<sup>[35]</sup> It has been demonstrated that a group of organic alkali with comparatively great molecular configurations, for instance, *n*-butylamine and tetrabutylammonium hydroxide (TABOH), intercalate different 2D MXene NMs more effectively (Figure 6c).<sup>[85]</sup> Alkali cations would intercalate in MXene NMs layers and greatly enlarge their interlayer space following the dissociation of organic alkali in aqueous solution of ML 2D MXene NMs (Figure 6d). Therefore, hand shaking or moderate ultrasonication may cause ML MXene NMs to delaminate. Using aforementioned intercalation technique, SL  $\text{V}_2\text{CT}_x$  NSs were also produced, in addition to other MXene NMs (Figure 6e,f). In MXene NSs, employing organic alkali can lower F-group concentrations and raise  $\text{O}_2$  value, both of which are advantageous for some applications, like in energy storage devices, e.g., batteries. In addition to intercalator screening, intercalation technique optimization also merits special attention since it can result in optimal ML MXene delamination.<sup>[86]</sup> Even vigorous ultrasonication, delamination yield of MXene NSs in classical production is low.

TMAOH and ascorbic-acid (AA) used as intercalator and reductant, respectively, in a hydrothermal-assisted intercalation

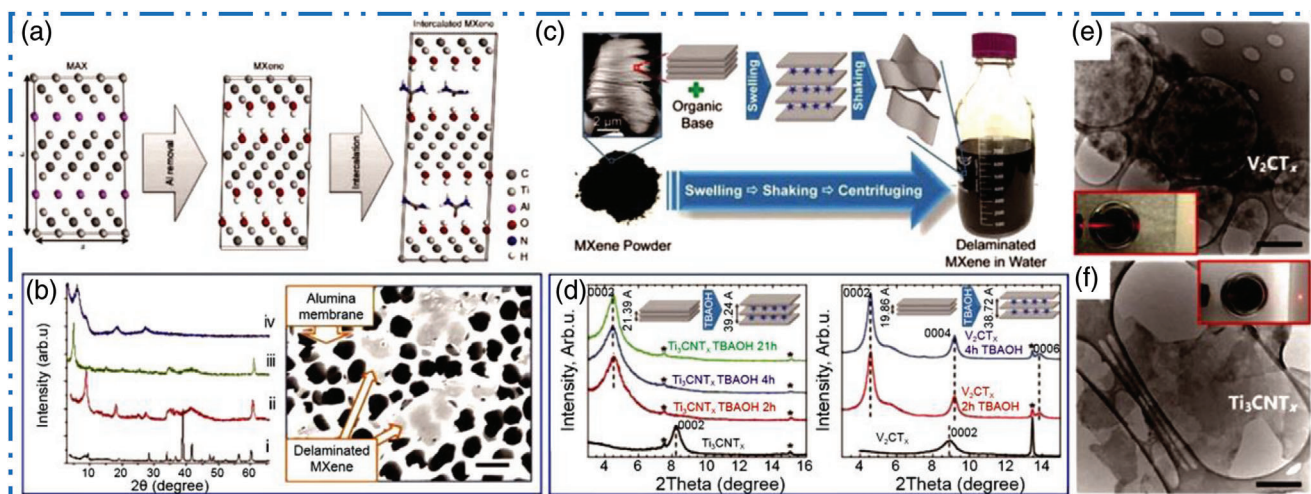


**Figure 6.** Intercalation–delamination mechanism. (a) Intercalation of  $\text{Ti}_3\text{C}_2\text{T}_x$ . (b) XRD of (i)  $\text{Ti}_3\text{AlC}_2$ , (ii) exfoliated, (iii) DMSO intercalated, and (iv) delaminated  $\text{Ti}_3\text{C}_2\text{T}_x$  (left). SEM of delaminated  $\text{Ti}_3\text{C}_2\text{T}_x$  on alumina membrane (right). (c) Scheme of MXene delamination route via organic base, (d) XRD of  $\text{Ti}_3\text{CNT}_x$  before and after mixing with TBAOH, (e) TEM of a delaminated  $\text{V}_2\text{CT}_x$  NS and (f) a delaminated  $\text{Ti}_3\text{CNT}_x$  NS. Insets show the Tyndall effect for  $\text{V}_2\text{CT}_x$  and  $\text{Ti}_3\text{CNT}_x$  aqueous solution, respectively. Reproduced with permission.<sup>[42]</sup> Copyright 2022, Wiley.

technique to enlarge intercalator diffusion.<sup>[86]</sup> Intercalation of TMAOH and subsequent delamination of ML MXene NMs were both aided by a microwave treatment, with low yield.<sup>[87]</sup> According to earlier studies, 2D MXene NMs would become unstable when oxygen and water mix, especially at high temperatures.<sup>[88]</sup> As a result, during the intercalation, MXene NSs would produce a large number of defects, which would cause them to be unstable and have a low conductivity.<sup>[89]</sup> Additionally, extended hydrothermal and ultrasonic treatments would result in a reduction in the lateral diameters of MXene NSs. Freeze-and-thaw (FAT)-assisted technique has been developed to cleave MXene from ML MXene NMs based on expansion force of water-freezing to address the aforementioned issues. The FAT development increased the yield of 2D MXene NMs with further ultrasonication, but the lateral size naturally shrank. The MXenes NSs produced by FAT approach demonstrated good conductivity and high mechanical strength as a result of the moderate circumstances of their synthesis, making them well suited for bendable renewable energy storage systems. Etching continues to pose more of a difficulty for the MXene NMs synthesis than intercalation and delamination. These adaptable and electrically conductive MXene NSs may diffuse uniformly in a range of solutions<sup>[90]</sup> and aggregate into freestanding films, flexible fibers, compressible sponges,<sup>[91]</sup> and vertical arrays, among other structures. Through creation of an excellent utilization of their surface chemistry, MXene NMs have extra functions, such as superconductivity.<sup>[92]</sup>

## 2.6. Diversity of Structures and Compositions

MXenes family benefits directly from any development for production of MAX phases with different composition and structure variety; in fact, the synthesis of 2D MXene NMs has been a major driving force behind many recent investigations on MAX phases. To illustrate this connection, we will provide a few examples of

these technological developments. Figure 1 depicts the known structures of 2D MXene NMs schematically. In 2D MXene NMs feature which have hexagonal close-packed crystal configuration with  $P6_3/mmc$  space group symmetry, similar to the basal planes in MAX precursors (where TMs in M sites are close-packed and X atoms occupy the octahedral sites in M atomic planes).<sup>[38]</sup> There have been reports of 2D MXene NMs containing Mo, Cr, Ti, Nb, V, ZrHf, Sc, W, Ta, and Y at M position. It should be noted that Cr, Sc, W, and Y were only recorded as components of o-(i)-MXene NMs, together with the other metals indicated above. At least 26 distinct o-MXene NMs were calculated in theory, including  $\text{Mo}_2\text{ScC}_2\text{T}_x$ ,  $\text{Cr}_2\text{TiC}_2\text{T}_x$ ,  $\text{Mo}_2\text{TiC}_2\text{T}_x$ , and  $\text{Mo}_2\text{Ti}_2\text{C}_3\text{T}_x$  having previously been experimentally observed.<sup>[93]</sup> Ideal o-MXene composition has an  $\text{M}'$  to  $\text{M}''$  ratio of 2:1 or 2:2, derived from an appropriate ratio of various metal lattice locations in 2D MXene configuration. By contrast, 2D i-MXene NMs are preferred only when the ratio of  $\text{M}'$  to  $\text{M}''$  is 2:1 and the size difference in  $\text{M}''$  and  $\text{M}'$  is at least 0.2.<sup>[94]</sup> In MXenes  $\text{M}'$  atoms form a honeycomb lattice and  $\text{M}''$  atom positioned on the hexagon centers and extend out from the M layers. A monoclinic ( $C_2/c$ ) or orthorhombic ( $C_2/mor Cmc$ ) configuration of i-MAX phases is inherited by 2D i-MXene NMs.<sup>[95]</sup> Up to now, 32 distinct i-MAX phases were synthesized.<sup>[96]</sup> However, most i-MAX phases have both A and  $\text{M}''$  components scratched away at the same time. Using HF, for example, Al and Sc or Y were selectively eliminated from  $(\text{W}_{2/3}\text{Sc}_{1/3})_2\text{AlC}$  and  $(\text{W}_{2/3}\text{Y}_{1/3})_2\text{AlC}$ , yielding  $\text{W}_{1.33}\text{CT}_x$  i-MXene with ordered divacancies.<sup>[97]</sup> This phenomenon results from  $\text{M}''$  elements' poorer connection to carbon sites, as shown by their outward displacement from M plane. These structural properties also enable a notion of targeted etching, in which adjusted production circumstances can assist removal of either A alone or both A and  $\text{M}''$  components from the i-MAX, as demonstrated for  $\text{Mo}_{4/3}\text{Y}_{2/3}\text{AlC}$ .<sup>[98]</sup>

For many years, solid solutions of MAX phases containing several TMs have been discovered.<sup>[99]</sup> They just lately become



aware of their 2D MXene NMs, per force; here, we provided few examples.<sup>[100]</sup> For example, double TMs based MAX phase with ordered structure  $\text{Cr}_2\text{TiAlC}_2$  was discovered in 2014. Ti-atoms dominate the core layer of M in this o-MAX ( $P63/mmc$  space group), while Cr atom nearly entirely resides in the outside layers of M (4f Wyckoff sites) in the  $\text{M}_3\text{C}_2$  blocks, while Ti-atom occupies a central layer (2a Wyckoff sites).<sup>[101]</sup> Anasori et al.<sup>[33]</sup> also studied on three novel o-MXene NMs and identified  $\text{Mo}_2\text{TiAlC}_2$  and  $\text{Mo}_2\text{Ti}_2\text{AlC}_3$  ( $\text{Mo}_2\text{TiC}_2\text{T}_x$ ,  $\text{Mo}_2\text{Ti}_2\text{C}_3\text{T}_x$ , and  $\text{Cr}_2\text{TiC}_2\text{T}_x$ ). The o- $\text{Mo}_2\text{ScAlC}_2$  and its equivalent MXene  $\text{Mo}_2\text{ScC}_2\text{T}_x$  were reported on by Meshkian et al. in 2017.<sup>[102]</sup> Tao et al. revealed the existence of a different sort of layered ordered double TMC, namely,  $(\text{Mo}_{2/3}\text{Sc}_{1/3})_2\text{AlC}$ , in which two TMs (Mo and Sc) are carbides based i-MXenes NSs. Sc-atoms are also etched in etching method. As a result,  $\text{Mo}_{4/3}\text{CT}_x$  MXene acquires ordered vacancies at the Sc atoms' original M locations.<sup>[103]</sup> New TMs for the MAX precursors, for example,  $(\text{W}_{2/3}\text{Y}_{1/3})_2$ , are present in additional in-plane ordered MAX. There have been reports of  $2\text{AlC}$  (W or Y alone does not form a MAX precursor),<sup>[104]</sup> as well as their analogous MXene NMs with ordered vacancies (e.g.,  $\text{W}_{4/3}\text{CT}_x$ ). By etching Sc and Al from  $(\text{Nb}_{2/3}\text{Sc}_{1/3})_2\text{AlC}$ , random vacancies at M sites for  $\text{Nb}_{1.33}\text{CT}_x$  were discovered.<sup>[105]</sup> According to Persson et al.,<sup>[106]</sup> etching  $(\text{Mo}_{2/3}\text{Y}_{1/3})_2\text{AlC}$ , which displayed in-plane ordering, under the right circumstances can leave behind an in-plane ordered double M compound called  $(\text{Mo}_{2/3}\text{Y}_{1/3})_2\text{CT}_x$  MXene while just removing the Al layers. Only small impurity phases of MAX precursors with  $n > 3$  have been found in bulk production or sputtered thin films.<sup>[107]</sup> By contrast, Deysher et al.<sup>[108]</sup> recently studied on the bulk powder metallurgy synthesis at 1650 °C of a  $n = 4$  phase with a composition of  $(\text{Mo}_{0.8}\text{V}_{0.2})_5\text{AlC}_4$ . The formation of  $(\text{Mo}_{0.8}\text{V}_{0.2})_5\text{C}_4\text{T}_x$  by successfully etching Al makes way for the synthesis of other MAX and MXene compounds. There are boundless possibilities for novel MXene compositions thanks to the high-entropy 2D MXene NMs with numerous M elements<sup>[109]</sup> and random binary solid solution on M sites. As this is a potent method for modifying the properties of MXene NMs, theoretically and structure space of MAX precursors and their equivalent MXene NMs will continue to grow in the upcoming years, particularly in direction of more than one M per MXene NMs (solid solution, o-MXenes, and/or i-MXenes type structures).<sup>[110]</sup>

Carbon, nitrogen, or both can occupy the X sites with exemption of  $\text{ml-Ti}_2\text{NT}_x$  and  $\text{ml-Ti}_4\text{N}_3\text{T}_x$ .<sup>[65,111,112]</sup> research on nitride 2D MXene NMs was restricted since production of nitride MXenes is somehow difficult. There are far fewer studies on nitride as well as carbonitride type MXenes than there are on C-based MXenes.<sup>[111]</sup> This is partially due to the insufficiency of MAX phases that contain nitrogen and challenges associated with synthesizing nitride MXene NMs because a nitride layers tend to dissolve in acids. It is thought that in carbonitrides MXene NMs, the carbon and nitrogen atoms reside in the octahedral positions at random, regardless of carbonitride stoichiometry.<sup>[113]</sup> On the other hand, further research is needed to have a better knowing organization of X site atoms in these MXene NMs. In bulk TMCs as well as TMNs, oxygen may substitute for both carbon and nitrogen in the lattice, generating oxycarbides or oxynitrides, correspondingly. It is essential to investigate the possibilities of such replacement in MXenes. It is still anticipated that with continued dedication, other nitride MAX precursors will eventually be created, and their etching will be exploited

to create 2D nitrides. The  $\text{Mo}_2\text{NT}_x$ ,  $\text{V}_2\text{NT}_x$ , and nitrogen-doped  $\text{Ti}_2\text{CT}_x$  have all been successfully produced using other cutting-edge methods, for example, nitriding 2D MXene NM to substitute some or all of carbon with nitrogen, which significantly improved their performance as electrocatalysts.<sup>[114]</sup> Other layered carbides, such as  $\text{Zr}_3\text{Al}_3\text{C}_5$ ,  $\text{Hf}_3(\text{AlSi})_4\text{C}_5$ ,<sup>[55]</sup> and  $\text{Mo}_2\text{Ga}_2\text{C}$ , were effectively employed to manufacture  $\text{Zr}_3\text{C}_2\text{T}_x$ ,  $\text{Hf}_3\text{C}_2\text{T}_x$ , and  $\text{Mo}_2\text{CT}_x$ , respectively. This proves that production of MXene NMs by selective etching is not confined to MAX precursor materials. Other bottom-up methods, for instance, CVD technique, were employed to produce large-area ultrathin- $\text{Mo}_2\text{C}$ , WC, and TaC films additionally to selective etching and top-down synthesis. By reducing hexagonal oxides in ammonia, Xiao et al.<sup>[115]</sup> studied on salt-templated formation of 2D MoN,  $\text{V}_2\text{N}$ , as well as  $\text{W}_2\text{N}$ .

Reliant on production technique and 2D MXene composition, MXene NMs surface has single or mixed  $\text{T}_x$  ( $\text{T}_x = \text{NH}$ , OH, Br, S, Se, O, F, Te, Cl, etc.). Postprocessing can change or delete these terminations altogether,<sup>[39,116]</sup> which has a significant impact on materials characteristics. MXenes with mixed terminations are produced via synthesis in F and Cl containing acidic solutions, with a composition of  $\text{T}_x$  (surface groups) in 2D MXene NMs' formula being  $(\text{OH})_m\text{O}_x\text{F}_y\text{Cl}_z$ .<sup>[117]</sup> Depending on the synthesis technique, density functional theory (DFT) predictions, and the use of NMR, elastic neutron scattering, XPS, and STEM techniques have recommended a random allocation for OH, O, in addition to F with a changeable ratio. Typically F and O  $\text{T}_x$  predominate over OH groups in the dry state.<sup>[118,119]</sup> In relation to M and X atoms,  $\text{T}_x$  atoms can be located at the surface in a variety of locations. The face-centered cubic (FCC) site, which is centered over TM atoms of atomic plane under an external layer, is the most actively advantageous and thermodynamically stable location for these moieties on a surface of  $\text{M}_n\text{C}$  ( $n = 2, 3, 4$ ) layers.<sup>[120]</sup> Functional groups may also organize themselves on a surface, so that they are positioned above the X atoms (hcp sites). The STEM investigations have demonstrated that F atoms only inhabit FCC sites, although O atoms can dwell at both sites, despite competition at ambient temperature in various groups to exist in favored thermodynamically stable locations. Thermal processing and vacuum annealing allow for the modification of the composition and coordination of MXene NMs'  $\text{T}_x$ .<sup>[121,122]</sup> There are two forms of intercalated (structural) water found in the configuration of MXene NMs made via aqueous etchants: physisorbed and chemisorbed. The SL of chemisorbed water with  $\text{H}_2$  bonding to a surface may still intercalated in the 2D MXene NMs, necessitating vacuum heat treatment at above 500 °C for taking away. Physisorbed  $\text{H}_2\text{O}$  may be detached at lower 200 °C heat treatment.<sup>[123]</sup> The  $\text{CuCl}_2$  or  $\text{CdCl}_2$  salt melts can be generated by etching in Lewis acids to yield Cl-terminated ML MXene NMs ( $\text{M}_{n+1}\text{X}_n\text{Cl}_2$ ).<sup>[58]</sup> To create Br terminations, bromides such as  $\text{CdBr}_2$  can be employed instead of  $\text{CdCl}_2$ .<sup>[39]</sup> In order to create a collapsed 3D structure with significant interlayer contact between the 2D MXene NSs, these homogeneous halogens based terminations (particularly Br) at the surface of MXenes must be deleted. This structure is comparable to electrides.<sup>[124]</sup> Through subsequent surface reactions, these terminations can also be altered for different functional groups, extending a variety of 2D MXene NMs' compositions. The production of MXene NMs with Te, Se, NH, O, and S based  $\text{T}_x$  is comparable. According to assessments using Rietveld analysis with EXAFS, and pair distribution function, the type of uniform

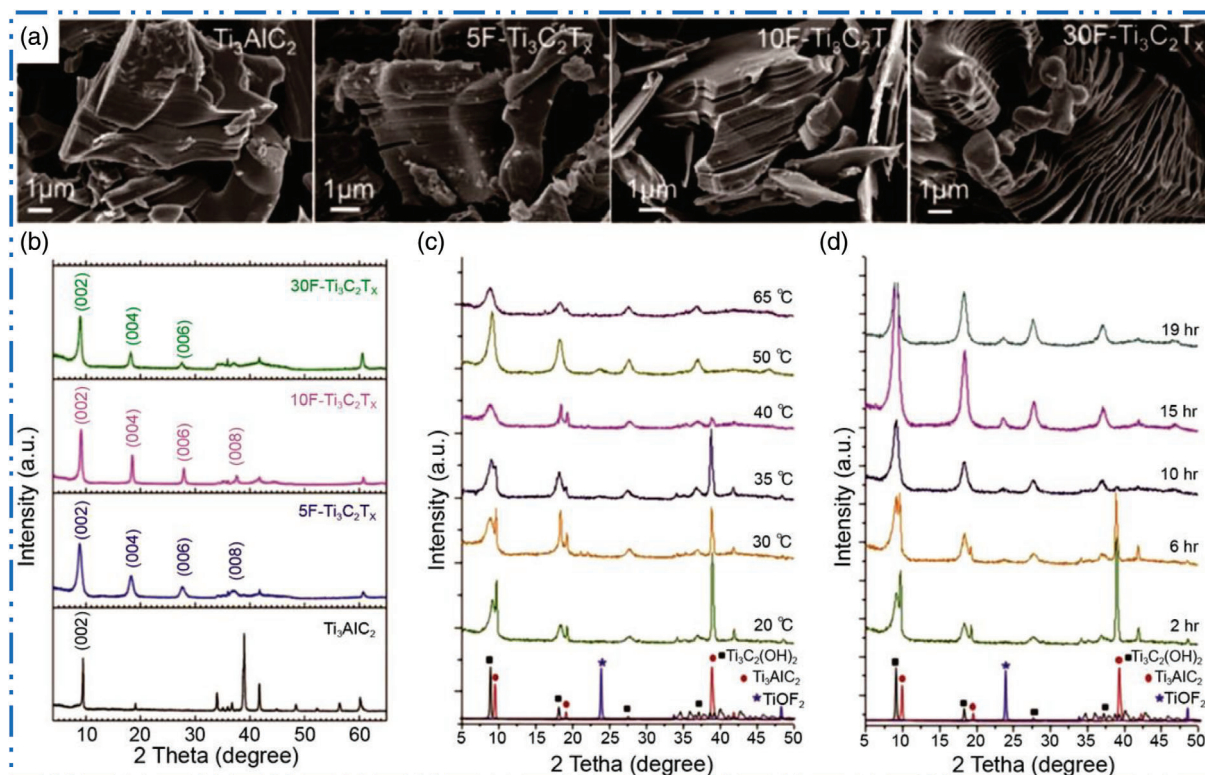


**Figure 7.** a) SEM of  $\text{Ti}_3\text{AlC}_2$  after etching with 5, 10, and 30 wt% HF. b–d) XRD of MXenes and MAX phases. Reproduced with permission.<sup>[42]</sup> Copyright 2022, Wiley.

$\text{T}_x$  that causes in-plane compressive or tensile strain causes a minor alteration in the structure of MXene NMs.<sup>[39]</sup>

### 3. General Synthesis Methods and Processing of Non-Ti MXenes

Due to clumsy size, the ML 2D MXene applications in several fields, including as nanoelectronics and medical, may be severely constrained.<sup>[125]</sup> MAX (and non-MAX) phases are designed as well as synthesized by etched, and exfoliation method to get MXene NMs. Since innovative of first MXenes, then, several other methods have been introduced, ranging from electrochemical, alkaline, molten salt, and halogen etching<sup>[35,126]</sup> to direct and indirect HF-based synthesis. It is possible to further delaminate weakly bound ML 2D MXenes into few layers (FLs) to SL-type NSs. The initial steps toward understanding why particular processes simply construct definite MXene NMs and how the characteristics and surface chemistry of 2D MXenes may be regulated through production come from atomicity knowledge of MXene etching and delamination. This section examines the selectivity of various procedures toward various 2D MXenes, highlighting trends and contrasts between the intercalation–delamination and etching–exfoliation techniques currently in use. Therefore To produce SL or FLs 2D NSs, intercalation and subsequent delamination are required. However, the yield of MXene NSs might occasionally be poor because of the robust contact between MXene layers. As a result, several improved techniques developed to produce MXene NSs with a high yield, which might even enable large-scale manufacturing.<sup>[127]</sup> By splitting the production

and processing of MXene NMs into two sections—etching tactics and intercalation and delamination strategies—this subsection reviews the production and characterization of non-Ti MXene NMs.

a) Etching strategies of MXenes: As the large quantity or bulk of MXenes NM synthesis heavily relied on MAX precursor phase so, MXenes bulk quantity can be synthesized from solid state reaction, whereas large size MXenes from magnetron sputtering (MS), epitaxial production, and CVD technique. High-quality 2D MXene NMs which are carefully regulated or with no functional groups were given by bottom-up strategies novel technique therefore; future analysis of different bottom-up strategies should be looked into using 2D MXene. After using HF MXenes etched at room temperature and variety of MXene NMs was synthesized with various HF concentrations, with different etching durations, at different temperature. According to certain experimental findings, greater HF concentrations might reduce etching time in addition to increase etching effectiveness (Figure 7a,b).<sup>[57]</sup> Figure 7c,d demonstrates that etching temperature and duration may be critical for producing ML 2D MXene NMs.<sup>[128]</sup> As HF is extremely corrosive so, rising etchant concentration, applied etching heat treatment, and time blindly will cause defects to appear quickly and dramatically lower lateral diameters of the 2D MXene NMs.<sup>[129]</sup> Therefore, MXene etching settings should be modified based on the materials' intended characteristics and uses. It is an ideal to introduce a synthesis method by which we can synthesize MXene with large lateral diameters and small defects. This will help out to use MXenes as an electrocatalysts in numerous applications like in fuel cell,

batteries, sensors, etc., because these characteristics provide excellent conductivity with strong structural stability that heavily influences rate capability as well as cyclability.<sup>[130]</sup> For that reason, moderate conditions of HF etching procedure, for instance, low HF concentrations, short etching times, and low etching applied heat treatment value, should be adapted to synthesize 2D MXene NMs in order to build high performance devices. Instead of alterations in XRD pattern, the emergence of accordion-like morphology is sometimes misinterpreted as an indication of effective etching of 2D MXene NMs. In reality, this accordion-like configuration is primarily due to emission of hydrogen gas in the etching method, which cannot be used to determine how thoroughly the MXene NMs were etched.<sup>[131]</sup> For the production of the 2D MXene NMs with the required characteristics for elevated devices performance, it is advantageous to make effective employing of the XRD investigation, where (002) diffraction peak would expand as well as downshift to a lower angle as a result of enhanced interlayer spacing. Conductivity is affected by the termination group(s) like F groups in HF etching, on outer surface of MXene NMs based on HF etching techniques.<sup>[132]</sup> Thus, it was crucial to introduce alternative methods to replace first introduced HF etching technique.

b) Non-HF conversion of MAX to MXene: While HF is reputed for being hazardous, making MXene frequently requires the employing such a strong acid. Another efficient etchant for some MAX phases etching to MXenes NMs is a combination of various kind acids (e.g., HCl) and fluoride salts (such as LiF).<sup>[133]</sup> Therefore, non-HF techniques for making 2D MXene have also been reviewed in this article. One of the potential ways to safely prepare 2D MXene is by the combination of LiF/HCl or FeF<sub>3</sub>/HCl, chemical etching, and other methods. Thus, it is important to carefully assess each of their purity, production yield, surface, as well as physicochemical characteristics as well. The ease of delamination is another benefit of this process over conventional HF etching, additionally to an effective etching with improved safety. After etching, Li-ions can enter and reside in the space in 2D MXene layers, increasing the interlayer gap. Therefore, MXene NSs may be produced by physical-shaking or sonication without the need for further intercalation procedures. Theoretically, employing various fluoride salts, an interlayer spacing of MXene NMs may be more restricted to suit needs of various metal-ion batteries. As LiF/HCl can etch and delaminate MAX precursors in single step, it is still the most used method among the several fluoride salt and acid combinations based techniques.<sup>[35]</sup> Additionally, there are various F-based etching techniques that can avoid using HF directly. For instance, in water or propylene carbonate, NH<sub>4</sub>HF<sub>2</sub> may etch A layers.<sup>[65,82]</sup> Currently, the common fluoride etching of MXene NMs unavoidably creates several F-groups and has a detrimental impact on efficiency of devices, for example, energy storage devices.<sup>[134]</sup> In fact, few F-free etching techniques were created recently that gave 2D MXene NMs the necessary characteristics.<sup>[131]</sup> A notable example is electrochemical etching, which is F-free electrolyte eliminates Al atomic layers from MAX precursors. Specifically, 3-electrode structure with Ag/AgCl, Pt, and HCl as electrolyte, reference, and counter electrodes, correspondingly was used to transform the working electrode of MAX into MXenes and carbide-derived carbon at 0.6 V.<sup>[135,136]</sup>

Alkali etching techniques are yet an additional category of alternatives to prevent fluorine contamination.<sup>[137]</sup> Although the

forementioned methods can get rid of F-group, but still require corrosive chemicals as necessary elements, posing the same safety issues as conventional HF etching. The majority of the currently used etching techniques are simply efficient for Al-MAX precursors, which cannot completely use MXene NMs. Therefore, developing a green etching technique for MXene production that is more safe and versatile is difficult. By means of Lewis acidic molten salt etching technique, which has good chemical protection and a broad etching spectrum, a substantial breakthrough was recently made.<sup>[58]</sup> Using ZnCl<sub>2</sub> or CuCl<sub>2</sub> as Lewis acidic molten salts at temperatures between 500 and 750 °C, distinct MXenes with A elements of Si, Zn, Ga, and Al may be etched from various MAX phases. There is still potential for improving etching techniques for MXene separation for particular devices. Now, we will explain stepwise in detail about various 2D non-Ti MXene NMs production.

### 3.1. Sc-MXene Synthesis

Scandium (Sc) has not obtained much attention in synthesis of novel 2D NMs since it is hard to extract in large amounts. The poor market availability and high price of Sc make it difficult to procure material. Applications should be supported by special characteristics or noteworthy performance advantages because comparable MXene NMs' end products will always be more expensive due to higher price of Sc precursors than Ti-based 2D MXene NMs. The intention of avoiding expense related to lost material via trial-and-error detection methodologies; it is better to identify first detail characteristics of the Sc-MXene based 2D NMs by theoretical evaluation. To get a ScAl<sub>3</sub>C<sub>3</sub>, the parent MAX may be converted into the 2D hydroxyl-terminated, carbon-deficient ScC<sub>x</sub>OH (Figure 8).<sup>[138]</sup> Initially, in situ reactive pulsed electric current synthesis technique used to produce a ScAl<sub>3</sub>C<sub>3</sub> precursor. Subsequently, distinct ScAl<sub>3</sub>C<sub>3</sub> layers were etched using tetramethylammonium hydroxide (TMAOH) like etchant. Figure 8a,c shows a scheme of ScC<sub>x</sub>OH, from ScAl<sub>3</sub>C<sub>3</sub> MAX and their XRD before/after etching in TMAOH with full analysis between 5° and 15°. Figure 8d shows layer expansion and individual grain exfoliation along basal planes, which indicate 70% transfer of the ScAl<sub>3</sub>C<sub>3</sub> to the 2D ScC<sub>x</sub> NM. Delaminated flexible 2D ScC<sub>x</sub> nanoflakes with hexagonal symmetry are clearly seen in the TEM picture and SAED pattern (Figure 8e).

Using a traditional pulsed DC magnetron sputtering technique, a Sc<sub>0.29</sub>Al<sub>0.71</sub>N MXene thin film measuring 780 nm thick was created on a Mo/SiO<sub>2</sub>/AlN/SOI substrate. ScAlN thin-film was deposited using a standard pulsed DC magnetron sputtering method. Four process chambers (AlN chamber, AlScN chamber, Mo chamber, and preclean chamber) and one transport chamber made up this PVD cluster system. A 12-in. Sc<sub>0.3</sub>-Al<sub>0.7</sub> alloy target was installed in the AlScN sputtering chamber. Without vacuum breaking, the ScAlN film was deposited on a 6-in. Mo/SiO<sub>2</sub>/AlN/SOI substrate. Using the 7500 W power, then a Mo (110) thin film was created keeping the target substrate distance 70 mm at 300 °C as a bottom electrode for electrical property measurements. The SOI wafer is cleaned progressively by argon ion soft etching in the clean chamber to assure clean surfaces film growth. The argon gas pressure during the 20 min



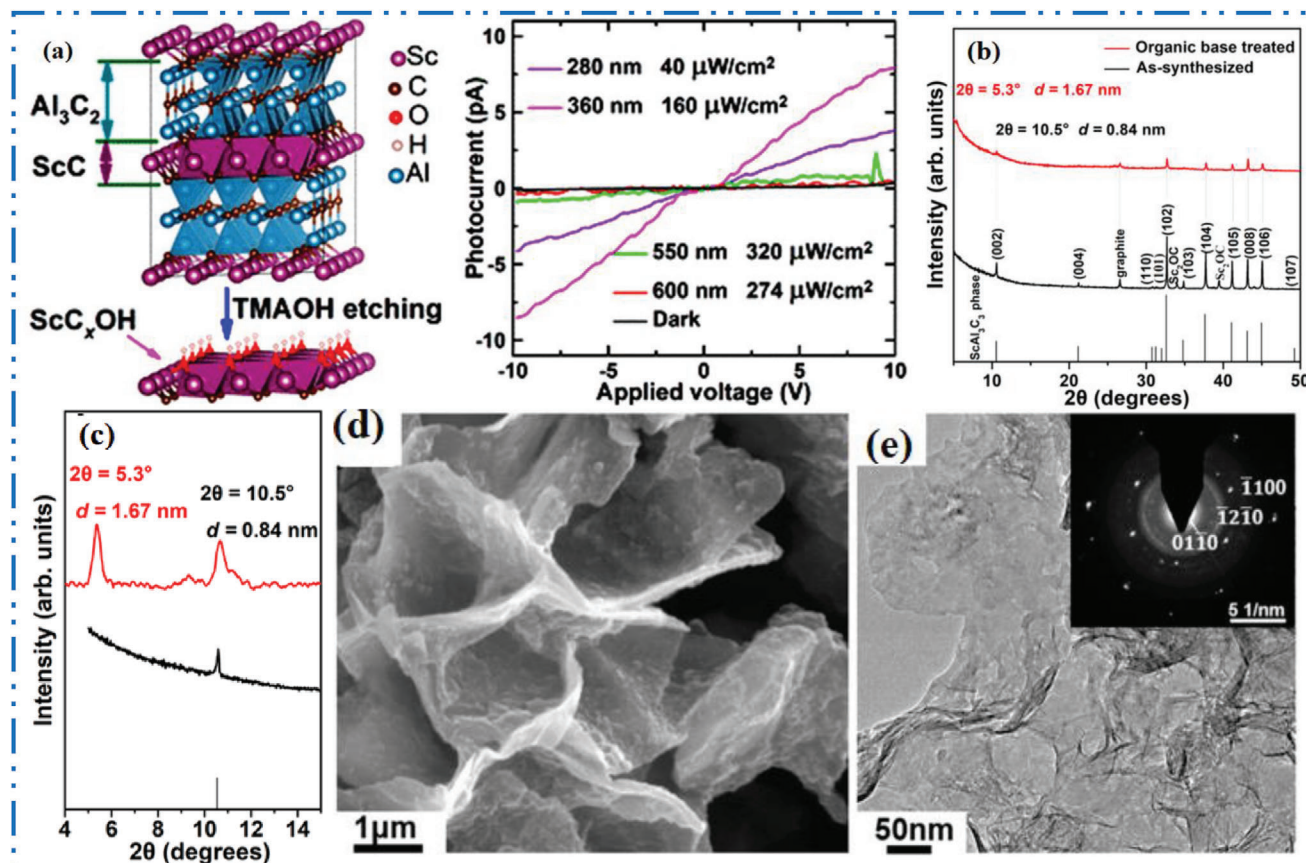


**Figure 8.** a) Scheme shows  $\text{ScC}_x\text{OH}$ , from  $\text{ScAl}_3\text{C}_3$  MAX etching, and  $I$ - $V$  curves, b) XRD of  $\text{ScAl}_3\text{C}_3$  before/after TMAOH etching, c) full analysis with  $2\theta$  ( $5^\circ$ ,  $15^\circ$ ), d) SEM after etching at  $30$ – $40^\circ\text{C}$  for  $72$  h, and e) TEM 2D nanoflakes, with SAED pattern. Reproduced with permission.<sup>[138]</sup> Copyright 2019, American Chemical Society.

sputtering period was  $2.6$  mTorr. Four  $90^\circ\text{C}$  rotations of the substrate were made during the deposition to provide uniform film thickness. It is important to note that in order to increase the quality of the  $\text{ScAlN}$  (002) with better crystal orientation employed  $\text{SiO}_2$  and  $\text{AlN}$  as a seed layer before sputtering the Mo layer. The prepared  $\text{ScAlN}$  thin film offered high-quality crystal orientation and a high effective piezoelectric coefficient  $d_{33}$  of  $12.6$  pC  $\text{N}^{-1}$ . In addition, there was no wurtzite-to-rock-salt phase transition under high pressure ( $\leq 20$  GPa), which is quite beneficial for application in strong coupling piezoelectric devices with high-pressure stability.<sup>[139]</sup>

### 3.2. V-MXene Synthesis

In comparison to Ti, vanadium (V) is one of the mainly abundant metal exist on earth, making 2D V-MXene NMs as a cost-effective one 2D NMs. In contrast to other 2D V-based MXene, non-Ti 2D MXene has demonstrated increased research for experimental investigation in various applications, including nuclear waste adsorption,<sup>[140]</sup> pseudocapacitors,<sup>[141]</sup> electrocatalysis,<sup>[142,143]</sup> theranostics,<sup>[144]</sup> etc. The V has also been successfully incorporated into double-TMs, including Ti-V, Mo-

V, and Cr-V based 2D MXene NMs,<sup>[145]</sup> according to various studies.<sup>[146]</sup> The Al atoms are typically removed by HF acid-based etching in conventional preparation of  $\text{V}_2\text{CT}_x$  MXene NMs<sup>[13]</sup> from parent  $\text{V}_2\text{AlC}$  MAX precursors phases (Figure 9a). Figure 9b shows  $\text{V}_2\text{CT}_x$  with multiple stacks of NSs that sonicated to create FL 2D NMs.<sup>[147]</sup>

Figure 9d,e shows how nitrogen physisorption and XRD may be apply to find out the transfer of MAX to 2D MXene based NM.<sup>[148]</sup> There have been information of HF free and harmless production methods employing HCl with  $\text{LiF}$ <sup>[150]</sup> or  $\text{NaF}$  that successful produce 2D vanadium carbide of high quality. Tetrabutylammonium hydroxide (TBAOH) and TMAOH are two delaminating agents that may be used to efficiently create vacancies and/or intercalation in a configuration of V-based MXene NMs. Expanding interlayer gap and creating V–O–Sn covalent bond in vanadium carbide both have been accomplished using a similar ion intercalation approach.<sup>[151]</sup> The  $2\text{D V}_2\text{CT}_x$  MXene NMs quality, durable stability, as well as optoelectronic capabilities were all enhanced because of careful control of the 2D MXene NMs' structure. The production of  $\text{V}_2\text{C}$  with a high yield of  $90\%$  and strong structural integrity has also been examined utilizing green delamination techniques employing algae extraction.<sup>[149]</sup>

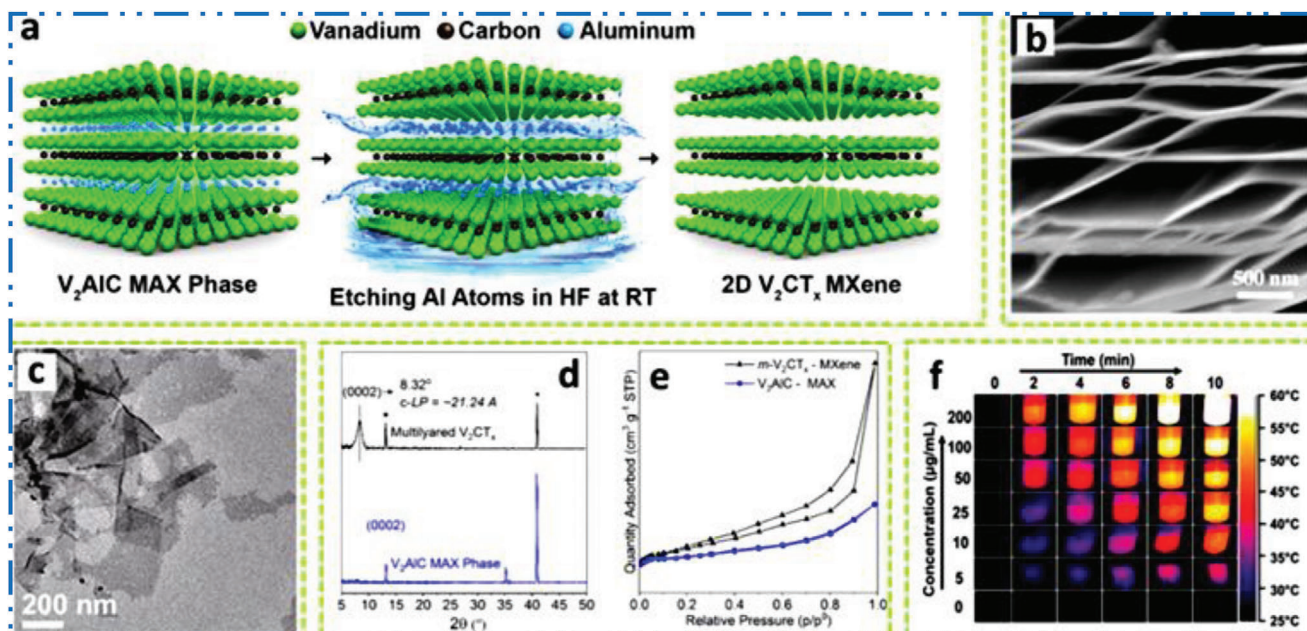


**Figure 9.** a,b) Scheme shows selective etching of  $V_2AlC$  to synthesis  $V_2CT_x$ , Reproduced with permission.<sup>[13]</sup> Copyright 2017, American Chemical Society, and its SEM, Reproduced with permission.<sup>[140]</sup> Copyright 2016, American Chemical Society. c) TEM of FL  $V_2C$  after sonication. Reproduced with permission.<sup>[147]</sup> Copyright 2021, Springer Nature. d) XRD of  $V_2AlC$  and the  $m-V_2CT_x$ , e,f) TG/DTA of  $m-V_2CT_x$  (surface area =  $10.25 \text{ m}^2 \text{ g}^{-1}$ ) as well as  $V_2AlC$  (surface area =  $1.50 \text{ m}^2 \text{ g}^{-1}$ ). Reproduced with permission.<sup>[148]</sup> Copyright 2020, American Chemical Society, and thermal photographs of  $V_2C$  NSs irradiated with 808 nm. Reproduced with permission.<sup>[149]</sup> Copyright 2020, Wiley-VCH.

### 3.3. Cr-MXene Synthesis

Intense rivalry with distinguished MXene NMs based on Nb, V, and Mo, Cr-based MXenes have received little attention. Currently the Cr motivations are receiving a great desirable consideration in the 2D MXene NMs growth due to the increased interest in its ferromagnetic performance,<sup>[152]</sup>  $H_2$  storage potential,<sup>[153]</sup> as well as electronic properties.<sup>[154]</sup> The most extensively researched MAX phase for Cr-MXene is often the MAX phase,  $Cr_2AlC$  (Figure 10a). Although it has attractive features for nanoelectronics<sup>[155]</sup> and water-splitting uses.<sup>[156]</sup> The Cr-based 2D MXene NMs are one of the hardest types of MXene NMs to manufacture experimentally.<sup>[157]</sup> Figure 10a illustrates a graphic version of exfoliation of  $Cr_2AlC$  to  $Cr_2CT_x$ .<sup>[158]</sup> Contrast between Cr (bright) and Al (less-bright) can be seen in envoy and HAADF-STEM images of  $Cr_2AlC$  MAX precursor phase (Figure 10b).<sup>[159]</sup> Ball milling,<sup>[160]</sup> the sintering technique,<sup>[161]</sup> electrochemical molten salt production,<sup>[162]</sup> with magnetron-sputtering (MS) physical vapor deposition techniques<sup>[163]</sup> are further methods that may be used to create the  $Cr_2AlC$  MAX phase. The  $Cr_2GaC$ <sup>[164]</sup> is an option to  $Cr_2AlC$  MAX precursor. There is still a difficulty in synthesizing Cr-MXene with high purity since the transition into Cr-MXenes. Although, it was failed and bulk and anisotropic Cr-carbide was preferred over Cr-based MXenes.<sup>[165]</sup> It is difficult to synthesize Cr-MXene, such as  $Cr_2C$ ,  $Cr_2N$ ,  $Cr_3C_2$ ,  $Cr_3N_2$ ,  $Cr_4C_3$ , and  $Cr_4N_3$ ,<sup>[166]</sup> which are accounted by low cohesive energy and low stability of Cr-carbide in comparison to other carbides.<sup>[45]</sup> Another factor is that other Cr-derived compounds, rather as Cr-MXene, are created during HF etching.<sup>[165]</sup> The HF acid is used to exfoliate most of the documented MAX precursors into a 2D MXene, although doing so

also dissolves metals and creates fluoride salts.<sup>[166]</sup> Combining  $FeCl_3$  with metal-complexing agent tartaric acid to create soluble, readily washable complexes of Al and Fe metal cations that employed to overcome the negative reaction of the Cr-based MAX precursor in F-based etchants.<sup>[158]</sup> Exfoliation experiments using a combination of acids (KF, HF, NaOH), and studied molten salt method were all failed till date.<sup>[166]</sup> The  $Cr_2CT_x$  was also effectively generated by electrochemically removing Al from MAX precursors using diluted HCl.<sup>[167]</sup>

Thin films of  $Cr_2GeC$  and  $Cr_{2-x}Mn_xGeC$  were deposited by utilizing the magnetron sputtering method. As long as the temperature was above  $650^\circ\text{C}$ , which allowed the reaction to take place, it was found that the deposition rates and heating regimes had no impact on phase formation. Most likely, the development of a thin film of the MAX phase was primarily influenced by the Cr:Ge:C atomic ratios. The  $Cr_2GeC$  MAX phase was more likely to develop when there was a minor surplus of carbon. Significant morphological changes brought about by increasing film thickness resulted in the formation of faceted crystallites. The AFM and XRD data further showed that manganese doping the films caused additional morphological changes and enhanced the phase composition. It was discovered that  $Cr_2GeC$  films with a thickness greater than 40 nm exhibited metallic behavior based on optical spectra, resistivity, and Hall tests. The columnar structure of crystallites may be responsible for the hopping-type conduction mechanism shown in the  $Cr_{2-x}Mn_xGeC$  film. The concentration of electrons and holes in the well-synthesized  $Cr_2GeC$  films was calculated to be  $10^{27} \text{ cm}^{-3}$  using a two-band model. The carrier mobility of the thin films was  $\approx 200 \text{ cm}^2 \text{ V}^{-1} \text{ s}^{-1}$ . This carrier mobility was one order of magnitude more than that of bulk polycrystal, demonstrating their superior crystal quality. This thorough



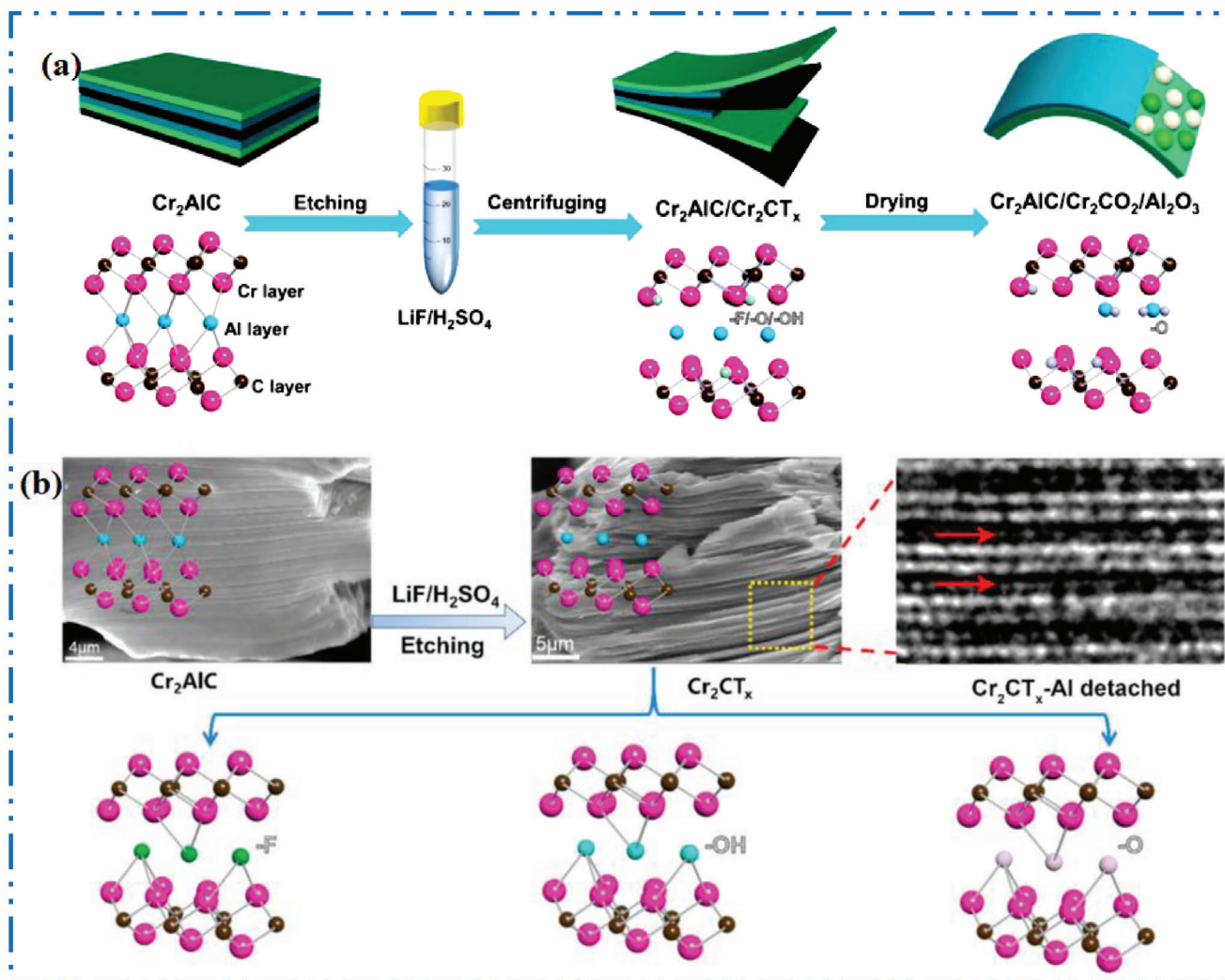


**Figure 10.** a) Scheme shows Cr<sub>2</sub>AlC crystal structure with its MXene. b) TEM image. Reproduced with permission.<sup>[158,159,168]</sup> Copyright 2020, American Chemical Society.

investigation of Cr<sub>2-x</sub>Mn<sub>x</sub>GeC thin films has improved knowledge of MAX phase formation processes and shows potential for the creation of durable conductive and protective coatings.<sup>[169]</sup>

### 3.4. Y-MXene Synthesis

The top-down method based exfoliation of MAX precursor in the 2D MXene type NM is a common production method for several MXene-based NMs synthesis. Unfortunately, very few studies have examined Y-Al-non-MAX C's systems. Crystal configuration of YAl<sub>3</sub>C<sub>3</sub> is comparable to that of layered ternary carbides, which have a common formula T<sub>m</sub>Al<sub>3</sub>C<sub>2+m</sub> (Figure 11a).<sup>[170]</sup> Crystal configuration of these layered ternary carbides may be seen in this configuration as intergrowth configurations made up of two different types of layers: i) Al<sub>3</sub>C<sub>2</sub> units arranged similarly to Al<sub>4</sub>C<sub>3</sub>, and ii) [T<sub>m</sub>C<sub>m</sub>] slabs in NaCl kind configuration. The YAl<sub>3</sub>C<sub>3</sub>, contains Y metal atoms sandwiched between Al<sub>3</sub>C<sub>3</sub>, is one arrangement that has been examined (Figure 11a). The Al-C

is bound inside the Al<sub>3</sub>C<sub>3</sub> layer with its effect on how Y atoms interface in the 2D, this configuration looks to be hard to delaminate into 2D NSs having Y atoms. The Y-atoms share C-atoms at the top as well as bottom of the crystal lattice in projected image of Figure 11a, creating a Y-C linked network in this 1D direction. When the crystal projection is turned by 60° (Figure 11a) then the Y-atoms now allocate a top and bottom C-Al atom pair. Chemical etching of Al (orange circle) is anticipated to cause the Y-C to separate into 1D linear chain before 2D MXene NSs. In an experiment, sintering stoichiometric quantities of YC<sub>2</sub> and Al<sub>4</sub>C<sub>3</sub> resulted in the formation of YAl<sub>3</sub>C<sub>3</sub> with additional Y<sub>2</sub>O<sub>3</sub>, Y<sub>4</sub>Al<sub>2</sub>O<sub>9</sub>, and amorphous carbon products. In comparison to the Zr-Al-Si-C and Zr-Al-C, the YAl<sub>3</sub>C<sub>3</sub> produced improved thermoelectric characteristics. The YH<sub>2</sub>, Al, and C powders can be in situ hot pressed at 1500 °C to create bulk YAl<sub>3</sub>C<sub>3</sub> ceramic (Figure 11b).<sup>[170]</sup> High purity YAl<sub>3</sub>C<sub>3</sub> displayed excellent elastic, mechanical, and thermal characteristics. By using high heat treatment based solid-state processes to build crystals that permitted only F to terminate the layers, bottom-up synthesis of the Y<sub>2</sub>CF<sub>2</sub> material was



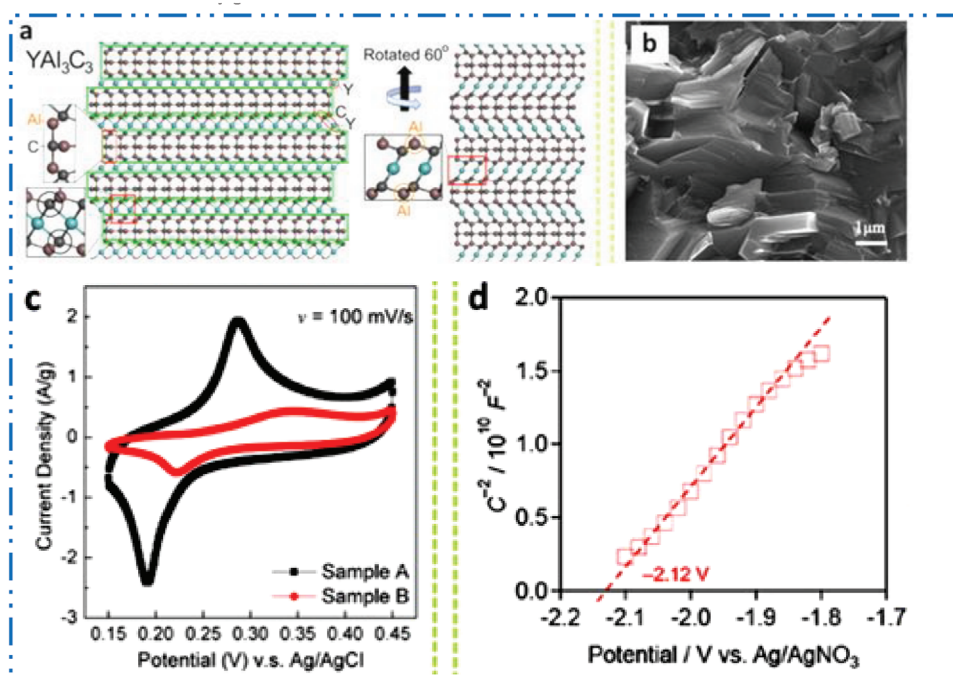


**Figure 11.** a,b) Scheme shows YAl<sub>3</sub>C<sub>3</sub> crystal structure with 60° rotation, and its SEM with its crystal structure, Reproduced with permission.<sup>[170]</sup> Copyright 2017, Elsevier. c) CVs of sample A (HF-etched and DMSO delamination), and sample B (HCl/LiF etching) electrodes in 6 M KOH at 100 mV s<sup>-1</sup>, Reproduced with permission.<sup>[172]</sup> Copyright 2020, Elsevier. d) Mott-Schottky plot of Y<sub>2</sub>CF<sub>2</sub>. Reproduced with permission.<sup>[173]</sup> Copyright 2020, American Chemical Society.

accomplished.<sup>[171]</sup> The Y<sub>2</sub>CF<sub>2</sub> is a semiconductor by nature, as determined by an investigation of its electronic structure, with a direct bandgap (B.G) of 1.9 eV, indirect B.G of 1.6 eV, and low ionization potential of 3.8 eV. Yet it was discovered that Y<sub>2</sub>CF<sub>2</sub> is delicate to water and oxygen.

### 3.5. Zr-MXene Synthesis

Layered ternary and quaternary compounds make up non-MAX phases with the typical formulas M<sub>n</sub>Al<sub>3</sub>C<sub>2</sub> and M<sub>n</sub>[−Al(Si)]<sub>4</sub>C<sub>3</sub> (T = Zr or Hf, n = 1, 2, or 3...).<sup>[174–176]</sup> The Zr–Al–C MAXs precursors are classified as layered ternary and quaternary TMCs, just like Hf–Al–C structures. Al–C units, as opposed to regular Al unit from MAX phases, are preferentially extracted for these non-MAX phases. In situ reactive pulsed electric current synthesis technique was used to create Zr<sub>3</sub>Al<sub>3</sub>C<sub>5</sub>.<sup>[177]</sup> Figure 12a–c shows that 2D Zr<sub>3</sub>C<sub>2</sub>T<sub>z</sub> MXene may be generated by selectively etching Al<sub>3</sub>C<sub>3</sub> from Zr<sub>3</sub>Al<sub>3</sub>C<sub>5</sub> using HF acid, as seen by the variations in XRD peaks and its accordion-like shape. Figure 12d,e shows a top and side view of 2D Zr<sub>3</sub>C<sub>2</sub>T<sub>2</sub> (T = F, OH, O), and electronic energy bandgaps (B.Gs) of Zr<sub>3</sub>C<sub>2</sub>F<sub>2</sub>, Zr<sub>3</sub>C<sub>2</sub>(OH)<sub>2</sub>, and Zr<sub>3</sub>C<sub>2</sub>O<sub>2</sub>, respectively.<sup>[177]</sup>

Using a ZrC sputtering target and radio frequency magnetron sputtering, the 2D MXene ZrC film created on a fused silica substrate. The face-centered cubic structure and excellent crystallinity of ZrC was confirmed by findings of the XRD examination. The ZrC films produced by magnetron sputtering deposition were exceptionally smooth and uniform, which is advanta-

geous for lowering surface flaws. The surface roughness for these samples were found 7.21 nm.<sup>[178]</sup>

### 3.6. Hf-MXene Synthesis

While M<sub>n+1</sub>AX<sub>n</sub>, an early TMC is the most often reported MAX phase, other layered ternary and quaternary TMCs, such as (MC)<sub>n</sub>Al<sub>3</sub>C<sub>2</sub> and (MC)<sub>n</sub>[Al(Si)]<sub>4</sub>C<sub>3</sub>, have M = Zr or Hf and n = 1, 2, 3, are also required after as the non-MAX precursors.<sup>[174]</sup> Predominantly single MAX precursors, based Hf and Zr, have been said to be difficult to synthesize and challenging to create.<sup>[174]</sup> Therefore, hot pressing may be used to create ternary carbides in Hf–Al–C structure, including Hf<sub>3</sub>Al<sub>3</sub>C<sub>5</sub>, Hf<sub>2</sub>Al<sub>4</sub>C<sub>5</sub>, and Hf<sub>3</sub>Al<sub>4</sub>C<sub>6</sub>.<sup>[179]</sup> The elemental distribution of Hf, Al, and C depicts the microsize configuration of Hf:Al:C.<sup>[180]</sup> Zr–Al–Si–C<sup>[181]</sup> and Hf–Al–Si–C<sup>[182]</sup> reports of quaternary carbide have therefore demonstrated success in the preparation of single-phase 2D MXene NMs precursor ceramic. Anisotropic Hf<sub>2</sub>[Al(Si)]<sub>4</sub>C<sub>5</sub> particles with a trace quantity of HfC grains are shown to have superior mechanical, thermal, and thermal conductivity characteristics than HfC.<sup>[182]</sup> Two Hf–C layers sandwiched between four Al–C layers (Al<sub>4</sub>C<sub>3</sub>) may be created by combining hot pressing and spark plasma sintering (SPS) procedures to make a Hf<sub>2</sub>Al<sub>4</sub>C<sub>5</sub> ternary carbide.<sup>[181]</sup> As interfacial connections in M–C and Al–C layers for stacked Hf–Al–C carbides are particularly strong, selectively etching and exfoliating ternary Hf–Al–C carbides must be challenging. This previously shown in Ti<sub>3</sub>(Si<sub>0.75</sub>Al<sub>0.25</sub>)C<sub>2</sub> system,<sup>[183]</sup> methods to reduce the interfacial adhesion in Hf–C and Al(Si)C sublayers by alloying Si on Al sites allow HF to

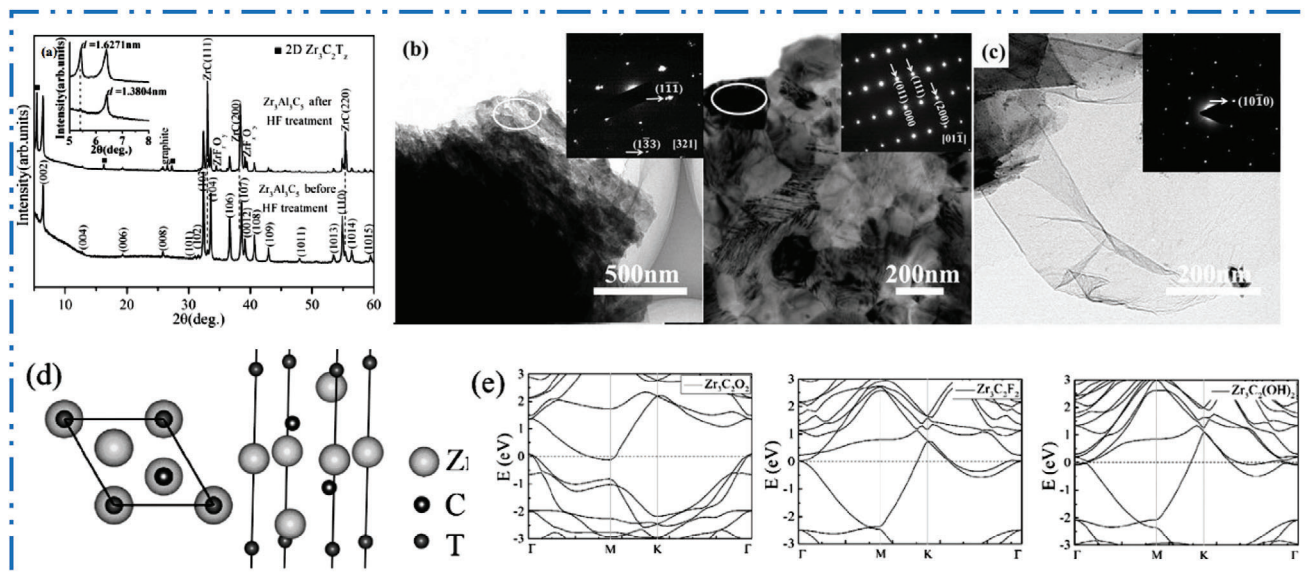


**Figure 12.** a) XRD of  $\text{Zr}_3\text{Al}_2\text{C}_5$  before/after HF dealing, b,c) TEM of vacuum heat treated  $\text{Ti}_3\text{C}_2\text{T}_x$  and  $\text{Zr}_3\text{C}_2\text{T}_x$  after ultrasonication, d) top and side view of  $\text{Zr}_3\text{C}_2\text{T}_x$ , and e) energy bands structures. Reproduced with permission.<sup>[177]</sup> Copyright 2016, Wiley-VCH.

etch the configuration of  $\text{Hf}_3[\text{Al}(\text{Si})_4]\text{C}_6$  and subsequently delaminate into ML  $\text{Hf}_3\text{C}_2\text{T}_x$ . XRD findings of  $\text{Hf}_3[\text{Al}(\text{Si})_4]\text{C}_6$  before and after being treated with concentrated HF based solution, showcasing peaks of typical MXene exfoliation from parent MAX phases. The thickness of a bilayer MXene NMs was displayed via delaminated  $\text{Hf}_3\text{C}_2\text{T}_x$  NSS, matching height profile, and B.G diagram.<sup>[118,184,186,188]</sup>

### 3.7. Nb-MXene Synthesis

The uniqueness of its metallic property, outstanding photonic and optoelectronic features, high photothermal stability, biocompatibility, great conductivity, as well as capacity for high charge-discharge rates is only a few of niobium (Nb)-based MXene NMs are characterized.<sup>[185]</sup> To date, stacked  $\text{Nb}_2\text{CT}_x$  MXene may be created using three different etching methods: HF etching, LiF + HCl etching, and hydrothermal etching. **Figure 13a,b** illustrates the typical MAX phases of  $\text{Nb}_4\text{AlC}_3$  and  $\text{Nb}_2\text{AlC}$ , respectively. Once the Al layers are successfully removed, 2D MXene is produced, giving rise to  $\text{Nb}_4\text{C}_3$  and  $\text{Nb}_2\text{C}$ . **Figure 13c** depicts the typical top-down method of Nb-based MXene NMs production,<sup>[186]</sup> with  $\text{Nb}_2\text{AlC}$  serving as the precursor MAX phases (**Figure 13d**).<sup>[187]</sup> The ML, accordion-like  $\text{Nb}_2\text{C}$  structure is then created by selectively etching of Al-layer by means of HF acid (**Figure 13e**).<sup>[188]</sup> Nevertheless, HF-based etched 2D MXene NM demonstrated a propensity to deteriorate even at room temperature.<sup>[189]</sup> Hence, the HF-free approaches that enable quick and safe production, a wide surface area, outstanding chemical stability, high porosity, high conductivity, and minimal cytotoxicity have also been very successful in producing 2D Nb-MXenes. TPAOH and TBAOH are often used as intercalants in the delamination process, which is mainly used to create FLs of MXene based NMs. Surprisingly, rising interest in employing MXene is also to create NMs that have catered to

the needs of academics. An oxidized form of  $\text{Nb}_2\text{CT}_x$  MXene has been obtained as  $\text{Nb}_2\text{O}_5$  NPs decorated on surface of carbon layers ( $\text{Nb}_2\text{O}_5/\text{C}$ ) by hydrothermal behavior (**Figure 13f**) or  $\text{CO}_2$  calcination.<sup>[190]</sup> Another distinct type of niobium carbide is seen in a 1D nanowires (**Figure 13g**).<sup>[191]</sup> ferroelectric crystals made of 2D MXene (**Figure 13h**),<sup>[192]</sup> carbon nanotubes (CNTs) and 2D  $\text{Nb}_2\text{CT}_x$  (**Figure 13i**),<sup>[193]</sup> and N-doped niobium carbide-supported niobium pentoxide (**Figure 13j**).<sup>[194]</sup>

The HF etching approach has a superior etching effect than the LiF + HCl etching method, although it was certified as an effective etchant for  $\text{Ti}_3\text{C}_2\text{T}_x$ . It may not be suited for  $\text{Nb}_2\text{CT}_x$  due to the higher bond energy to overcome (Nb–Al). Peng et al.<sup>[195]</sup> employed a hybrid solution of  $\text{NaBF}_4$  and HCl as an etchant in a hydrothermal etching process to synthesize  $\text{Nb}_2\text{CT}_x$ . With a significantly shorter etching period (20 h), a good exfoliation effect may be obtained. As a result, the hydrothermal etching approach is likely to be extended to additional 2D MXene NMs. A similar HF etching procedure may be used to generate  $\text{Nb}_4\text{C}_3\text{T}_x$ . By using the magnetron sputtering deposition process, few-layered 2D  $\text{Nb}_2\text{C}$  NSs and microfiber-based 2D  $\text{Nb}_2\text{C}$  saturable absorber were created. The substantial third-order nonlinear susceptibility and coexistence of saturable absorption and reverse saturable absorption processes are revealed by  $\text{Nb}_2\text{C}$  saturable absorber. In comparison to reverse saturable absorption processes, the effective nonlinear absorption coefficient caused by the saturable absorption effect was found to be nonlinear absorption coefficient ( $\beta_{\text{eff}}$ )  $\approx -10^5$   $\text{GW}^{-1}$ , which was two orders of magnitude greater. For the first time, the positive nonlinear refractive index  $n_2$  was calculated to be  $\approx 10^{-13}$   $\text{m}^2 \text{W}^{-1}$ . Additionally, square-wave pulse (SWP) mode-locked Yb-doped fiber laser was successfully built using a microfiber-based 2D  $\text{Nb}_2\text{C}$  saturable absorber. The single pulse energy can be increased linearly up to 0.89 nJ while the peak power remains fixed, allowing the SWP pulse width to be adjusted from 0.652 to 1.616 ns. According to our findings, 2D



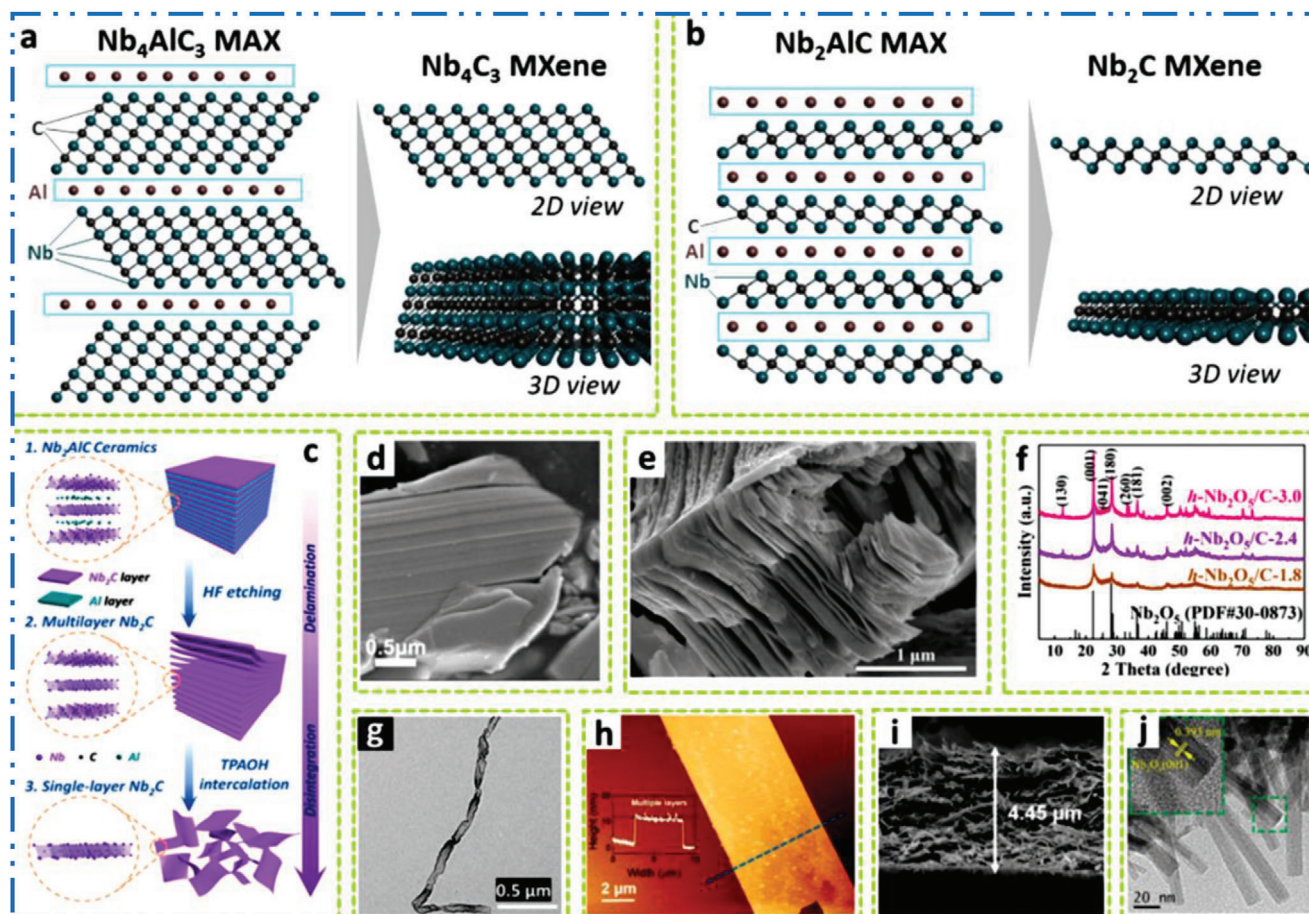


**Figure 13.** Scheme shows crystal structure of a)  $\text{Nb}_4\text{AlC}_3$  and b)  $\text{Nb}_2\text{AlC}$  and their MXene. c) Fabrication scheme diagram of  $\text{Nb}_2\text{C}$  NSs, with HF based delamination and TPAOH intercalation. Reproduced with permission.<sup>[186]</sup> Copyright 2017, American Chemical Society, d) SEM of  $\text{Nb}_2\text{AlC}$  MAX, Reproduced with permission.<sup>[187]</sup> Copyright 2020, American Chemical Society, e) SEM of HF-etched  $\text{Nb}_2\text{C}$ , Reproduced with permission.<sup>[188]</sup> Copyright 2021, American Chemical Society, f) XRD of  $\text{h-Nb}_2\text{O}_5/\text{C}$ , Reproduced with permission.<sup>[190]</sup> Copyright 2019, Elsevier, g) TEM of E-etched  $\text{Nb}_2\text{CT}_x$  nanowires, Reproduced with permission.<sup>[191]</sup> Copyright 2020, Wiley-VCH, h) AFM of  $\text{M-KNbO}_3$ , Reproduced with permission.<sup>[192]</sup> Copyright 2019, Wiley-VCH, i) SEM of  $\text{Nb}_2\text{CT}_x\text{-CNT}$ , Reproduced with permission.<sup>[193]</sup> Copyright 2016, Elsevier, j) TEM of  $\text{N-Nb}_2\text{O}_5@/\text{Nb}_2\text{C}$  composite, Reproduced with permission.<sup>[194]</sup> Copyright 2022, Elsevier.

$\text{Nb}_2\text{C}$  NSs would make a great saturable absorber for investigating saturable dynamics and ultrafast photonics dynamics in fiber lasers.<sup>[196]</sup>

### 3.8. Mo-MXene Synthesis

Effectiveness in the renewable-energy storage, electrocatalysis, and medicinal uses, molybdenum (Mo) was the next most investigated form of the 2D MXene NM despite its low crustal abundance.<sup>[197]</sup> The conventional basic materials used to produce MXenes are known as MAX phases. Nonetheless, because the thermodynamic conditions are inadequate to generate the MAX precursor of this material, the instability of  $\text{Mo}_2\text{AlC}$  and  $\text{Mo}_2\text{GaN}$  is seen. The  $\text{Mo}_2\text{GaC}$  may be effectively manufactured as layer structure bulk ceramics in its MAX precursor and can be etched to create stable  $\text{Mo}_2\text{C}$  MXene NMs (Figure 14a).<sup>[197]</sup> Little to no success, attempts to selective etching of Ga from  $\text{Mo}_2\text{GaC}$  MAX to produce  $\text{Mo}_2\text{C}$  MXene were made.<sup>[198]</sup> A large-

scale synthesis of  $\text{Mo}_2\text{CT}_x$  nanoflakes was reported by Halim et al.,<sup>[199]</sup> by selectively etching the Ga from  $\text{Mo}_2\text{Ga}_2\text{C}$  by means of a  $\text{LiF}/\text{HCl}$  solution (Figure 14b). Afterward, by hand shaking in water, delaminated 2D MXene NMs were easily produced. Unexpectedly, bulk ternary metallic boride, or MAB precursor<sup>[200]</sup> has also demonstrated promise as a basic material for 2D MBene preparation. Boron is used in place of X (C/N) in the first MAX precursor. Similar to the concept and approach used with the 2D MXene NMs, MAB precursors are etched to get 2D TM-based boride (MBene). Using a hydrothermal-assisted, HF-free etching approach, MoB MBene from MoAlB MAB phase was effectively produced (Figure 14c).<sup>[201]</sup>

$\text{MoAl}_{1-x}\text{B}$  remnants, however, show that Al was not entirely eliminated (Figure 14d). Epitaxial synthesis has been reported to produce MXene in a different non-MAX phase. For example,  $\text{MoS}_2$  crystals are chemically transformed in Figure 14e by thermal annealing in the existence of a  $\text{CH}_4$  and  $\text{H}_2$  to yield 2D  $\text{Mo}_2\text{C}$  MXene NSs. The DFT simulations showed successive hydrodesulfurization and carbide conversion processes took place on



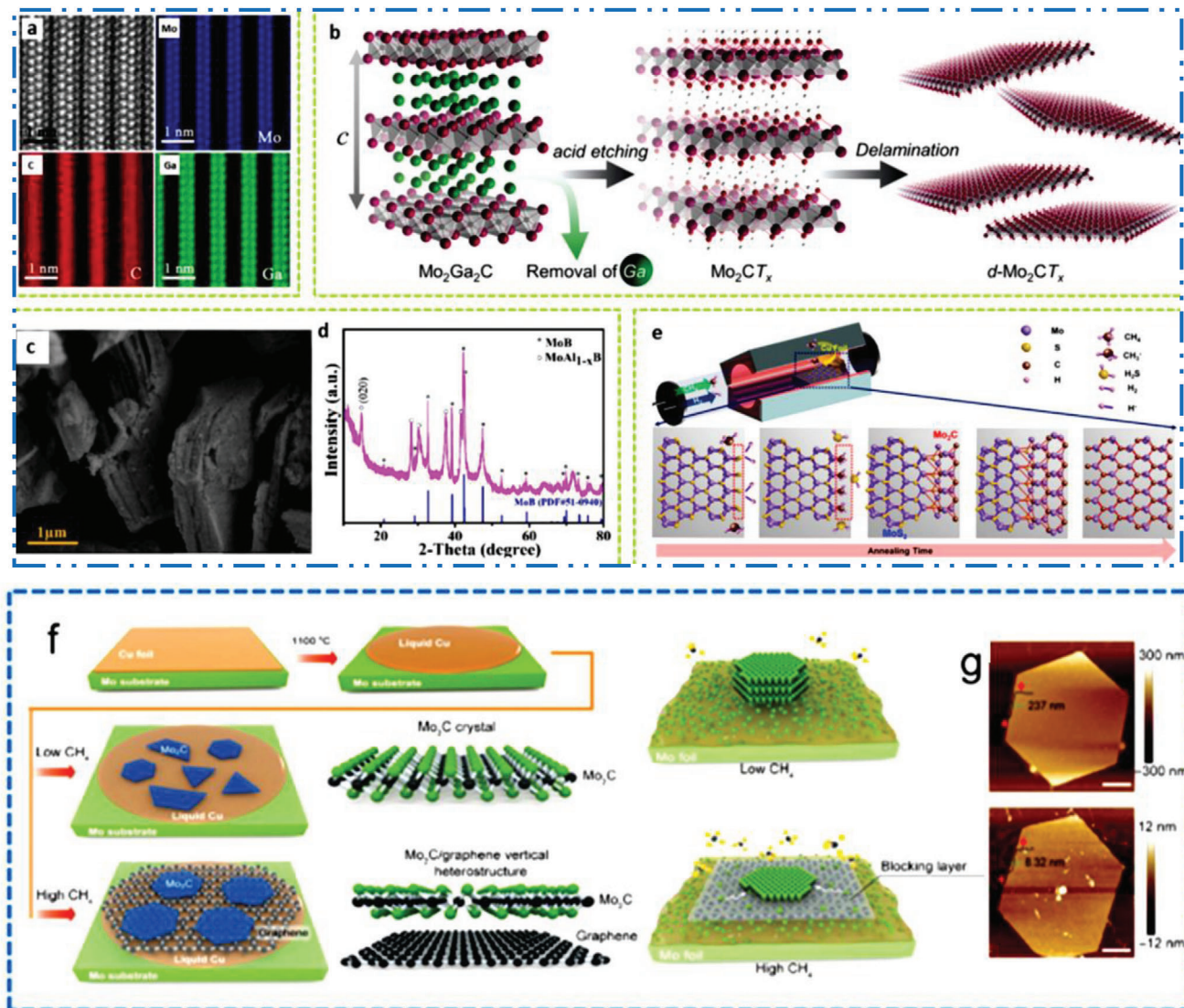


**Figure 14.** a) HRSTEM and EDX mapping of Mo<sub>2</sub>Ga<sub>2</sub>C, Reproduced with permission.<sup>[197]</sup> Copyright 2019, Wiley, b) Scheme showing synthesis as well as delamination of Mo<sub>2</sub>CT<sub>x</sub>, Reproduced with permission.<sup>[199]</sup> Copyright 2016, Wiley, c,d) SEM of MoB MBene and its XRD, Reproduced with permission.<sup>[201]</sup> Copyright 2022, Elsevier, e) Scheme shows Mo<sub>2</sub>C production using heat treatment in CH<sub>4</sub> as well as H<sub>2</sub>, Reproduced with permission.<sup>[202]</sup> Copyright 2018, American Chemical Society, f,g) scheme shows Mo<sub>2</sub>C crystals synthesis in CH<sub>4</sub> environment, and its AFM, Reproduced with permission.<sup>[203]</sup> Copyright 2020, Springer.

MoS<sub>2</sub>'s edge, where conversion method started. The Mo-MXenes may also be created by bottom-up techniques, for example, CVD and solid state reactions, which allow for fine control over the surface terminations of such MXenes. Mo<sub>2</sub>C was the first CVD-grown MXene in 2015. Geng et al.<sup>[204]</sup> established a one-step CVD approach to manufacture high-quality Mo<sub>2</sub>C crystals on in situ produced graphene using a Mo–Cu alloy as the catalyst, as illustrated in Figure 14f. Under high CH<sub>4</sub> flow rates, the quickly growing graphene film acts as a blocking layer, which is critical in controlling the thickness and homogeneity of Mo<sub>2</sub>C hexagons (Figure 14g).

The 2D MoN is the second CVD-grown MXene NM. Joshi et al.<sup>[205]</sup> devised a two-step method to produce MoN (Figure 15a).

First, resistively heated Mo filament under O<sub>2</sub> flowing was utilized to create MoO<sub>3</sub> on fluorinated tin oxide (FTO) substrate via hot-filament-CVD. Following that, the MoO<sub>3</sub> 2D NSs were annealed in an ammonia environment, resulting in the phase transition from MoO<sub>3</sub> to MoN. The 2D MoN MXene SEM shows vertically aligned stacks with the basal plane perpendicular to the FTO substrate (Figure 15b). Sun et al.<sup>[206]</sup> produced MoN from MoS<sub>2</sub> using Na<sub>2</sub>CO<sub>3</sub>-assisted nitridation (Figure 15c) in an ammonia environment at high temperatures (700–800 °C). Following the washing procedure, high purity MoN NSs may be obtained. CVD procedures, as opposed to top-down approaches, are devoid of intricate solution reactions and may produce pure 2D MXene NMs without different termination groups, such as O, F, Cl, or

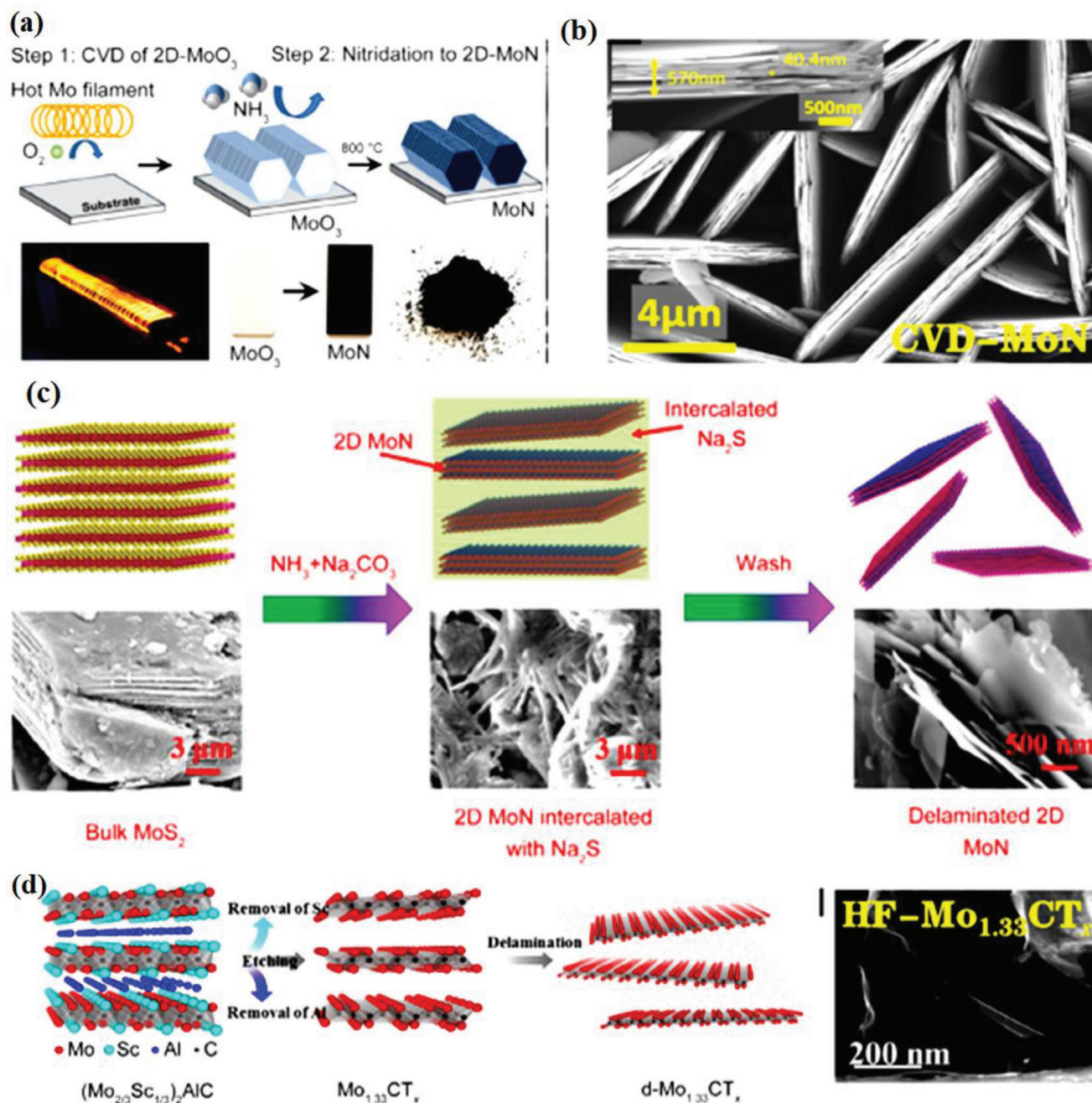


**Figure 15.** a) HRSTEM and EDX mapping of Mo<sub>2</sub>Ga<sub>2</sub>C, Reproduced with permission.<sup>[197]</sup> Copyright 2019, Wiley, b) Scheme showing synthesis as well as delamination of Mo<sub>2</sub>CT<sub>x</sub>, Reproduced with permission.<sup>[199]</sup> Copyright 2016, Wiley, c,d) SEM of MoB MBene and its XRD, Reproduced with permission.<sup>[201]</sup> Copyright 2022, Elsevier.

OH.<sup>[204]</sup> Notably, the amount of precursors (i.e., carbon or nitride resources) may be precisely regulated, allowing for the determination of the final quality of 2D MXene NMs. The effectiveness of the nitridation technique in producing 2D MoN MXene NM provides solid evidence for the synthesis of additional nitride-based MXenes. It is also worth mentioning a novel form of Mo-based MXene (i.e., Mo<sub>1.33</sub>CT<sub>x</sub>), the very defective MXene, which was discovered during the etching of (Mo<sub>2/3</sub>Sc<sub>1/3</sub>)<sub>2</sub>AlC. The etching procedure eliminates not only Al layers but also Sc, result-

ing in Mo<sub>1.33</sub>CT<sub>x</sub> MXene with ordered vacancies (Figure 15d).<sup>[95]</sup> Figure 15e depicts typical nanolaminated NSs. This faulty Mo-based MXene requires a shorter HF etching time of 24 h than Mo<sub>2</sub>CT<sub>x</sub>. Using the Mo<sub>2</sub>C sputtering target and radio frequency magnetron sputtering, a thin layer of Mo<sub>2</sub>C was created on a quartz plate substrate. A vacuum pump was used to raise the vacuum level to  $6 \times 10^{-4}$  Pa. At 600 °C, the Mo<sub>2</sub>C samples were annealed. Three distinct portions were selected for the measurements in order to gauge the thickness of Mo<sub>2</sub>C coatings.



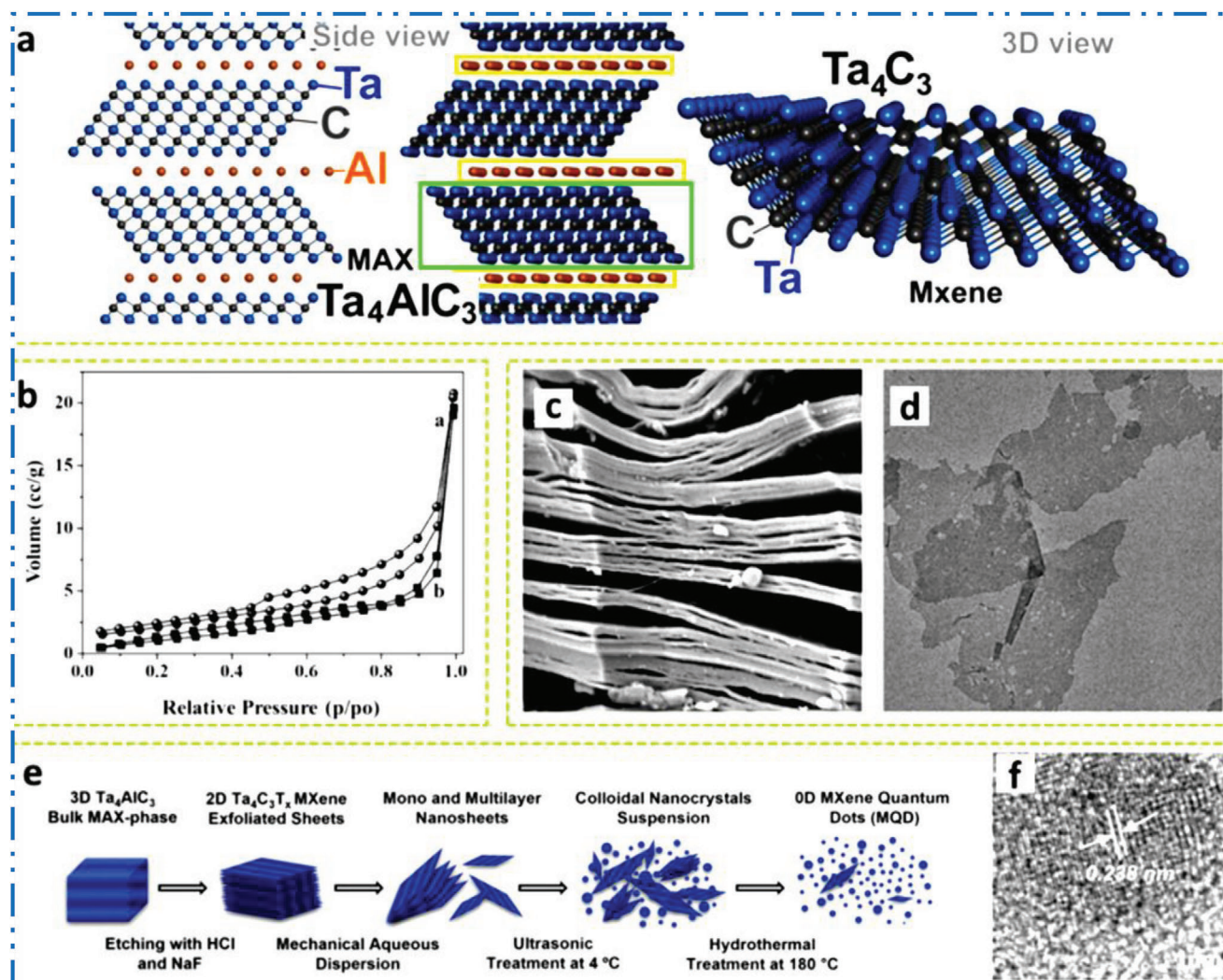


**Figure 16.** a,b) Scheme shows crystal structure of  $\text{Ta}_4\text{AlC}_3$  and  $\text{Ta}_4\text{C}_3$  and their BET, Reproduced with permission.<sup>[208]</sup> Copyright 2013, Elsevier, c) SEM of multi-layer  $\text{Ta}_4\text{C}_3$ , d) TEM of FL  $\text{Ta}_4\text{C}_3$ , Reproduced with permission.<sup>[209]</sup> Copyright 2022, Elsevier, e) scheme on exchange of bulk  $\text{Ta}_4\text{AlC}_3$  to  $\text{Ta}_4\text{C}_3\text{T}_x$  MQDs, f) HRTEM of ML  $\text{Ta}_4\text{C}_3\text{T}_x$  NSs discovered definite and exfoliated crystals with lattice d-spacing of ~0.260 nm, Reproduced with permission.<sup>[210]</sup> Copyright 2021, Wiley.

Atomic force microscopy revealed that the  $\text{Mo}_2\text{C}$  films were between 4.3 and 4.7 nm thick. The uniform surface and thickness of the thin film sample created by radio frequency sputtering are much greater, and the initial transmission is simple to manage.<sup>[207]</sup>

### 3.9. Ta-MXene Synthesis

One of the metals with the fewest unfavorable biological reactions is tantalum (Ta), with Ta-derived 2D NMs.<sup>[211]</sup> The Ta-based NMs, like 2D MXene, possess adjustable characteristics as a result, making them interesting candidates for biological applications. Typical MAX phase arrangement may be observed in the schematic illustration of  $\text{Ta}_4\text{AlC}_3$  MAX precursor's crystal configuration (Figure 16a). When Al layers are taken out from

MAX precursor, Ta-based 2D MXene NM is created, expanding similar to accordion configuration and increasing its surface area (Figure 16b).<sup>[208]</sup> Figure 16d depicts a typical multi-layered  $\text{Ta}_4\text{C}_3$  accordion-like structure with FLs (Figure 16c).<sup>[209]</sup> At a particle size of below 5 nm, finer Ta-MXene NMs were created as MXenes quantum dots (MQDs) (Figure 16e,f).<sup>[210]</sup> The synthesized  $\text{Ta}_4\text{C}_3\text{T}_x$  MQDs exhibited good biocompatibility, stable suspension, high surface area, and great thermal stability.

### 3.10. W-MXene Synthesis

MAX precursors are employed as the primary precursor material for the production of MXene NMs, and it is already stated in the earlier section of this paper. Nevertheless, it was



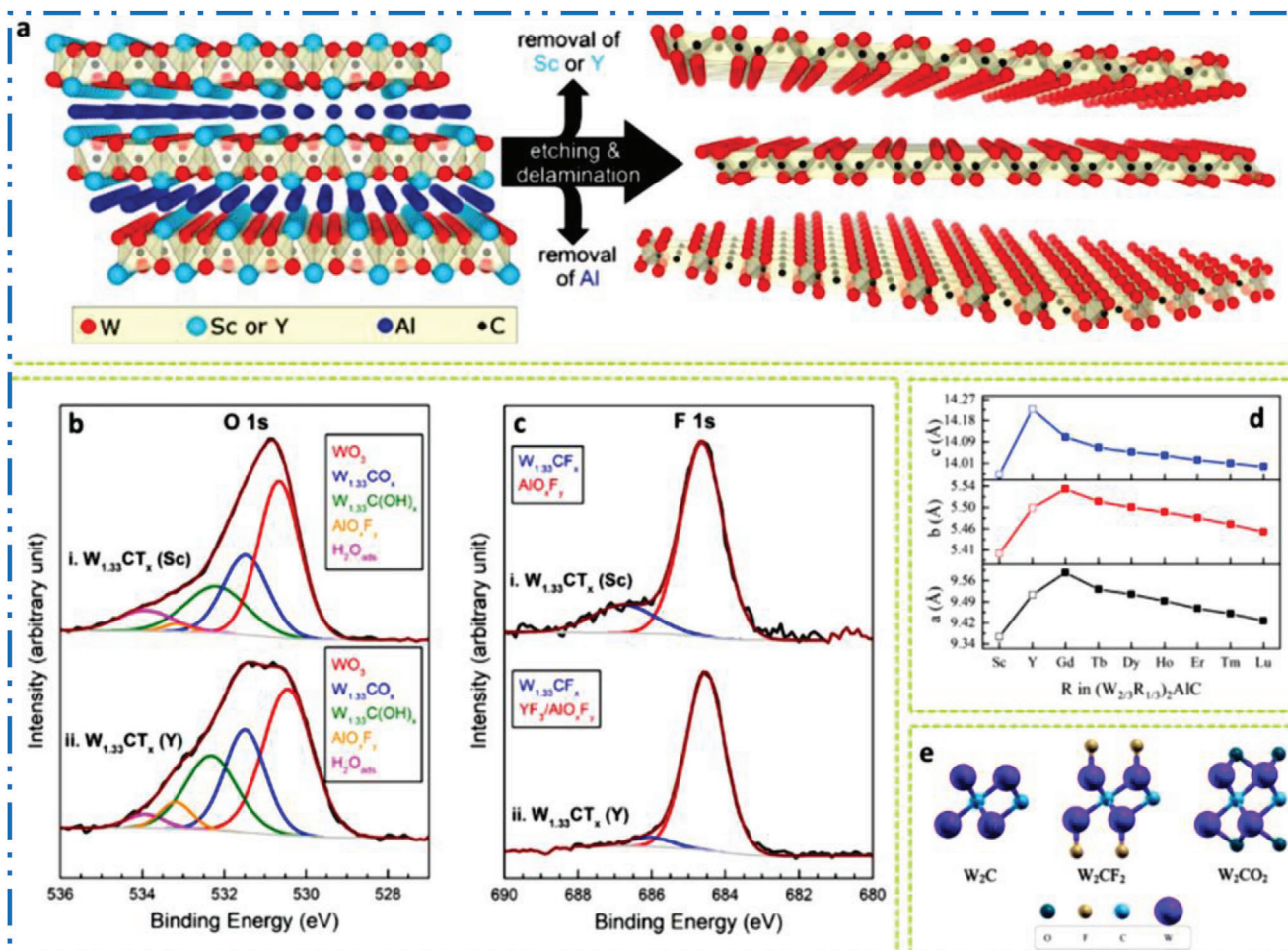


**Figure 17.** a) Scheme shows in-plane chemical ordering in  $(W_{2/3}Sc_{1/3})_2AlC$  or  $(W_{2/3}Y_{1/3})_2AlC$  (left panel), cause  $W_{1.33}C$  by controlled divacancies after etching as well as delamination (right panel), Reproduced with permission.<sup>[97]</sup> Copyright 2018, Wiley-VCH. XPS with curve fitting of (i)  $W_{1.33}CT_x(Sc)$  and (ii)  $W_{1.33}CT_x(Y)$  free-standing delaminated films for b) O1s and c) F1s, Reproduced with permission.<sup>[216]</sup> Copyright 2019, American Chemical Society, d) summary with evaluation of element-dependent lattice parameters of  $(W_{2/3}R_{1/3})_2AlC$  (R = Gd, Tb, Dy, Ho, Er, Tm, Lu) (closed symbols) compared to Ref. [220] (R = Sc, Y) (open symbols), Reproduced with permission.<sup>[217]</sup> Copyright 2021, Elsevier, e) Side view of optimized  $W_2C$ ,  $W_2CF_2$ , and  $W_2CO_2$  structural unit-cell, Reproduced with permission.<sup>[218]</sup> Copyright 2022, Elsevier.

studied that it is challenging to synthesize W-containing MAX precursors.<sup>[45]</sup> Notably, 17 elemental compositions comprising W-based  $M_2AX$  phases, for instance,  $W_2SC$ ,  $W_2AlN$ ,  $W_2SiN$ ,  $W_2SnN$ ,  $W_2InN$ ,  $W_2GeN$ ,  $W_2GaN$ , and  $W_2PbC$ , and other MAX phases, such as  $Cr_2SN$ ,  $V_2SN$ ,  $Mo_2SiN$ ,  $Mo_2SC$ ,  $Mo_2GeN$ ,  $Mo_2InN$ ,  $Mo_2AlN$ , as well as  $Mo_2SnN$  have demonstrated inclination to create unstable phases.<sup>[212]</sup> Hence, rather than a typical MAX phase where only one TM is added, quaternary i-MAX hybrid phases may be constructed to have a common equation of  $(M[1]_{2/3}M[2]_{1/3})_2AlC$ . By deliberately including M2 in a 1:2 ratio into the M1-dominated layer, alloying MAX precursor phase in this situation can produce in-plane chemically ordered configurations.<sup>[213]</sup> Stability of i-MAX hybrid structures may be anticipated when first-principles computations based on DFT are used, which opens up the prospect of producing i-MAX precursor experimentally.<sup>[95,214]</sup> Reliant on etching circumstances, such as i-MAX can produce either  $(M1_{2/3}M2_{1/3})_2C$  or  $M1_{1.33}C$  as 2D MXene NMs products.<sup>[97]</sup> Exploration for i-MAX was extended to rare-earth (RE) elements, for example, Pr, Ce,

Nd, Gd, Sm, Tb, Ho, Dy, Tm, Er, and Lu, in  $(Mo_{2/3}RE_{1/3})_2AlC$  hybrid phase,<sup>[215]</sup> increasing the moiety of MAX precursor into new dimension. Computational approaches have served as theoretical guides in this expansion. By DFT study of more than 18 compositions of  $(W_{2/3}M2_{1/3})_2AlC$ , where  $M2 = Sc, Y (W)$ , and  $A = Al, Si, Ga, Ge, In, and Sn$ , Meshkian<sup>[97]</sup> expected a phase stability. For experimental synthesis, the quaternary i-MAX  $(W_{2/3}Sc_{1/3})_2AlC$  and  $(W_{2/3}Y_{1/3})_2AlC$  phases were determined to be the very stable (Figure 17a). Sc and Y were effectively removed using HF acid or a solution of LiF/HCl, afterward TBAOH, producing 2D  $W_{1.33}C$  with ordered divacancies. Different quantities of surface terminations were depicted in the fitted XPS peaks for O1s (Figure 17b) and F1s (Figure 17c) for i)  $W_{1.33}CT_x(Sc)$  and ii)  $W_{1.33}CT_x(Y)$ .<sup>[216]</sup> The feasibility of filling the M2 positions of i-MAX (Figure 17d) with lanthanide elements (Gd, Tb, Dy, Ho, Er, Tm, and Lu) in place of Sc/Y was also examined.<sup>[217]</sup> In a nutshell, although rare-earth metals “R” = Lu behaved paramagnetically, R = Gd exhibited linear antiferromagnetic characteristics.

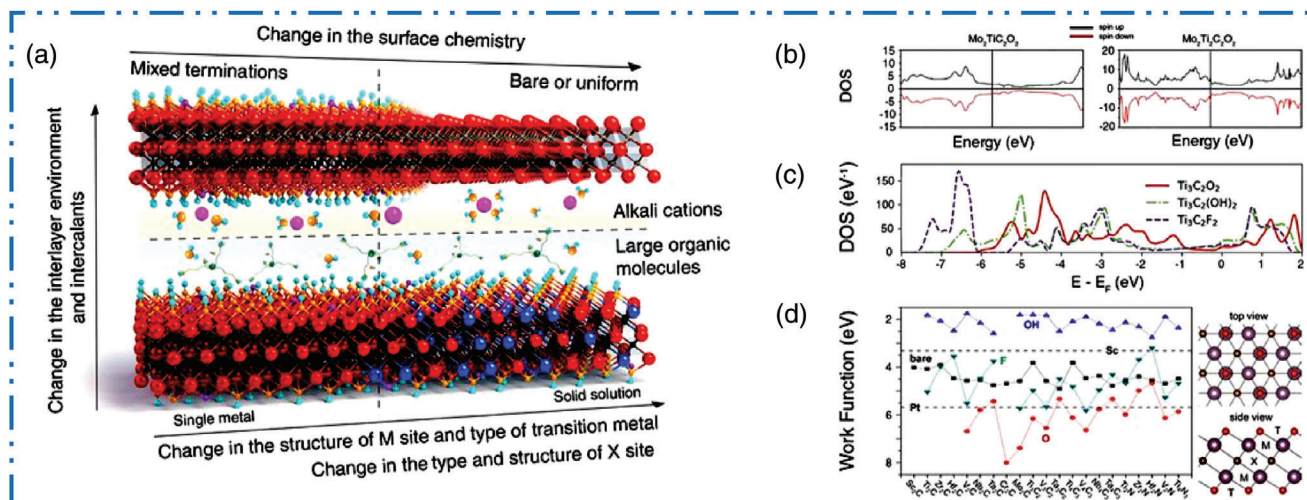


**Figure 18.** a) Scheme shows of different compositional and structural factors showing electronic as well as optical properties of MXene NMs, b) DOS, illustrating the result of MXene configuration, c) DOS shows a cause of surface chemistry on electronic properties of MXene NMs, and d) reliance of a work function of MXene NMs on their surface chemistry. Reproduced with permission.<sup>[34]</sup> Copyright 2021, American Association for the Advancement of Science (AAAS).

### 3.11. Double Transition Metal MXenes Synthesis

The idea of alloying has been widely used to incorporate useful metals and enhance the characteristics of original NMs. According to analysis of the Cr–Ti–Al–C<sup>[101]</sup> as well as Mo–Ti–Al–C<sup>[219]</sup> structures, metal alloying on initial MAX precursors is a widespread practice. Other techniques, like as microwave heating, SPS, and the arc-melting approach have also been effective in doping MAX phases. Nonetheless, introducing secondary precursor metals by elemental replacement in recognized crystal configurations is the normal standard in the formation of multiple metal MAX phases.<sup>[105,220]</sup> The (Cr<sub>2/3</sub>Ti<sub>1/3</sub>)<sub>3</sub>AlC<sub>2</sub> is a quaternary MAX precursor relied on M3-AX<sub>2</sub> lattice where two M elements (Cr/Ti) generated an o-MAX out-of-plane ordering phase that is now referred to as the o-MAX precursor.<sup>[221]</sup> In the meanwhile, M2-AX phase revealed the in-plane chemical arrangement in M elements with the same 2:1 ratio, thus the name i-MAX phase.<sup>[95]</sup> Etching of i-MAX precursors yields 2D NMs with ordered divacancies as opposed to o-MAX precursor, where the structure is retained in the subsequent MXene NMs. Further investigations of metal combinations inside as well as outside of IIIB–VIB family were exhaustively looked for after the current finding of recently studied MAX precursors. Thermodynamic stability of M<sub>5</sub>AlC<sub>4</sub> MAX precursors with M04 M00 AlC<sub>4</sub> compositions was predicted using DFT calculations (M0 and M00 were Zr, Hf, Ta, Ti, V, Nb, Mo, Sc, and W). According to Deysher and group mates analysis's of the precise formation energy, compositions based on Hf, Zr, and Ta should form with more stability than compositions comprising W and Mo. It is interesting to note that unconventional metals have also had achievement creating MAX with greater magnetic characteristics. According to a systematic theoretical research of alloying Cr<sub>2</sub>AC (A = Al, Ge) with Mn, the resulting phases have varied magnetic orderings based on the Cr/Mn ratio as well as internal ordering. Another work effectively formulated for Mn and Fe substituted in place of Cr<sub>2</sub>AlC utilizing microwave heating and SPS.<sup>[38,228]</sup>

### 3.12. Non-IIIB to VIB Metal Group Synthesis

Majority of known 2D MXene NMs employed M as an early TM from group-(III–VI)B. Notably, only MXene members have excellent B.G.s for semiconducting qualities such as Sc<sub>2</sub>C(OH)<sub>2</sub> (IIIB), Y<sub>2</sub>C(OH)<sub>2</sub> (IIIB), and Cr<sub>2</sub>TiC<sub>2</sub>(OH)<sub>2</sub>.<sup>[155,223,224]</sup> Lutetium (Lu) is a family of group-IIIB lanthanide series that has recently demonstrated potential benefits like Lu-MXene and Lu<sub>2</sub>C. Lu-MXene NMs with fluorine and hydroxyl terminated topologies are discovered to be useful as semiconductors in vis, and NIR optical devices.<sup>[225]</sup> Ingason et al.<sup>[226]</sup> impulse is to investigate stable but uncharted MAX phases led to the theoretical prediction and fabrication of Mn<sub>2</sub>GaC. By adopting heteroepitaxial thin film production, Mn effectively inserted in a MAX precursor, is showing the homogenous elemental layers and atomic arrangement of Mn, Ga, and C. In next section we will explain the theory and experimental demonstration of MXene general properties.<sup>[37]</sup>

## 4. Theory and Experimental Demonstration of Non-Ti MXene General Properties

### 4.1. Electronic Properties

MXene composition, structure, surface chemistry, with interlayer chemistry all affect their physical and (electro)chemical features (Figure 18a). The majority of 2D MXene NMs that behave like metals in terms of electron transport, with linearly decreasing its resistivity with temperature ( $dR/dT > 0$ ).<sup>[125,227]</sup> Changing the TM type and M site's structure in MXene NMs can lead to a negative temperature dependency of resistivity ( $dR/dT < 0$ ), giving rise to MXene NMs that behave like semiconductors.<sup>[121]</sup> These later include Mo<sub>2</sub>CT<sub>x</sub>, Nb<sub>2</sub>CT<sub>x</sub>, and V<sub>2</sub>CT<sub>x</sub> as examples.<sup>[199]</sup> Additionally, the 2D Mo<sub>2</sub>TiC<sub>2</sub>T<sub>x</sub> o-MXene NMs exhibited semiconductor-like behavior.<sup>[228]</sup> A sample of how the M-site structure might alter DOS of MXene NMs is shown in Figure 18b. It is projected that all 2D MXene NMs without surface terminations

functioned as metallic conductors with carriers made of free TM electrons.<sup>[227]</sup> Surface terminations, in contrast to ordinary metals, can alter DOS and shift Fermi level, make them electrically adjustable (Figure 18c).<sup>[229]</sup> A switch from metallic to semiconducting B.G opening, and a wide range in their work functions have all been anticipated for various MXenes other than  $\text{Ti}_3\text{C}_2\text{T}_x$  (Figure 18d).<sup>[230]</sup>

$\text{Nb}_2\text{CT}_x$  ( $\text{T}_x = \text{Se}, \text{S}, \text{or NH}$ ) has shown superconductivity, on the other hand, nonterminated or O-based terminated ML  $\text{Nb}_2\text{C}$  did not show a superconducting transition.<sup>[39]</sup> Thermoelectric characteristics and heat transport are similarly impacted by MXene surface terminations.<sup>[231]</sup> Electrical properties of ML and films are also impacted by the intercalants that are frequently utilized for delamination.<sup>[121]</sup> Tetrabutylammonium ( $\text{TBA}^+$ ) and other large organic cations are intercalated in the 2D MXene-based nanoflakes, resulting in a significant interlayer gap.<sup>[232]</sup> This separation prevents interflake electron hopping; make the resulting films less conductive. By contrast, the high conductivity of MXenes and narrow interlayer distance are often maintained by intercalated alkali cations.<sup>[233]</sup> For example,  $\text{Mo}_2\text{TiC}_2\text{T}_x$  underwent a change from band semiconducting ( $-dR/dT$ ) to metallic performance as a result of the deintercalation of water and  $\text{TBA}^+$ .<sup>[121]</sup> Additionally influencing a physical characteristics of 2D MXene NMs and their chemical stability are a flake size, stoichiometry, surface chemistry, and point defects, majority of which are vacancies in M and C sublattices that are either inherited from the precursor or produced by etching.<sup>[234]</sup> Greater intraflake electron transport and chemical stability are demonstrated by larger, defect-free 2D MXenes flakes, and the conductivity of these materials can exceed  $20\,000\text{ S cm}^{-1}$ .<sup>[74]</sup>

## 4.2. Magnetic Properties

Magnetic characteristics of 2D MXene NMs are also intriguing based on different investigations techniques. Therefore, MXenes with desirable magnetic characteristics, especially of antiferromagnetic nature, were expected to be possible by tuning M site of o-MXene NMs via altering the outer-layer TMs ( $\text{M}''$ ).<sup>[146]</sup> For o-MXene NMs with Mn in intermediate layer and Mn nitrides, ferromagnetism was anticipated.<sup>[146]</sup> At about 30 to 35 K, a magnetic glass transition in  $\text{Cr}_2\text{TiC}_2\text{T}_x$  was examined.<sup>[235]</sup> Theoretical forecasts continue to offer direction for prospective compositions and structures. As, in definite simulated o-MXene NMs, the surface  $\text{M}'$  layers are under octahedral crystal force fields while a central  $\text{M}''$  layers are not spin-polarized, causing band splitting in their 3D orbitals moreover, so, a net spin moment showing magnetic order of o-MXene NM.<sup>[146]</sup> Liu et al.<sup>[236]</sup> developed a crystal field theory-based model to calculate a magnetic property of MXene NMs, as well as findings demonstrated that  $\text{Mn}_2\text{NT}_x$  acts as a highly ferromagnetic material at ground state, though the magnetic nature disappeared when surface groups are present. The 2D  $\text{Cr}_2\text{C}$ ,  $\text{Cr}_2\text{N}$ ,  $\text{Ta}_3\text{C}_2$ , and  $\text{Cr}_3\text{C}_2$  MXene NMs are regarded as a ferromagnetic in nature that can be stripped from their MAX phase.<sup>[237,238]</sup> Single layer  $\text{Mn}_2\text{C}$  MXenes are antiferromagnetic with high Neel temperature of 720 K, according to theoretical estimates.<sup>[239]</sup> Surface functionalization with F, Cl, and OH, converts it to a ferromagnetic state with a high Curie temperature (520 K).<sup>[240]</sup> A few MXene NMs, such as  $\text{Cr}_3\text{C}_2$  and  $\text{Mn}_2\text{C}$ , are just

theoretically predicted and have not been synthesized experimentally till date. He et al.<sup>[240]</sup> described a magnetic characteristics of the 2D MXene NMs ( $\text{T} = \text{F}, \text{Cl}, \text{OH}, \text{O}, \text{and H}$ ) based on a theoretical analysis. MXenes containing functional groups having formal charges (F, Cl, and OH) preserve a ferromagnetic ground state following functionalization, but other MXenes turned into non-magnetic as they are symmetrically functionalized on their surface. Crystal strain has significant impact on crystal magnetism, according to theoretical investigations. Ion doping and vacancy introduction were proposed as two key ways for controlling its magnetic characteristics.<sup>[241]</sup>

## 4.3. Optical Properties

In a vis and NIR range, MXene NMs demonstrated longitudinal and transversal surface plasmon types; it is demonstrated that transverse plasmons are independent of the lateral dimension of the nanoflakes.<sup>[242]</sup> As interband transitions, they also reveal high UV-absorption. Types as well as configuration of M and X sites, and stoichiometry of surface  $\text{T}_x$ , all affect the optical characteristics of MXenes. Figure 19a,b demonstrates that certain MXenes contain plasmonic peaks that span the whole vis–NIR spectrum area<sup>[243]</sup> and plasmonic hues in transmission (colloidal solution or thin film) and reflection (solid-state ML films).<sup>[125]</sup> Generally, significant excitation peaks in MXenes' optical spectra go to high energies when their  $n$ -value is reduced.<sup>[243]</sup> In comparison,  $\text{V}_2\text{CT}_x$  has a greenish blue color in transmission and a brownish gold color in reflection, with no absorption peak in UV–vis–NIR band area.<sup>[244]</sup> The  $\text{V}_2\text{CT}_x$  has shown a larger level of value.<sup>[245]</sup> Figure 19c illustrates how different compositions of the  $(\text{Ti}, \text{Nb})_2\text{CT}_x$  and  $(\text{Ti}, \text{V})_2\text{CT}_x$  structures exhibit varied plasmonic hues as a consequence of changing the  $\text{M}':\text{M}''$  ratio in solid solution MXene NMs.<sup>[110,246]</sup> Figure 19d shows UV–vis–NIR transmittance spectra from 300 to 2500 nm for MXene thin films.<sup>[34]</sup>

## 4.4. Mechanical Properties

Although early analysis indicated that MXenes would have a high elastic modulus like bulk carbides<sup>[247]</sup> and experimental study of the 2D MXene NMs mechanical properties are only now at beginning.<sup>[248]</sup> The SL flakes of  $\text{Nb}_4\text{C}_3\text{T}_x$  MXene NMs were experimentally examined in terms of fundamental mechanical characteristics using AFM nanoindentation.<sup>[249]</sup> As a result subsistence of point defects with  $\text{T}_x$ , a studied modulus of SL  $\text{Nb}_4\text{C}_3\text{T}_x$  only reached 0.39 TPa,<sup>[250]</sup> which is still below theoretically supposed limit.<sup>[251]</sup> The  $\text{Nb}_4\text{C}_3\text{T}_x$  has a breaking strength of  $26 \pm 1.6\text{ GPa}$ . Figure 20a,b shows a tensile stress versus strain curves of the  $\text{Ti}_3\text{C}_2\text{T}_x$  MXenes based thin films with different thickness formed by vacuum-assisted filtration and blade coating, and force–deflection curves of a bilayer 2D  $\text{Ti}_3\text{C}_2\text{T}_x$  nanoflakes at different loads. Figure 20c shows the comparison of the effective Young's moduli.<sup>[34]</sup> The published Young's modulus values of numerous 2D NMs,<sup>[250]</sup> incorporated into the recently found vapor-grown  $\text{MoSi}_2\text{N}_4$  material, are compared in Figure 20c.<sup>[252]</sup> The in-plane Young's modulus of nitride-technique based MXene NMs is projected to be superior than that of carbide MXene NMs.<sup>[253]</sup>



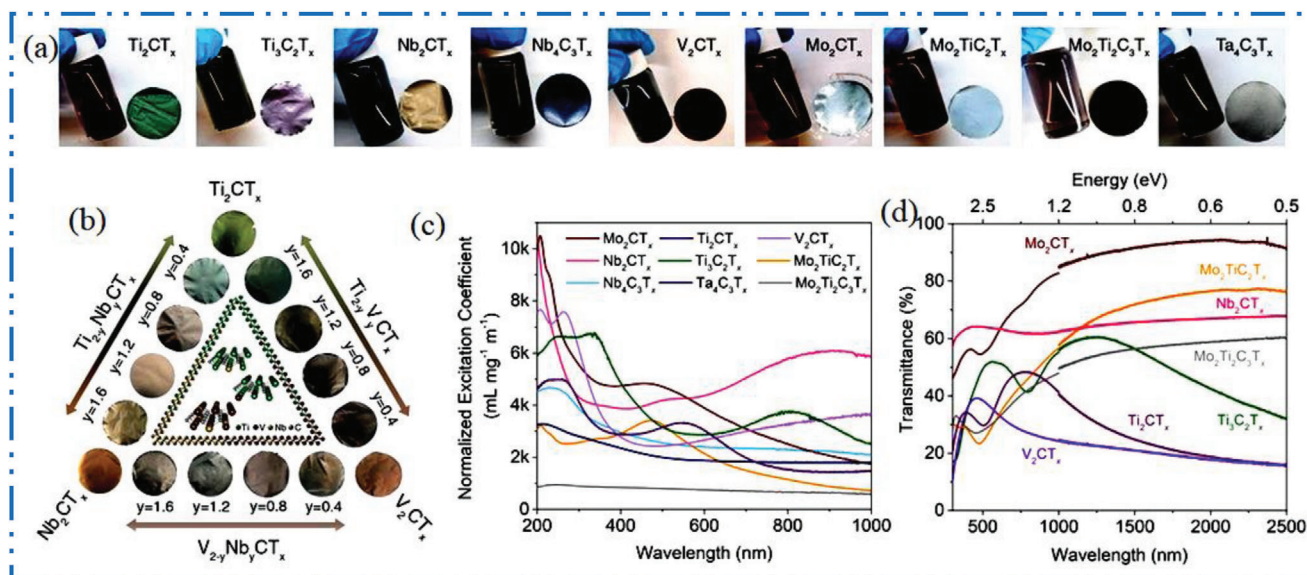


**Figure 19.** a) Color of colloidal solutions of a range of MXene NMs and their analogous freestanding films. b) Photographs of three  $M'_{2-y}M''_yCT_x$  solid solution schemes, c) UV-vis-NIR optical extinction properties of aqueous dispersions of various TMCs, d) UV-vis-NIR transmittance spectra from 300 to 2500 nm for MXene thin films. Reproduced with permission.<sup>[34]</sup> Copyright 2021, American Association for the Advancement of Science (AAAS).

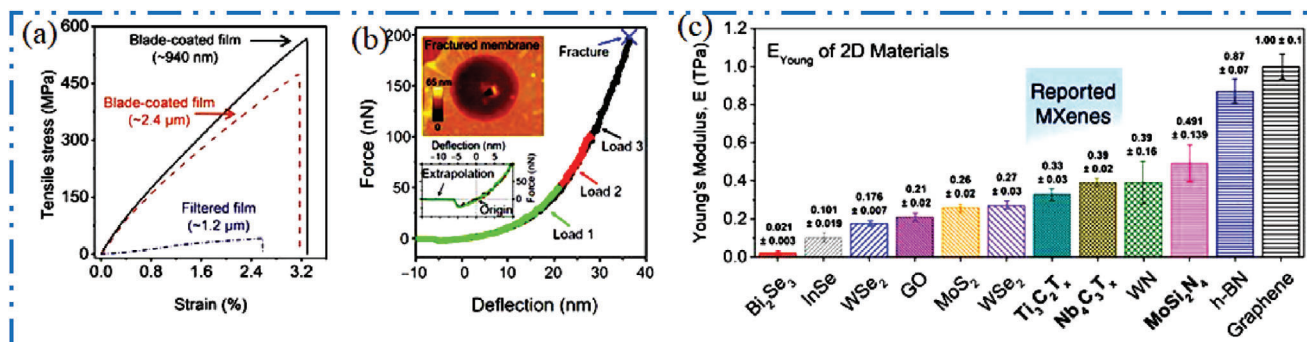


**Figure 20.** a) Tensile stress versus strain curves of  $Ti_3C_2T_x$  films with different thickness formed by vacuum-assisted filtration and blade coating. b) Force-deflection curves of a bilayer  $Ti_3C_2T_x$  nanoflake at different loads. c) Comparison of the effective Young's moduli. Reproduced with permission.<sup>[34]</sup> Copyright 2021, American Association for the Advancement of Science (AAAS).

#### 4.5. Topological Insulator Properties

Despite the fact that some functionalized 2D MXene NMs were anticipated to have a 2D topological insulator (TI) nature, in which electrons travel alongside an edge states, allowing in dissipation-free transport appropriate for low-power electronic devices. Relativistic spin-orbital coupling (SOC) can cause 2D TI phase, which has a substantial impact on electronic configuration of NMs containing heavy elements. The Mo, W, Ti, Zr, and Hf-atoms make up the majority of observed TIs MXenes. For instance, O-functionalized  $M_2CO_2$  ( $M = W, Mo, \text{ and } Cr$ ) are 2D TIs with significant SOC-induced B.Gs, with  $W_2CO_2$  computed using the GGA (HSE06) functional reaching 0.194 (0.472) eV (Figure 21a).

MLs phases and external disturbances not disrupt the 2D MXene NMs band structure, which has been proven. Si et al. as well as Khazaei independently studied the occurrence of the 2D

TI phase in MXenes with double TM elements, like  $Mo_2MC_2O_2$  ( $M = Zr, Ti, \text{ or } Hf$ ) (Figure 21b), whereas Khazaei also explored  $W_2MC_2O_2$ .<sup>[255,256]</sup> The  $Mo_2MC_2O_2$  has huge gaps of 0.1–0.2 eV depending on the “M”-atoms, while  $W_2HfC_2O_2$  is projected to have the greatest B.G of 0.285 eV (0.409 eV at the HSE06 level). In  $Mo_2M_2C_3O_2$  ( $M = Ti, Zr, \text{ or } Hf$ ), the quantum spin Hall phase was verified, with a range of M-atoms contributing to SOC induced B.G of 38–152 meV.<sup>[257]</sup> Recently, Liang et al. discovered that nitride type  $Zr_3N_2F_2$  and  $Hf_3N_2F_2$  MXene are transformed into TI by applying a lattice strain.<sup>[258]</sup> As transfer of charge, substitution doping, and proximity induced effects in  $Sc_2C(OH)_2$  MXene make it a novel form of s-pd band inversion TIs that enters into the TIs phase when an electric field is applied. The almost free electron states revealed by parabolic energy dispersion in the  $Sc_2C(OH)_2$  are suitable surface transport channels accountable for strong carrier mobility. Such states are near and above Fermi level, with no partial contributions from

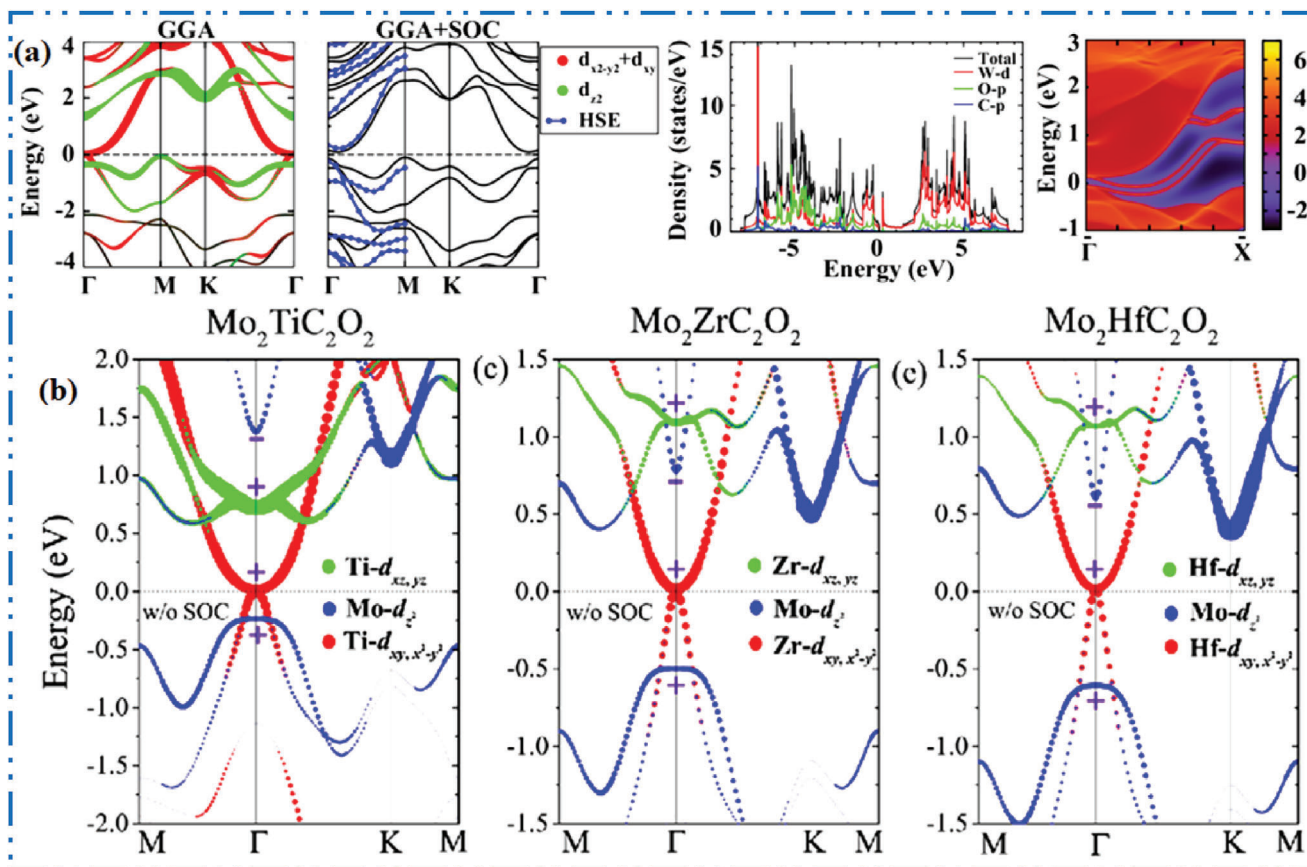


**Figure 21.** Band structures of a)  $\text{W}_2\text{CO}_2$ , Reproduced with permission.<sup>[254]</sup> Copyright 2015, American Physical Society, Cornell University Press, b) without/with SOC, and respected edge states, Reproduced with permission.<sup>[255]</sup> Copyright 2016, American Chemical Society.

any elements. The above materials were previously discovered in early tests with mixed surface  $\text{T}_x$ , and one of the recommended approaches for practically constructing TIs MXenes is careful regulation of surface  $\text{T}_x$  of oxygen terminated  $\text{Mo}_2\text{CT}_x$  during synthesis.<sup>[259]</sup> In next section we will explain in detail about each non-Ti MXenes NMs properties individually.

#### 4.6. High-Entropy 2D MXene NMs

First-principles calculations show the significance of high configurational entropy in equimolar multielements in producing pure and stable phases of multiprinciple elements (MPEs) MAX phases and link the synthesizability of quaternary high-entropy MAX to an entropy-driven stabilization. The efficient synthesis of MAX and MXene materials with high entropy by maximizing the configurational entropy to stabilize (near) equimolar mixtures in a manner similar to that in other disordered multicomponent systems (e.g., bulk ceramics and metals). The increasing family of MXenes now has a broad compositional space that may be investigated for uses such as energy storage, catalysis, and microstructural stability in harsh settings. This exotic subgroup of high entropy MPE MXenes was successfully synthesized. Furthermore, future modifications to the electrochemical, catalytic, electrical, and magnetic characteristics of MXenes may greatly

benefit from knowledge of the control over the composition of each transition metal layer. The development of topological insulator MXenes have not yet been synthesized but are predicted in theoretical studies,<sup>[260,261]</sup> may be further made possible by a particular choice of multiple constituent transition metals. This is due to higher degrees of freedom in component selectivity and phase formation when using more than one transition metal in MXenes. The vast compositional space and the potential for entropic stabilization in the high-entropy MAX and MXene phases present a variety of computational difficulties and opportunities.

The quantitative calculation of entropy, prediction of thermochemical properties, transition temperatures, and investigation of their transport properties are some intriguing questions that can be addressed by combining traditional modeling techniques with recent developments in big data analytics. This will help us better understand the mechanisms affecting the mechanisms affecting their synthesizability. With the use of molecular dynamics, which can illuminate the diffusion rates in disordered materials, the kinetic features may be investigated. A useful source of information on the durations and stability of metastable phases under various operating conditions can be found in recent data-driven methodologies. Overall, the enormous amount of synthetic and experimental data sets that will be produced offers enormous opportunities for artificial intelligence and machine learning to pinpoint crucial trends for quickening the process of



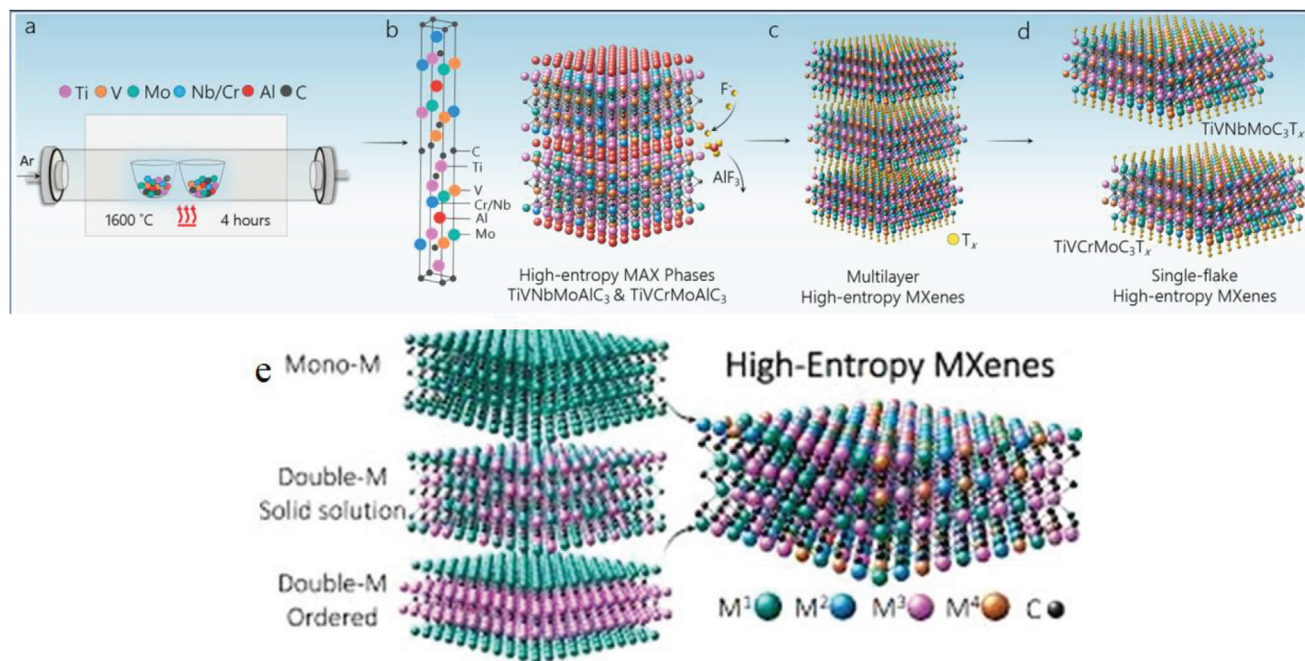


**Figure 22.** Schematic for the synthesis of high-entropy MAX and MXenes. a) Reactive sintering of high-entropy MAX phases. b) MAX phase unit cell (left) of  $M^1M^2M^3M^4AlC_3$  with elements Ti (pink), V (orange), Nb or Cr (blue), Mo (green), Al (red), and C (black). c) Selective etching of Al layer by HF to synthesize multilayer high-entropy MXenes. d) Delamination of multilayer MXenes is completed via organic molecule intercalants, which leads to the formation of single flakes of high-entropy MXenes  $TiVNbMoC_3T_x$  and  $TiVCrMoC_3T_x$ . e) High-entropy MXenes. Reproduced with permission.<sup>[34]</sup> Copyright 2021, American Association for the Advancement of Science (AAAS).

materials design and discovery in this significant class of high-entropy 2D materials.

Investigate the formation enthalpy ( $H$ ) of MAX compositions with reference to the combination of the most competitive phases,  $H_{cp} = H_{MAX \text{ phase}} - H_{competitive \text{ phases}}$ , in order to comprehend the synthesizability of high-entropy MAX and MXene phases and to quantify the thermodynamic stability of MAX compositions. The total energies of the phase structures and the total energies (per atom) of the bulk phases of M, A, and X elements should be used to compute the formation enthalpy of each phase. Then, a linear optimization procedure was used to determine which stage was the most competitive.<sup>[262]</sup> The relative stability of MAX phases in relation to the competitive phases is indicated by the negative  $H_{cp}$ . The likelihood of their experimental realization is often higher the more negative the enthalpy value. Configurational entropy, or statistically the number of discrete representative positions of the alloy constituents, which depends on the number of elements in the system under discussion, is a significant factor in the stabilization of multicomponent systems. For three and four transition-metal (three-M) MAX systems, the entropic contribution can be estimated using<sup>[263]</sup>

$$\Delta S_{mix} = -R \sum_{i=1}^k (x_i \ln x_i) \quad (1)$$

where  $x_i$  is the mole fraction of the  $i$ th component in a system with  $k$  total components.<sup>[264]</sup> The calculated entropic contribution at 1600 °C for three-M and four-M systems is  $-0.1773$  and  $-0.2238$  eV f.u.<sup>-1</sup>, respectively. Based on configurational entropy, the four-M MAX phase has more favorable entropy to form as

a single phase compared to the three-M one (Figure 22). The entropic stabilization explains the preference for four-M single-phase MAX phase as compared to three-M phases of MAX under similar synthesis conditions. Note, however, that our enthalpy calculations reveal that the three-M MAX is also synthesizable. Since we only used one synthesis temperature and duration (1600 °C, 4 h) for the sake of consistency, we cannot rule out the single-phase formation of the three-M MAX by further annealing at a desired temperature and duration. It is known that a lower contribution of configurational entropy can lead to the formation of a multiphase system (undesired phases) in the absence of post annealing treatment.<sup>[25]</sup> Further detailed studies on the nature of competing phases and formation pathways are required to understand the trends in synthesizability of high entropy MAX phases.

Two high-entropy  $TiVNbMoAlC_3$  and  $TiVCrMoAlC_3$  MAX phases were successfully synthesized by Nemani et al.,<sup>[265]</sup> and converted to high-entropy  $TiVNbMoC_3T_x$  and  $TiVCrMoC_3T_x$  MXenes with an equimolar percentage of Ti:V:Nb:Mo and Ti:V:Cr:Mo major transition metals. These high entropy MAX phases were created via conventional pressureless reactive sintering, and their corresponding single- to few-layer MXenes were created by selective etching with hydrofluoric acid and tetramethylammonium hydroxide delamination. XRD, SEM, and STEM were used to confirm the effective synthesis of single to few layer high-entropy MXenes from high-entropy MAX phases and their purity. Additionally, using XPS and EDS in SEM, researchers were able to confirm the bonding properties in high entropy MXenes and pinpoint the equimolar composition of transition metals. The elemental mapping using EDS in STEM was used to determine the equimolar distribution of transition metals in the transition



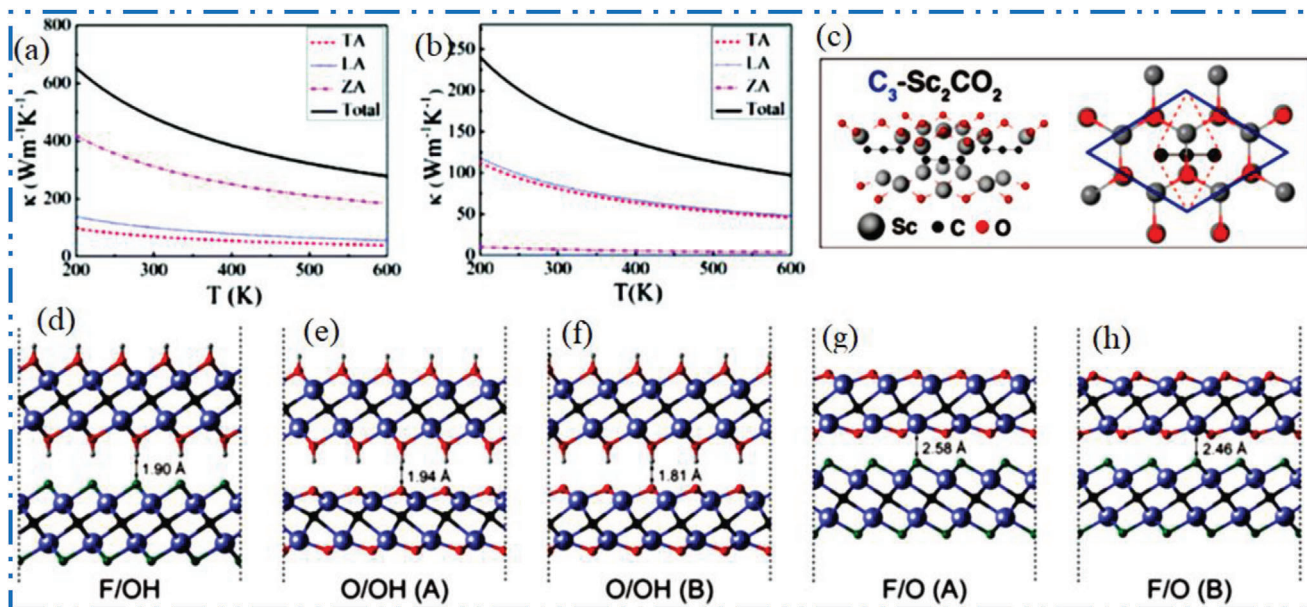


**Figure 23.** Thermal conductivities of a)  $\text{Sc}_2\text{CF}_2$  and b)  $\text{Sc}_2\text{C}(\text{OH})_2$  along armchair directions, Reproduced with permission.<sup>[270]</sup> Copyright 2016, Royal Society of Chemistry, c) structure and energetic stability of  $\text{C}_3\text{-Sc}_2\text{CO}_2$ , Reproduced with permission.<sup>[269]</sup> Copyright 2021, Wiley, side view of d) F/OH, e) O/OH (A), f) O/OH (B), g) F/O (A), and h) F/O (B) hetero-systems, Reproduced with permission.<sup>[223]</sup> Copyright 2015, American Chemical Society.

metal layers in the delaminated single-to-few layer MXenes. First-principles calculations show the significance of high configurational entropy in equimolar multielements creating pure and stable phases of MPE MAX phases and link the synthesizability of quaternary high-entropy MAX to an entropy-driven stabilization. Maximizing configurational entropy to stabilize (near) equimolar mixtures in a manner similar to that in other disordered multi-component systems (e.g., bulk ceramics and metals) allowed for the successful synthesis of high-entropy MAX and MXene materials.

## 5. Applications of Non-Ti MXenes

### 5.1. Sc-MXene Applications

The few experimental experiments that have been examined for Sc-MXene have allowed systematic computational research to completely anticipate their characteristics. The characteristics of  $\text{Sc}_2\text{CT}_2$  ( $T = \text{F, OH, O, Cl}$ ) MXene NMs were studied using first-principles calculations.<sup>[266,267]</sup>  $\text{Sc}_2\text{C}(\text{SH})_2$ ,  $\text{Sc}_2\text{CCl}_2$ , and  $\text{Sc}_2\text{NO}_2$  were projected to be semiconductors whereas  $\text{Sc}_2\text{C}(\text{OH})_2$  and  $\text{Sc}_2\text{CF}_2$ , for instance, displayed advantageous optical absorption in the vis-light range.<sup>[268,269]</sup> Figure 23a,b shows the thermal characteristics of the semiconducting materials  $\text{Sc}_2\text{CF}_2$  and  $\text{Sc}_2\text{C}(\text{OH})_2$ ;  $\text{Sc}_2\text{CF}_2$  exhibited high thermal conductivity ( $472 \text{ W m}^{-1} \text{ K}^{-1}$ ). Although while  $\text{Sc}_2\text{C}(\text{OH})_2$  has a lower thermal conductivity ( $173 \text{ W m}^{-1} \text{ K}^{-1}$ ) and is less anisotropic than silver, it nevertheless outperforms the metal. Inspire by the ferroelectric hexagonal phase (hex- $\text{Sc}_2\text{CO}_2$ ) and antiferroelectric phase (AFE- $\text{Sc}_2\text{CO}_2$ ) of  $\text{Sc}_2\text{CO}_2$ , Bae et al.<sup>[269]</sup> developed a novel structural phase for  $\text{Sc}_2\text{-CO}_2$  MXenes NM with  $\text{C}_3$  unit ( $C2/m$  space group),  $\text{C}_3\text{-Sc}_2\text{CO}_2$  (Figure 23c). In contrast to hex- $\text{Sc}_2\text{CO}_2$  (trigonal symmetry) and AFE- $\text{Sc}_2\text{CO}_2$ , the  $\text{C}_3\text{-Sc}_2\text{CO}_2$  has a rhombic structure

with  $\text{C}_3$  structural units (oblique symmetry). The 2D electride insulator a novel reduced energy  $\text{C}_3$ -structure has demonstrated high applicability as anode NMs for LIBs. The SL  $\text{Sc}_2\text{CO}_2$  with asymmetric configuration was shown to be the most stable model in Type I, II, and III heterostructures of functionalized SL of  $\text{Sc}_2\text{CF}_2$ ,  $\text{Sc}_2\text{C}(\text{OH})_2$ , and  $\text{Sc}_2\text{CO}_2$ .<sup>[223]</sup> This is because of the many places where the O functional atom may be found. For the most stable geometries shown in Figure 23d–h, the heterojunctions between bilayers of  $\text{Sc}_2\text{CX}_2/\text{Sc}_2\text{CY}_2$  (where X/Y, X, and Y = F, OH, and O) were also assessed. It is possible to better comprehend the characteristics of Sc-MXenes that are practical to create before their production by utilizing computational approaches to determine their photonics, electronics, and optoelectronics features. Overall, it seems that the Sc-based MXene family has intriguing semiconducting characteristics that might be useful for optoelectronic devices. Nonetheless, given the cost and raw material restrictions, a detailed examination of their theoretical qualities should be given serious consideration before beginning any practical research. This will lessen the requirement to manufacture Sc-MXene NMs at a low cost for use in critical applications.

### 5.2. V-MXene Applications

Using a thermal image of 2D  $\text{V}_2\text{C}$  MXene NSs solution at various concentrations, photothermal presentation of vanadium carbide was assessed, and it was shown to be effective for photoacoustic and MRI-guided photothermal treatment of cancer.<sup>[149]</sup> In terms of energy storage,  $\text{V}_2\text{CT}_x$ 's theoretically determined specific capacity ( $125 \text{ mAh g}^{-1}$ ) stood out higher than  $\text{Nb}_2\text{CT}_x$  ( $110 \text{ mAh g}^{-1}$ ), industrial graphite, and  $\text{Ti}_2\text{C}$ .<sup>[271]</sup> There are many opportunities to investigate V-potential MXene NMs in further energy storage and conversion uses. In conclusion, several experimental

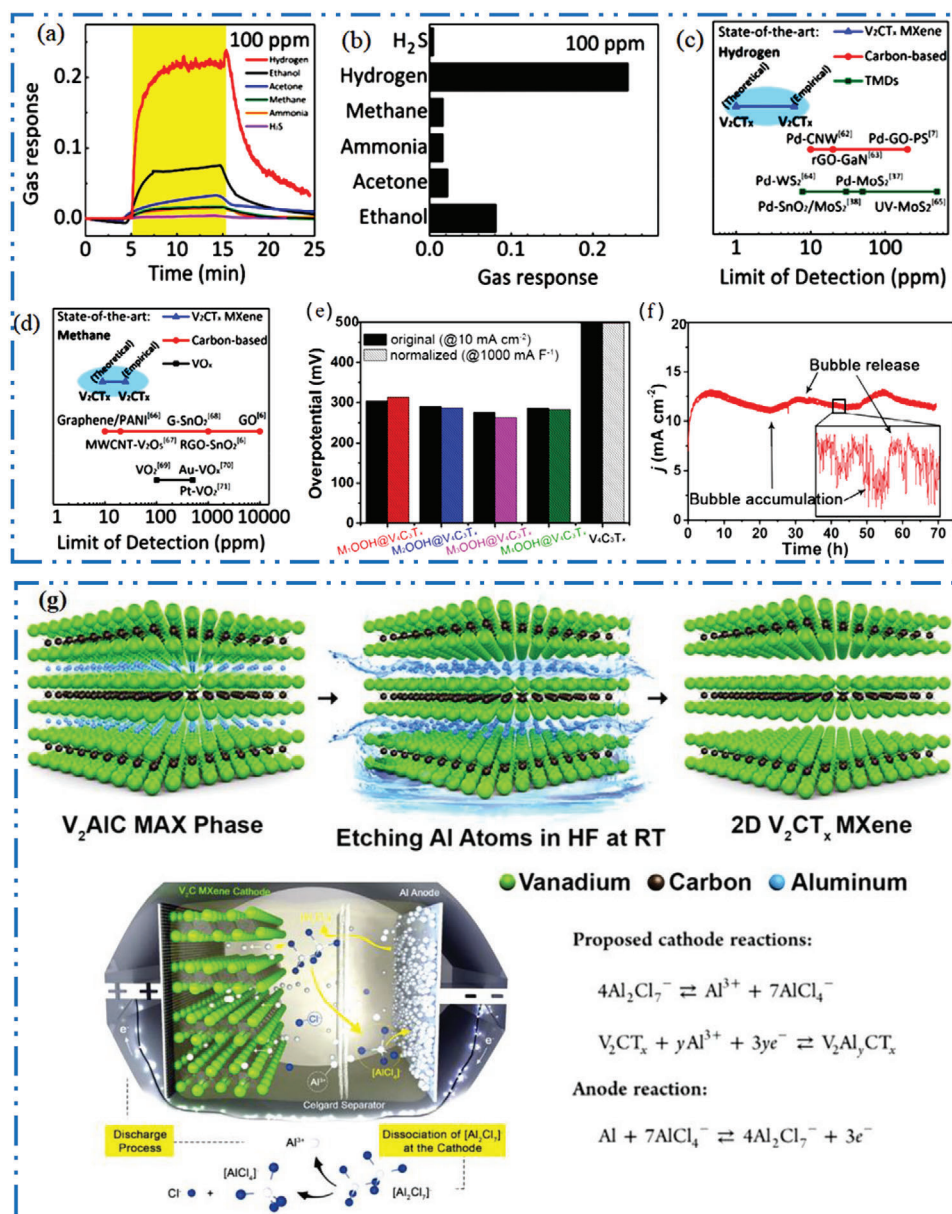


**Figure 24.** a,b) V<sub>2</sub>CT<sub>x</sub> sensor shows resistance variation at 100 ppm of H<sub>2</sub>, C<sub>2</sub>H<sub>6</sub>O, C<sub>3</sub>H<sub>8</sub>O, CH<sub>4</sub>, NH<sub>3</sub>, and H<sub>2</sub>S at RT, and summary of highest response, c,d) Comparison of limit of detection with other C- and V-based materials at RT for H<sub>2</sub> and methane, Reproduced with permission.<sup>[272]</sup> Copyright 2019, American Chemical Society, e)  $\eta$  and  $\eta_{\text{CdI}}$  of V<sub>2</sub>CT<sub>x</sub> and MOOH@V<sub>2</sub>CT<sub>x</sub>, f) CVs of M<sub>3</sub>OOH@V<sub>2</sub>CT<sub>x</sub>, Reproduced with permission.<sup>[273]</sup> Copyright 2020, Wiley, g) scheme of V<sub>2</sub>AlC to V<sub>2</sub>CT<sub>x</sub> production and ion battery, Reproduced with permission.<sup>[13]</sup> Copyright 2017, American Chemical Society.

investigations for creating the 2D V-MXene NMs without the use of HF have shown successful results. This may serve as motivation for producing alternative M-MXenes using less hazardous substances and simple procedures. Furthermore, doping techniques in V-MXenes have shown positive results in enhancing the substance's general characteristics. The M-MXene NMs can be used to test this method and introduce advantageous dopants in advanced uses. The remarkable sensitivity of a V<sub>2</sub>CT<sub>x</sub> MXene NMs-based gas sensor toward nonpolar gases was recently described (Figure 24a–d).

When hydrogen gas is present, then V<sub>2</sub>CT<sub>x</sub>-based NMs effectively detects it and their gas response is three times greater than

ethanol at 100 ppm at RT. For SNR = 3, it was calculated that the theoretical detection limits for hydrogen and methane were 1.3 and 25 ppm, respectively.<sup>[272]</sup> It is not yet completely understood how inert nonpolar gases are sensed. The gas sensing performance of V<sub>2</sub>CT<sub>x</sub> NM is noticeably different from that of Ti<sub>3</sub>C<sub>2</sub>T<sub>x</sub> MXene, in which the same group has previously examined.<sup>[274]</sup> Due to their broad range of gas-selectivity and tunability, the huge family of MXene NMs is suggested a very useful gas sensing platform. The obvious unanswered problems for their gas sensing mechanism are the functions of transition-metal species and the population of surface functional groups. The unique nine atomic multilayer V<sub>4</sub>C<sub>3</sub>T<sub>x</sub> was explored by Du et al. (Figure 24e,f).<sup>[273]</sup>



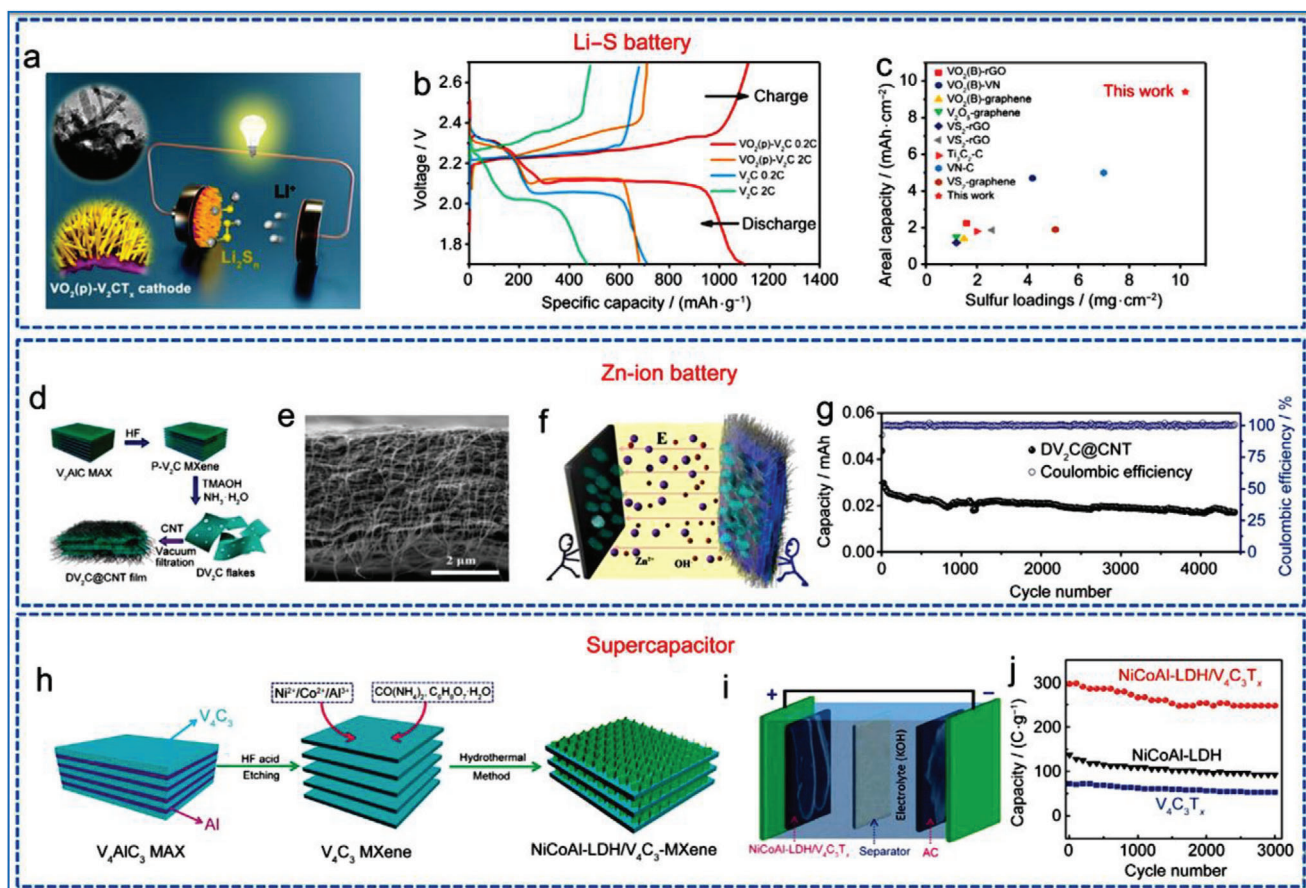


**Figure 25.** a) Scheme of  $\text{VO}_2(\text{p})\text{-V}_2\text{CT}_x$  cathode, b,c) Charge–discharge profiles, d) fabrication of delaminated freestanding film, e) SEM of  $\text{D-V}_2\text{C@CNT}$ , f) scheme of zinc hydroxide sulfate hydrate nanoflakes, and g,h) cycling performance and coulombic efficiency, and scheme of synthetic process composite. i) Scheme shows hybrid SC device, j) cycling performance of electrodes in 1 M KOH. Reproduced with permission.<sup>[203]</sup> Copyright 2020, Springer.

The nanohybrid with the optimum Ni/Fe ratio can achieve a current density of  $10\text{ mA cm}^{-2}$  at overpotential ( $\eta$ ) as low as 275.2 mV, which is superior to other MXene NMs based derivatives and similar to the majority of the state-of-the-art OER catalysts. We may imagine the prospective function of the  $\text{M}_4\text{X}_3$ -based MXene NMs as substrates for a variety of energy conversion and storage materials. It is demonstrated by variable physicochemical characteristics and high structural stability of these nanohybrids. In order to create an intercalation-type cathode material for Al batteries with outstanding cycle stability and high energy density, Vahidmohammadi et al.<sup>[13]</sup> showed that  $\text{V}_2\text{CT}_x$  NMs may reversibly intercalate  $\text{Al}^{3+}$  cations into their structures. Among the cathode materials for Al batteries that have been described so far,  $\text{V}_2\text{CT}_x$  NMs based electrodes have one of the greatest performances. The method they used to construct the unique ALB with the suggested charge–discharge mechanism at the liquid–solid boundary is schematically illustrated in Figure 24g. At a current density of  $100\text{ mA g}^{-1}$ , the TBAOH-FL- $\text{V}_2\text{CT}_x$  cathode produced unusually high specific capacities of more than  $300\text{ mAh g}^{-1}$ . As a result, our research created a new route for raising ALB performance. As a result, an ALB with an MXene-based composite cathode ( $\text{F-Ti}_3\text{C}_2\text{T}_x\text{@Ag}$ ) was created for another investigation. After 2000 cycles at a current density of  $0.5\text{ A g}^{-1}$ ,

the new ALB's discharge-specific capacity was around  $150\text{ mAh g}^{-1}$ .<sup>[275]</sup>

Rechargeable ZIBs, in addition to the typical battery types previously described are a battery technology that has drawn a lot of interest. In 2020, Venkatkarthick et al.<sup>[276]</sup> synthesized a  $\text{V}_2\text{O}_x\text{@V}_2\text{CT}_x$  that could serve as an efficient cathode material for aqueous ZIB. The prepared  $\text{V}_2\text{O}_x\text{@V}_2\text{CT}_x$  electrodes achieved an average optimum rate performance. Wang et al.<sup>[277]</sup> described a 3D-grid heterostructure made of paramontroseite- $\text{VO}_2$  ( $\text{VO}_2(\text{p})$ ) nanorods based cluster and 2D  $\text{V}_2\text{CT}_x$  MXene NM (Figure 25a). In contrast to other V-based cathode materials, the galvanostatic charge–discharge curves of cathode indicate strong discharge capacity performance (Figure 25b), and cathode has greater sulfur areal loading and bigger areal capacity of  $9.3\text{ mAh cm}^{-2}$  (Figure 25c).

Wang et al.<sup>[278]</sup> created a Zn-ion SCs electrode using a CNT network that was evenly mixed with 2D  $\text{V}_2\text{CT}_x$  MXene NMs (Figure 25d–f). The long-term cycling performance demonstrates a cycling life of over 4000 cycles at  $0.5\text{ A g}^{-1}$  current density with a Coulombic efficiency of  $\approx 100\%$  (Figure 25g). Researchers have showed that the structural stability of  $\text{V}_4\text{C}_3\text{T}_x$  is enhanced over  $\text{V}_2\text{CT}_x$  due to an increased number of layers, making it a suitable material for energy storage.<sup>[38]</sup> Wang et al.<sup>[279]</sup> created a new



supercapacitor heterostructure using Ni-Co-Al layered double hydroxide (NiCoAl-LDH) and 2D  $V_4C_3T_x$  MXene NM (Figure 25h,i). Their cycling stability of in 1 mol L<sup>-1</sup> KOH at a current density of 20 A g<sup>-1</sup> seems intact after 3000 cycles with a specific capacity of 248 C g<sup>-1</sup> (Figure 25j). The 2D V-MXene NMs also provide up new possibilities for white laser production and HER. It is also worth noting that V-MXene improves capacity when compared to the 2D V-MXene NMs. For example, Wang et al.<sup>[280]</sup> synthesized 2D  $(V_y, Ti_{1-y})_2CT_x$  NMs and investigated their applicability in LIBs. The addition of the heteroatom Ti to 2D  $(V_y, Ti_{1-y})_2CT_x$  NMs increases their reversible capacity. The 2D V-MXene NMs, like Mo-containing 2D MXene NMs, have restricted applicability. Han et al.<sup>[69]</sup> recently revealed that the electrical conductivity of  $Nb_yV_{2-y}CT_x$  film rises with increasing V content, resulting in improved EMI shielding efficacy.

### 5.3. Cr-MXene Applications

To predict catalytic performance and structural stability of  $Cr_2CO_2$  MXenes with TM alteration and carbon vacancy engineering, DFT simulations were assessed.<sup>[168]</sup> As weaker (25%) link between H atom and surface of  $Cr_2CO_2$ , the presence of carbon vacancies enhances HER activity. The bonding between the H atom and H<sub>2</sub> molecules on potential sites in  $Cr_2C$  was assessed by Yadav et al.<sup>[153]</sup> The sum of chemisorption (1.2 wt%), weak electrostatic interactions (3.2 wt%), and Kubas interaction (3.2 wt%) yields the reversible H<sub>2</sub> storage capacity of  $Cr_2C$  at 7.6 wt%. The issue still resides in making surface terminated Cr-MXenes, despite theoretical studies showing encouraging results. In conclusion, creating Cr-based MAX phases necessitates laborious techniques, departing from the tried-and-true MAX formulas. On the plus side, Cr-MAX phases are prepared using safer and less hazardous HF-free procedures instead of traditional ones. About 2D Cr-MXene NMs, its applicability for catalytic and magnetic activities is constrained. A huge potential may be concentrated on its synthesis and examination in many applications because of its cheaper cost and natural abundance.

### 5.4. Y-MXene Applications

Two different etching methods such as HF and DMSO delamination (sample A) and combined HCl as well as LiF solution (sample B), for  $YAl_3C_3$ ,<sup>[172]</sup> produced specific capacitances of 18 and 6 F g<sup>-1</sup>, correspondingly. Also, a positive slope from Mott-Schottky plot along with the negative flat-band potential (2.1 V vs Ag/AgNO<sub>3</sub>) show that  $Y_2CF_2$  exhibits n-type semiconductor behavior (1.9 eV B.G).<sup>[173]</sup> Nevertheless,  $Y_2CF_2$  was unstable and underwent oxidative degradation to generate fluorocarbon and carbonate species when used as a photocatalyst. Structural, electrical, optical, and thermal characteristics of Y-MXene<sup>[281]</sup> as well as their prospective uses have been researched using first-principles simulations. For instance, the  $Y_2C$  monolayer has a high theoretical specific capacity of 564 mAh g<sup>-1</sup>, a low diffusion barrier of 0.01 eV, and a substantial Na adsorption energy of  $\approx 0.32$  eV.<sup>[282]</sup> Therefore, Y-MXene has demonstrated good thermoelectric, electrochemical, and semiconductive capabilities when evaluated theoretically. In conclusion, it is still crucial to

conduct experimental assessments of the stability, surface functionalization, and characteristics of Y-based MXene NMs. Among the M-MXene NMs, yttrium continues to be the least researched metal. First-principles research has revealed the potential characteristics of Y-MXene. Yet, rigorous experimental evaluation and additional testing of these features in a variety of applications are still necessary before they can be compared to those of other M-MXenes.

### 5.5. Zr-MXene Applications

Metallic qualities were present in  $Zr_3C_2F_2$ ,  $Zr_3C_2O_2$ , and  $Zr_3C_2(OH)_2$ , with  $Zr_3C_2O_2$  containing highest mechanical strength (c11 value of 392.9 GPa).<sup>[177]</sup> In fact, it can influence the 2D MXene NMs general characteristics, and can result in optimal applications. Surface-terminated Zr-MXene was successfully tested in water-splitting,<sup>[283]</sup> electrocatalysis,<sup>[284]</sup> and batteries<sup>[285]</sup> using theoretical calculations. High-theoretical Na atom capacities computed at 474 and 326 mAh g<sup>-1</sup>, correspondingly,  $Zr_2CO_2$  and  $Zr_3C_2O_2$  function as metals and semiconductors.<sup>[285]</sup> In the meanwhile,  $Zr_2C$  (310 mAh g<sup>-1</sup>),  $Zr_2CO_2$  (266 mAh g<sup>-1</sup>),  $Zr_2CS_2$  (259 mAh g<sup>-1</sup>), and  $Zr_2CF_2$  (58 mAh g<sup>-1</sup>) have been predicted to have specific Li capacities.<sup>[286]</sup> This type of surface functionalization can offer a tactical method for forcing maximal functionalities onto any MXene. As a result, in situ chalcogenation (Se, S, and Te) and other approaches, such as coprecursor addition, can be researched in MXene NMs to further increase the conversion of highly desirable  $T_x$  functional groups.

### 5.6. Hf-MXene Applications

Based on first-principles DFT, theoretically studied  $T_x$  groups on  $Hf_3C_2T_2$  ( $T = F, O, OH$ ) projected that  $Hf_3C_2O_2$  would have a high mechanical strength.<sup>[55]</sup> Meanwhile, the OAS substitutions in Hf-MXene have adjustable characteristics that lead to a range of responses in achieving B.Gs that may be relevant for a number of applications.<sup>[184]</sup> A perfect hydrogen storage solution, Li/Hf<sub>2</sub>CF<sub>2</sub>, was made possible by Li-decoration on F-based  $T_x$  Hf-MXene NMs.<sup>[182]</sup> The Hf-MXene displayed reversible volumetric capacities of 1567 and 504 mAh cm<sup>-3</sup> used in LIBs and NIBs, correspondingly.<sup>[55]</sup> As a result, assessing Hf-MXenes NM in applications needing superior electrochemical and electrocatalytic capabilities is a wonderful option.

### 5.7. Nb-MXene Applications

In comparison to  $Ti_2C$  and  $Ti_3C_2$ , the 2D  $Nb_2C$ -based MXene NMs demonstrated the best K-ion capacitor performance with strong pseudocapacitive subject performances, quick kinetics, and long-lasting cycle stability.<sup>[287]</sup> Achieving a high energy density of 146.7 Wh kg<sup>-1</sup> (50.3 mAh g<sup>-1</sup> for 2.0 V),<sup>[288]</sup>  $Nb_2CT_x$  MXene beat its reported aqueous MXene equivalents. While F, O, and OH are the most often included termination groups because of the interaction between H<sub>2</sub>O and F<sup>-1</sup> and with bare  $Nb_2C$ ,<sup>[192]</sup> Cl, NH, Se, S, Br, and Te are also studied to see how they affect the MXene NMs' property that causes some of

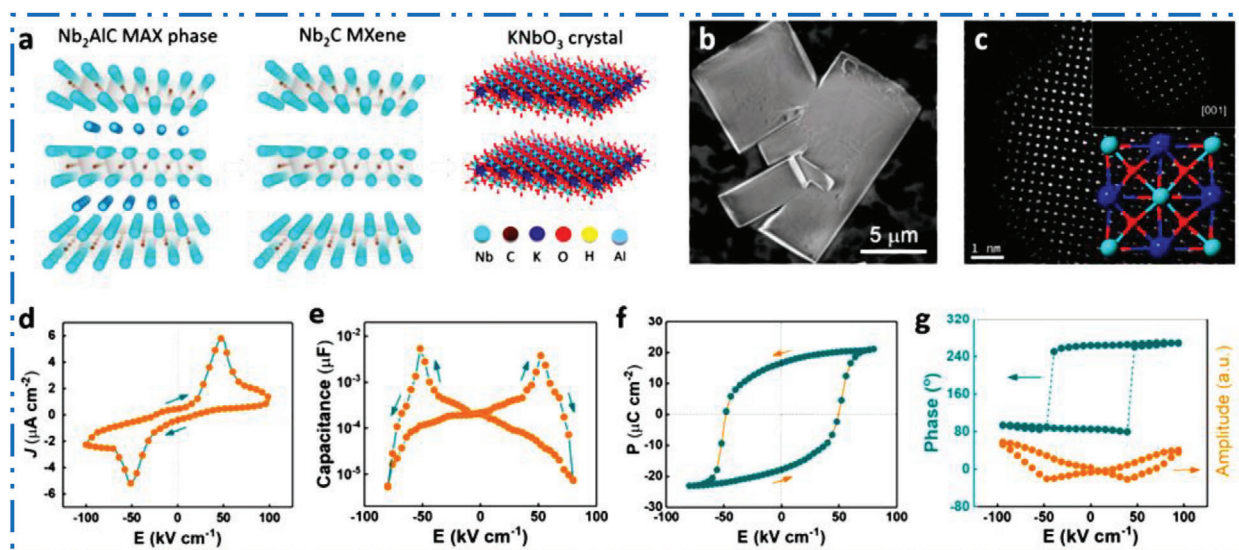


**Figure 26.** a) Crystal structure conversion of  $\text{Nb}_2\text{AlC}$  to  $\text{Nb}_2\text{CT}_x$  and M- $\text{KNbO}_3$  by hydrothermal conversion, b,c) SEM and TEM of M- $\text{KNbO}_3$ , and d–g) ferroelectric results of M- $\text{KNbO}_3$  crystals at RT. Reproduced with permission.<sup>[192]</sup> Copyright 2019, Wiley.

their devices uses.<sup>[289]</sup> Conduction band minimum of perovskite layer is greater or lower than the work function (WF) of O, OH, and F terminated  $\text{Nb}_2\text{CT}_x$ , which may be changed by varying the number of surface  $\text{T}_x$  of MXene NM.<sup>[290]</sup>  $\text{Nb}_2\text{CT}_x$  MXene NSs have successfully incorporated  $-\text{NH}_2$  groups on their surface, as shown by the core-level spectra N1s and F1s.<sup>[291]</sup> With this method, the WF may be adjusted to suit the desired minimum conduction band for perovskite. The Nb-based MXene NMs were tested thus far for a variety of uses, including photonics and optoelectronic devices,<sup>[292]</sup> metal ions sensing and fluorescence imaging,<sup>[293]</sup> medical implants,<sup>[294]</sup> radiotherapy,<sup>[295]</sup> batteries,<sup>[296]</sup> capacitors,<sup>[193]</sup> catalysts,<sup>[297]</sup> and hydrogen storage.<sup>[298]</sup> The Nb-MXene NMs' flexibility shows a promising qualities and applications that may compete with Ti-MXenes and other non-Ti MXene NMs.

Using  $\text{Nb}_2\text{CT}_x$  NM as a precursor material in a hydrothermal technique,  $\text{KNbO}_3$  ferroelectric crystals with a high aspect ratio and homogeneous shape have been created (Figure 26).<sup>[192]</sup> The  $\text{Nb}_2\text{CT}_x$  MXene was heated to 190 °C for 48 h in a KOH solution with sodium dodecyl sulfate (SDS) surfactant to undergo simultaneous oxidation and alkalization. Strong ferroelectric characteristics, such as a saturated polarization, a residual polarization, and a coercive field of 21  $\mu\text{C cm}^{-2}$ , 17  $\mu\text{C cm}^{-2}$ , and 50  $\text{kV cm}^{-1}$ , were present in the MXene-derived  $\text{KNbO}_3$  crystals at room temperature. When  $\text{Nb}_2\text{CT}_x$  MXene is substituted for commercial NbC powder under the identical conditions, cube-like  $\text{KNbO}_3$  powders with a nonuniform size distribution are produced. The final products' form is erratic in the absence of SDS surfactant. The 2D layered structure of  $\text{Nb}_2\text{CT}_x$  and the shape-modulation impact of SDS served as the foundation for the effective synthesis of high-aspect-ratio  $\text{KNbO}_3$  ferroelectric crystal. In essence, the 2D character of MXene is inherited by  $\text{KNbO}_3$ , leading to a highly rough crystal shape.

The capacity of 2D MXene NMs to absorb light effectively is considerably enhanced by surface plasmons vibrating at their 2D surfaces. The 2D MXene NMs have demonstrated excellent plas-

monic absorptions in the vis and IR regimes thus far. However, their potential utility in IR optoelectronic uses, such as photodiodes, has received only cursory attention. Furthermore, due to their inherent strong dark current, their comparatively poor resistivity has hampered their usage as photosensing materials. Therefore, Zhixiong Liu et al.<sup>[299]</sup> studied heterostructures built of  $\text{MAPbI}_3$  perovskite and 2D  $\text{Nb}_2\text{CT}_x$  MXene NM with a matching band structure are created and used to power self-powered vis–NIR photodiodes (Figure 27). Using  $\text{MAPbI}_3$  has allowed the  $\text{MAPbI}_3/\text{Nb}_2\text{CT}_x$  photodiode to operate in the vis-regime while suppressing the comparatively substantial dark current of the NIR-absorbing  $\text{Nb}_2\text{CT}_x$ . As a result, the manufactured photodiode reacted linearly to white light illumination with a responsivity of 0.25  $\text{A W}^{-1}$  and a photoresponse time of <4.5  $\mu\text{s}$ . Furthermore, when irradiated with an NIR laser (1064 nm), our photodiode has a greater on/off ratio ( $\approx 10^3$ ) and faster reaction times (30 ms) than planar  $\text{Nb}_2\text{CT}_x$  NMs only detectors (2 and 20 s, respectively). The space-charge-limited current and capacitance measurements show that the coordinate bonding between the surface groups of the 2D MXene NM and the undercoordinated  $\text{Pb}^{2+}$  ions of the  $\text{MAPbI}_3$  at the passivated  $\text{MAPbI}_3/\text{Nb}_2\text{CT}_x$  interface is responsible for such an efficient and enhanced charge transfer.

Su et al.<sup>[300]</sup> developed a  $\text{Nb}_2\text{O}_5/\text{C}/\text{Nb}_2\text{CT}_x$  hybrid material as a photocatalyst for HER (Figure 28a,b), which exhibits good hydrogen generation activity of 7.81  $\text{mmol h}^{-1} \text{g}^{-1}$  catalyst (Figure 28c). Cui et al.<sup>[301]</sup> produced another example in which  $\text{Bi}_2\text{WO}_6/\text{Nb}_2\text{CT}_x$  (Figure 28d) was used as a photocatalyst for the breakdown of organic contaminants. Rhodamine-B (RhB) and methylene blue (MB) absorbed extremely well in vis–light (Figure 28e–h).  $\text{Nb}_2\text{CT}_x$  also has biomedical uses because to its enzyme/ $\text{H}_2\text{O}_2$ -responsive biodegradability and biocompatibility. Xiang et al.<sup>[302]</sup> for example, developed mesoporous silicon on the surface of  $\text{Nb}_2\text{CT}_x$ , where mesopores function as initiator carriers and 2D MXene NM induces photothermal effects at the near-infrared-II biowindow (NIR-II). The 2D  $\text{Nb}_2\text{CT}_x$  confers

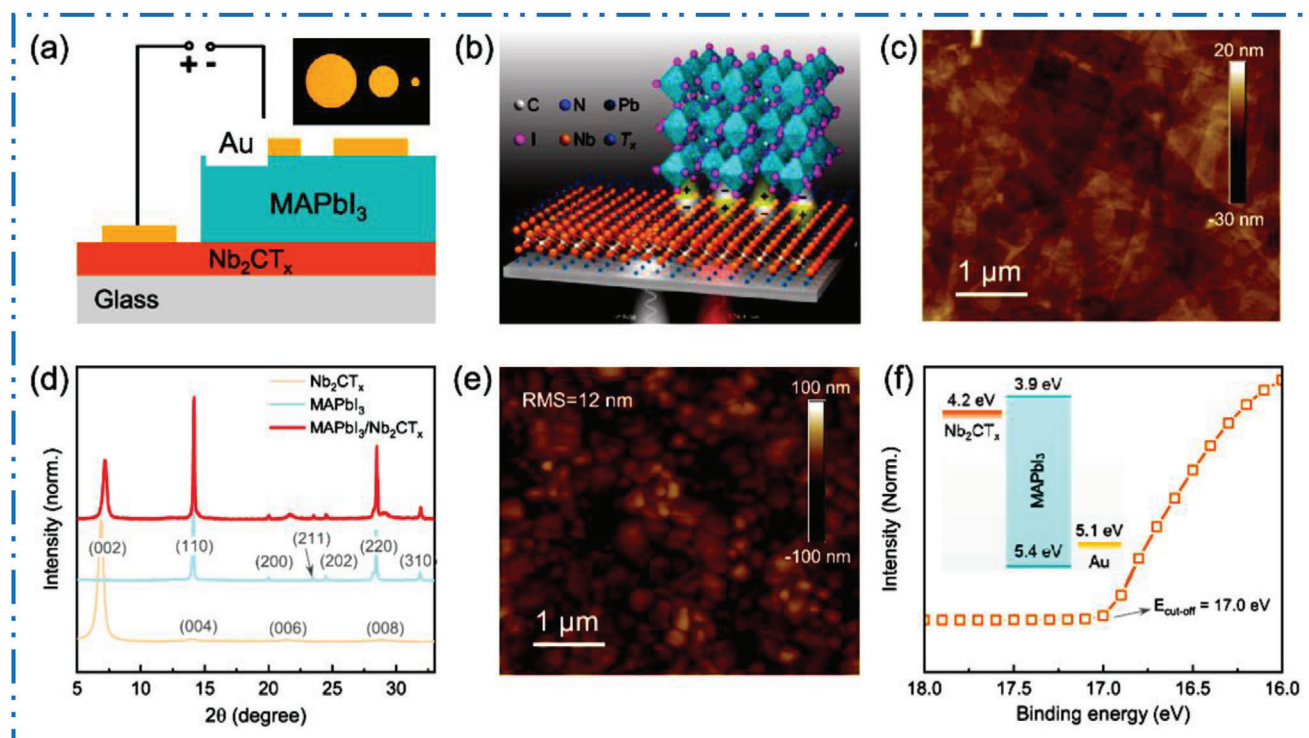


**Figure 27.** a–f) Scheme of heterostructure built of MAPbI<sub>3</sub> perovskite and 2D Nb<sub>2</sub>CT<sub>x</sub> MXene NM and corresponding characterization (AFM and XRD) and photodiodes applications. Reproduced with permission.<sup>[34]</sup> Copyright 2021, American Association for the Advancement of Science (AAAS).

photothermal stability and strong NIR-II absorption in the tissue transparency biowindow (Figure 28i). As a result, initiators are rapidly released and degraded, producing oxygen-independent free radicals. Similarly, Ren et al.<sup>[295]</sup> created the Nb<sub>2</sub>CT<sub>x</sub>-PVP core/shell structure. After radiotherapy, this hybrid substance was certified as hematopoietic recovery medication (Figure 28j).

It is worth noting that the limited uses of 2D Nb-MXene NMs hint that they may encounter the same issues as other hybrid MXene systems. Nb-MXene NMs outperform their pure equivalents in EMI shielding applications. In EMI shielding, for example, Nb<sub>2</sub>V<sub>2-y</sub>CT<sub>x</sub> (15–36 dB depending on the amount of V) outperforms Nb<sub>2</sub>CT<sub>x</sub> (10–15 dB) at 8.2–12.4 GHz. However, for energy storage, the addition of heterocomponents may result in inefficiency. After 20 cycles, the specific capacities of Nb-containing MXenes (e.g., (Nb<sub>0.8</sub>, Ti<sub>0.2</sub>)<sub>4</sub>C<sub>3</sub>T<sub>x</sub> (158 mAh g<sup>-1</sup>) and (Nb<sub>0.8</sub>, Zr<sub>0.2</sub>)<sub>4</sub>C<sub>3</sub>T<sub>x</sub> (132 mAh g<sup>-1</sup>)) are somewhat lower than Nb<sub>4</sub>C<sub>3</sub>T<sub>x</sub> (189 mAh g<sup>-1</sup>).<sup>[303]</sup> After 100 cycles at a current density of 100 mA g<sup>-1</sup>, Nb<sub>3.5</sub>Ta<sub>0.5</sub>C<sub>3</sub>T<sub>x</sub> and Nb<sub>3.9</sub>W<sub>0.1</sub>C<sub>3</sub>T<sub>x</sub> had lower specific capacities of 38 and 35 mAh g<sup>-1</sup>, respectively, than Nb<sub>4</sub>C<sub>3</sub>T<sub>x</sub> (52 mAh g<sup>-1</sup>).<sup>[304]</sup> More efforts should be made to explain the structures and characteristics of 2D Nb-MXene NMs, as well as to discover their benefits and game-changing applications.

## 5.8. Mo-MXene Applications

Mo-MXene has shown to be more effective as catalyst for hydrogen evolution than conventional Ti-MXene.<sup>[305]</sup> As compared to b-Mo<sub>2</sub>C and Cu–ZnO–Al<sub>2</sub>O<sub>3</sub> standard, T<sub>x</sub>-free, Mo-

terminated 2D-Mo<sub>2</sub>C demonstrated astounding catalytic activity and stability.<sup>[306]</sup> The lack of surface terminal groups showed that 2D-Mo<sub>2</sub>C was more active and selective in CO<sub>2</sub> hydrogenation. Several researches have demonstrated tremendous relevance in engineering a development of Mo-based MXene by tweaking its features. One method for dealing with host polymorphism in Mo<sub>2</sub>C MXene crystals is phase engineering.<sup>[307]</sup> Diffusion barrier in elemental precursors of Mo and C may be adjusted by varying the thickness of copper foil used as a catalyst, which also allows for fine control of the development rate of the Mo<sub>2</sub>C crystal. A preferential HER electrocatalytic reactivity for Bernal (AB) stacking as opposed to traditional AA-stacked crystals may be achieved in Mo-MXene by controlling the stacking type.<sup>[307]</sup> As in the case of the Fe-<sup>[308]</sup> and Co-substitution in Mo<sub>2</sub>CT<sub>x</sub>,<sup>[309]</sup> metal substitution may be housed inside the configuration of MXene NMs, which can also boost a electrocatalytic activity. The Mo-based MXene has also been used in growth of new NMs, such as CoP/Mo<sub>2</sub>CT<sub>x</sub> catalysts for energy conversion and water splitting,<sup>[310]</sup> Mo-based MXene NMs in doped CNTs as HER electrocatalysts,<sup>[310]</sup> and Mo<sub>2</sub>CT<sub>x</sub> for humidity monitoring<sup>[311]</sup> (Table 1). Among the MXenes, Mo<sub>2</sub>CT<sub>x</sub> performed the best in the visible spectral range responding at 9 A W<sup>-1</sup> and detecting at 5 × 10<sup>11</sup> Jones, respectively. It was discovered that the surface plasmon-assisted hot electrons in the Mo<sub>2</sub>CT<sub>x</sub> film play a significant role in the photocurrent. Transverse surface plasmon energy of Mo<sub>2</sub>CT<sub>x</sub> coincides with wavelength region of 400–650 nm, where a significant photocurrent was discovered. Under incident light of 660 nm and a bias of 1 V, the highest I<sub>on</sub>/I<sub>off</sub> ratio of 200 was discovered. The Mo<sub>2</sub>CT<sub>x</sub> thin-film photodetector has



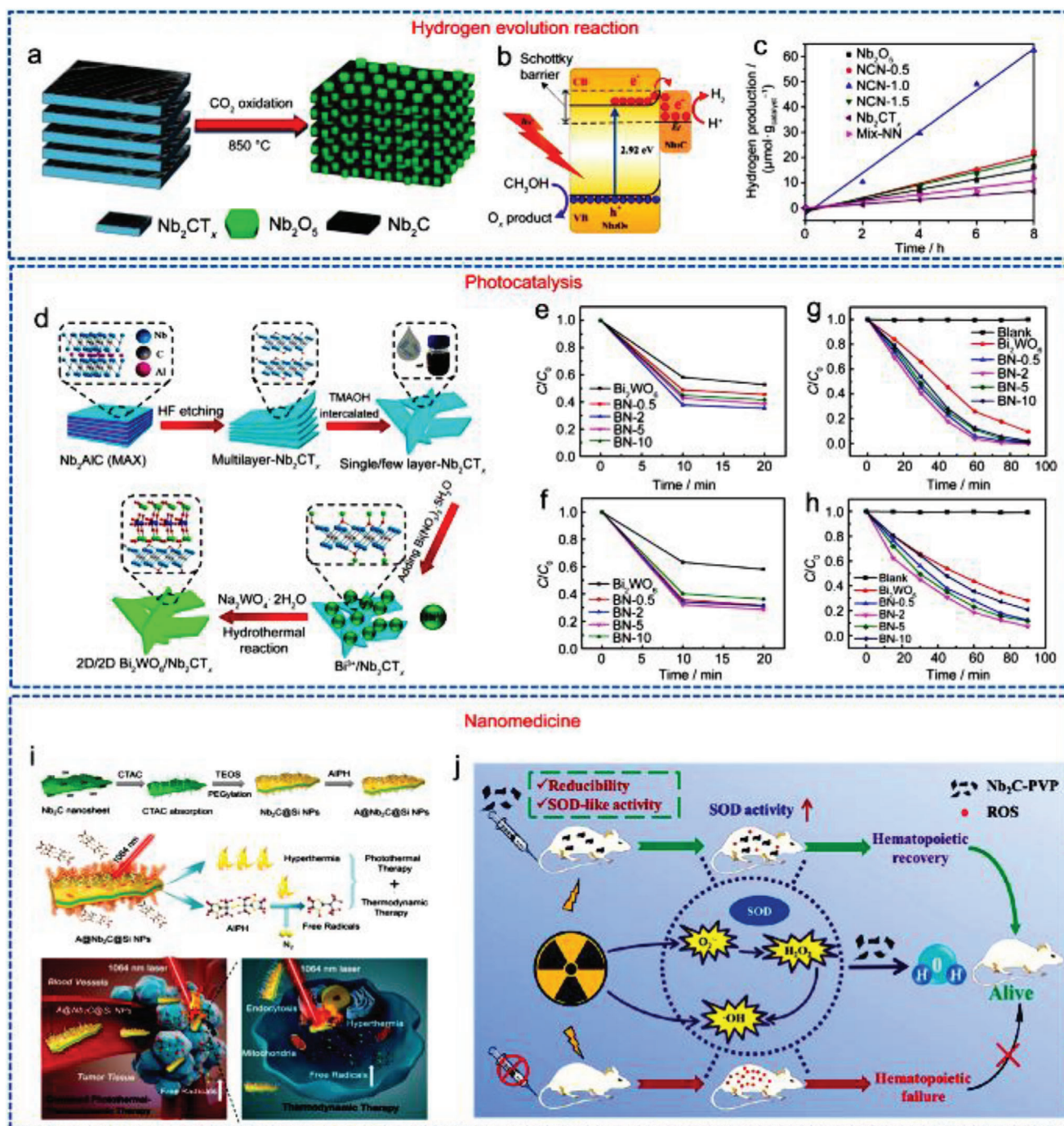


**Figure 28.** a,b) Scheme shows synthesis of  $\text{Nb}_2\text{O}_5/\text{C}/\text{Nb}_2\text{CT}_x$  composite, and its photocatalytic method, and c)  $\text{H}_2$  creation activity, d) scheme shows NSs synthesis, e,f) absorption of RhB and MB in existence of  $\text{Bi}_2\text{WO}_6$ , and g,h) photodegradation of RhB and MB in the presence of  $\text{Bi}_2\text{WO}_6$ . i) Scheme shows synthesis of  $\text{AIPH}@\text{Nb}_2\text{CT}_x@\text{mesoporous (m) SiO}_2$  NPs, and j) hematopoietic recovery after radiation by free radical scavenging. Reproduced with permission.<sup>[203]</sup> Copyright 2020, Springer.

outstanding stability under continuous illumination and in addition repetitive mechanical stress to good photodetection capability (Figure 29).

By using EELS mapping, the precise surface plasmon energies and distribution of  $\text{Mo}_2\text{CT}_x$  were investigated and seen. At 0.30, 0.39, 2.45, and 3.42 eV, four unique peaks were found, and they

are categorized as longitudinal dipole, longitudinal quadrupole, transversal modes, and interband transition, correspondingly. It should be noted that only MXenes have such multipolar surface plasmon modes been identified in 2D NMs. From the instance of  $\text{Ti}_3\text{C}_2\text{T}_x$ , it is known that population of surface termination groups, which closely correlates with the free electron density of

**Table 1.** Non-Ti MXene NMs, with production, key findings, and applications.

M-MXene	Preparation	Key findings	Applications	Refs.
Sc <sub>2</sub> CO <sub>x</sub>	MS-based deposition	Direct production, and no use of etchant and MAX precursors Sensitive to O <sub>2</sub>	Light absorption spectrum and photoluminescence	[139]
ScC <sub>x</sub> OH	Etching (TMAOH) of ScAl <sub>3</sub> C <sub>3</sub>	HF-free technique Traces of Al(OH) 4-surface groups and intercalated TMA <sup>+</sup> ions detected	Direct B.G semiconductor	[138]
V <sub>2</sub> CT <sub>x</sub>	HF-etching of V <sub>2</sub> AlC MAX	High contents of O and OH terminations than F, causes high gas adsorption ability	Gas sensors	[272]
V <sub>2</sub> CT <sub>x</sub>	HF-based etching of V <sub>2</sub> AlC	Contains MAX precursor residue, functionalized layers, and stacked layers limiting the capacity	Positive electrode for NIBs	[319]
V <sub>2</sub> O <sub>x</sub> @V <sub>2</sub> CT <sub>x</sub>	(NaF + HCl)-based etching of V <sub>2</sub> AlC MAX precursor	Formation of V <sub>2</sub> O <sub>x</sub> at high heat treatment based etching technique and electrochemical active process Impurity/formation of by-product Na <sub>5</sub> Al <sub>3</sub> F <sub>14</sub>	ZIBs	[276]
V <sub>2</sub> N	HF-based etching of V <sub>2</sub> AlN MAX precursor	V <sub>2</sub> N can generate abundant reactive O <sub>2</sub> species that can eradicate bacteria (in vitro) and promote the healing of subcutaneous abscesses with negligible toxicity (in vivo)	Photothermal-enhanced anti-infective therapy	[320]
V <sub>2</sub> CT <sub>x</sub>	HF-based etching of V <sub>2</sub> AlC	In situ generation of VO <sub>x</sub> through electrochemical oxidation of V during the initial charging, transforming V valence from V <sup>2+</sup> /V <sup>3+</sup> to V <sup>4+</sup> /V <sup>5+</sup> , all while maintaining inner V–C–V layer residual V <sub>2</sub> AlC are still formed	ZIBs	[321]
a-VO <sub>x</sub> /V <sub>2</sub> C	HF-based etching of V <sub>2</sub> AlC	Anodic oxidation of MLV <sub>2</sub> CT <sub>x</sub> reversible V–O vibration and valence evolution (V <sup>4+</sup> /V <sup>5+</sup> ) in disordered framework	Cathode for NIBs	[322]
Cr <sub>2</sub> CT <sub>x</sub>	Chemical etching (FeCl <sub>3</sub> and tartaric acid) of Cr <sub>2</sub> AlC	Prevented the formation of insoluble alumina existence of Cr <sub>7</sub> C <sub>3</sub> as phase impurity	Sensor for hydrazine detection	[158]
Cr <sub>2</sub> C	Etching (LiF/NaF + HCl) of Cr <sub>2</sub> AlC	Formation of residual salts Incomplete removal of Al	Evaluation of magnetic properties	[323]
Y <sub>2</sub> CF <sub>2</sub>	Solid-state reaction of Y <sub>2</sub> C, YC, and YF <sub>3</sub>	Direct synthesis, and presence of YF <sub>3</sub> and YOF impurity phases not very stable during photoreaction undergoing oxidative degradation (formation of fluorocarbon and carbonate species)	Vis–light induced photocatalytic activity	[173]
Y <sub>2</sub> CF <sub>2</sub>	Solid state reaction of YF <sub>3</sub> , Y-metal, and graphite	Direct synthesis, and controlled F-termination high purity of Y <sub>2</sub> CF <sub>2</sub> easy oxidation because of air exposure	Evaluation of electronic structure and oxidations sensitivity	[171]
YC <sub>x</sub> Td etching (LiF + HCl) of YAl <sub>3</sub> C <sub>3</sub>	HF-based etching of YAl <sub>3</sub> C <sub>3</sub> , Y <sub>2</sub> O <sub>3</sub> Nonuniform sheets	Y <sub>2</sub> O <sub>3</sub> impurity	LIBs as well as SCs electrode	[172]
Zr <sub>3</sub> C <sub>2</sub> T <sub>z</sub>	HF-based etching of Zr <sub>3</sub> Al <sub>3</sub> C <sub>5</sub>	Traces of rock-salt-like cubic ZrC impurities Zr <sub>3</sub> C <sub>2</sub> shows superior thermal stability than Ti-based MXene	Evaluation of structural, mechanical, and electronic properties	[177]
ZrC	MS-deposition	Direct production, and controlled film quality	Optoelectronic material for ultrafast mode-locked fiber lasers	[324]
Nb <sub>2</sub> C	HF-based etching of Nb <sub>2</sub> AlC	Al layer by selective etching	Evaluation of ultrafast relaxation dynamics and nonlinear response	[292]
Nb <sub>2</sub> C	HF-based etching of Nb <sub>2</sub> AlC	Removal of Al layer by selective etching	Electrodes for LIBs	[271]
Nb <sub>4</sub> C <sub>3</sub> T <sub>x</sub>	HF-based etching of Nb <sub>4</sub> AlC	High breakdown current density of 1.1 × 10 <sup>8</sup> A cm <sup>−2</sup>	Evaluation of electronic properties and high breakdown current density response	[325]

(Continued)



**Table 1.** (Continued)

M-MXene	Preparation	Key findings	Applications	Refs.
Nb <sub>2</sub> CT <sub>x</sub>	HF-based etching of Nb <sub>2</sub> AlC	Work functions are modulated by replacing the surface terminated —F groups with —NH <sub>2</sub> group	Electron transport layer and perovskite additive for perovskite solar cells	[291]
Nb <sub>2</sub> CT <sub>x</sub>	HF-based etching of Nb <sub>2</sub> AlC	Occurrence of unreacted Nb <sub>2</sub> AlC and residual Al-containing secondary phases	Evaluation of electronic and mechanical properties, and surface chemistry	[326]
Mo <sub>2</sub> CT <sub>x</sub>	HF-based etching of Mo <sub>2</sub> Ga <sub>2</sub> C	Relative stability against oxidation compared to Ti <sub>3</sub> C <sub>2</sub> T <sub>x</sub> , Nb <sub>2</sub> CT <sub>x</sub> , T <sub>2</sub> CT <sub>x</sub> , and V <sub>2</sub> CT <sub>x</sub> possible oxidized forms of Mo—O moieties in product	Plasmonic photodetection	[312]
Mo <sub>2</sub> C	UV-induced etching (H <sub>3</sub> PO <sub>4</sub> ) of Mo <sub>2</sub> Ga <sub>2</sub> C	HF-free production of high-quality F-free MXene NMs	LIBs and NIBs	[327]
Mo <sub>2</sub> CT <sub>x</sub>	HF-based etching of Mo <sub>2</sub> Ga <sub>2</sub> C	Optimization of Ga removal (HF at 140 °C after 96 h)	Catalytic activity in the water-gas shift reaction	[328]
Mo <sub>2</sub> CT <sub>x</sub>	HF-based etching of Mo <sub>2</sub> Ga <sub>2</sub> C	Stability in acid Mo <sub>2</sub> CT <sub>x</sub> was found to shows high HER activity than Ti <sub>2</sub> CT <sub>x</sub>	HER	[305]
Mo <sub>2</sub> N	Ammoniation of Mo <sub>2</sub> CT <sub>x</sub>	Retained MXene structure upon transformation conductivity values of Mo <sub>2</sub> N are three magnitudes larger than Mo <sub>2</sub> CT <sub>x</sub>	Evaluation of thermoelectric properties	[329]
Mo <sub>2</sub> C	Epitaxial synthesis through chemical conversion of MoS <sub>2</sub>	Excellent sheet resistance (123.6 Ω sq <sup>-1</sup> ) and carrier concentration (5.84 × 10 <sup>13</sup> cm <sup>-2</sup> )	Evaluation of electronic properties	[202]
Hf <sub>3</sub> C <sub>2</sub> T <sub>2</sub>	HF-based etching of Hf <sub>3</sub> [Al(Si)] <sub>4</sub> C <sub>6</sub>	Trace of unreacted Hf <sub>3</sub> [Al(Si)] <sub>4</sub> C <sub>6</sub> , and small amount of cubic HfC impurities more than 65% conversion from MAX to MXene NMs	LIBs and NIBs	[174]
Ta <sub>4</sub> C <sub>3</sub>	HF-based etching of Ta <sub>4</sub> AlC <sub>3</sub>	Surface modification improved biocompatibility and physiological stability with no noticeable toxicity	Dual-mode photoacoustic/CT-scan and in vivo photothermal ablation of tumors for biomedical uses	[330]
Ta <sub>4</sub> C <sub>3</sub>	HF-based etching of Ta <sub>4</sub> AlC <sub>3</sub>	Third-order nonlinear optical characteristics	Mode-locked fiber lasers	[316]
Ta <sub>4</sub> C <sub>3</sub> T <sub>x</sub>	HCl-based etching of Ta <sub>4</sub> AlC <sub>3</sub> , then with KOH solution	F-free etching method 84% removal of elemental Al promoted higher degree of OH and O groups functionalization	Biocompatible material for SCs electrodes	[317]
W <sub>1.33</sub> CT <sub>x</sub>	Etching (HF) of (W <sub>2/3</sub> Y <sub>1/3</sub> ) <sub>2</sub> AlC or (W <sub>2/3</sub> Sc <sub>1/3</sub> ) <sub>2</sub> AlC	Trace of MAX phase	Electrode for SCs	[216]
W <sub>1.33</sub> C	Etching (HCl + LiF) of (W <sub>2/3</sub> R <sub>1/3</sub> ) <sub>2</sub> AlC (R = Gd, Tb, Dy, Ho, Er, Tm, and Lu)	Antiferromagnetic paramagnetic for R = Lu-derived W-MXene complicated magnetic moment alignments for R = Tb, Dy, and Ho derived W-MXene	Evaluation of electrochemical properties	[217]
W <sub>1.33</sub> CT <sub>x</sub>	Etching (HF) of (W <sub>2/3</sub> Sc <sub>1/3</sub> ) <sub>2</sub> AlC Etching (LiF + HCl) of (W <sub>2/3</sub> Sc <sub>1/3</sub> ) <sub>2</sub> AlC Etching (HF) of (W <sub>2/3</sub> Y <sub>1/3</sub> ) <sub>2</sub> AlC	Ordered metal divacancies Pure phase Ordered metal divacancies Pure phase Ordered metal divacancies Impurity phases of original MAX phase, YAl <sub>3</sub> C <sub>3</sub> , W, and Y <sub>2</sub> O <sub>3</sub>	HER	[97]
W <sub>1.33</sub> C	Etching (LiF + HCl) of (W <sub>2/3</sub> Y <sub>1/3</sub> ) <sub>2</sub> AlC	Ordered divacancies and desirable biocompatibility/biodegradability	Tumor retention and theranostic functionalities for biomedical uses	[331]

2D MXene NMs, may be controlled to further tailor the longitudinal and transversal surface plasmon energies of MXenes.<sup>[242]</sup> The shape of each flake affects longitudinal dipole and quadrupole modes as well. Each monolayer MXene nanoflake keeps its own surface plasmon modes as separate NSs in the ML film due to the weak interlayer interaction of 2D MXene NMs, which enables the effective production of broadband plasmonic photodetection. Li et al.<sup>[55]</sup> created a sodium-ion capacitor (NIC) with an anode made of assembled Mo<sub>2</sub>C Ns (**Figure 30a**). The as-prepared ca-

pacitor had a maximum energy density of 76.1 Wh kg<sup>-1</sup> at a power density of 112 Wh kg<sup>-1</sup> and outperformed other active carbon-based capacitors (**Figure 30b**). Cycling stability at 1 A g<sup>-1</sup> current density further demonstrates the good capacity retention (**Figure 30c**). Mo<sub>2</sub>CT<sub>x</sub> catalytic activity in the water-gas shift process was reported by Sokol et al.<sup>[51]</sup> (**Figure 30d**). The results show that the 2D Mo<sub>2</sub>CT<sub>x</sub> had the highest activity of all investigated catalysts, with the maximal activity attained at roughly 520 °C and a peak CO consumption rate of ≈100 μmol(CO) g(Mo)<sup>-1</sup> s<sup>-1</sup>

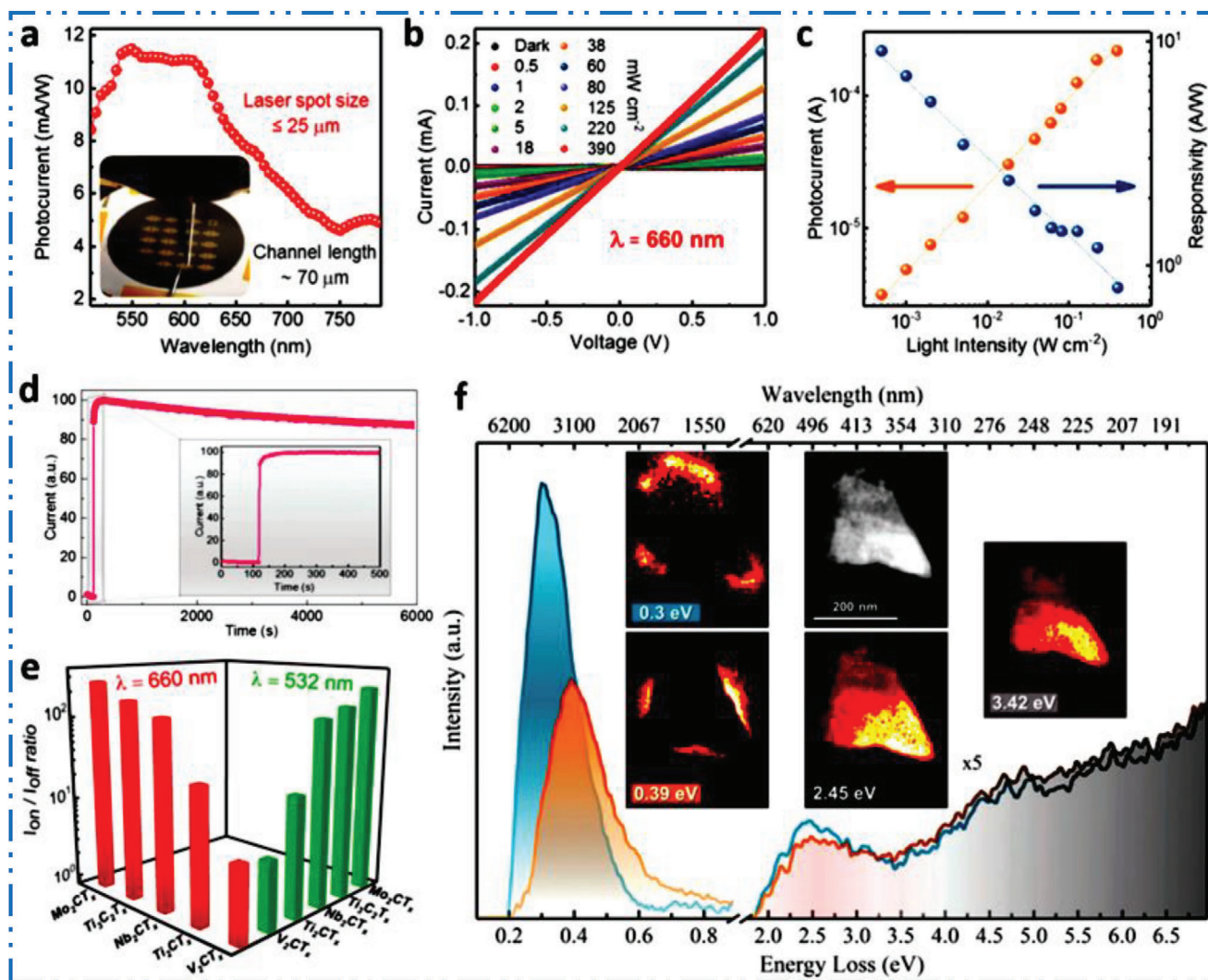


**Figure 29.** Photoreponse based on  $\text{Mo}_2\text{CT}_x$ , a) photocurrent at 0.7 V bias voltage, b) linear  $I$ - $V$  graph under different light intensities (660 nm), c) photocurrent and responsivity as a function of light intensity, d) photostability under continuous illumination, e)  $I_{\text{on}}/I_{\text{off}}$  ratio under excitation wavelengths of 660 and 532 nm, and f) zero-loss peak subtracted EELS spectra of a  $\text{Mo}_2\text{CT}_x$  with a truncated triangular shape. Reproduced with permission.<sup>[312]</sup> Copyright 2019, Wiley.

(Figure 30e). Furthermore, negligible deactivation was seen after 10 h on stream at roughly 500 °C, as illustrated in Figure 30f. Anasori et al.<sup>[49]</sup> coupled  $\text{MoS}_2$  and  $\text{Mo}_2\text{C}$  to create a photodetector with excellent sensitivity and broad spectrum (Figure 30g). This  $\text{Mo}_2\text{C}$ -based hybrid device has good responsiveness at various lighting power densities (Figure 30h). Hadi et al.<sup>[48]</sup> used 2D  $\text{Mo}_2\text{CT}_x$  NM as a theranostic nanoagent in the medical field (Figure 30i). In this setup, high cell viability was attained, confirming  $\text{Mo}_2\text{CT}_x$ 's superior biocompatibility (Figure 30j,k). Established research on Mo-MXene NMs has taken the possibility of switching the precursor from MAX to MAB precursors. This provides a fantastic chance to examine MBenes, which may have unique features that is not present in MXene NMs. In addition, investigations on molybdenum could be constrained by their low abundance. Thus, it is important to look into metal substitutes on Mo-based MXene NMs with competitive characteristics.

## 5.9. Ta-MXene Applications

Ta element (atomic number = 73) is investigated a 2D structure in biological uses<sup>[313]</sup> because Ta provides strong image contrast that might be advantageous for XRD and CT based imaging. Delaminated 2D  $\text{Ta}_4\text{C}_3$  that had been changed with soybean phospholipid (SP) and  $\text{MnO}_x/\text{Ta}_4\text{C}_3$  MXene NSs and modified with SP both demonstrated photoacoustic/CT imaging capacity and bio-functionalities that were suitable for biological uses. Ta-MXene, a 2D structure, may be used as an effective host to create hybrid materials with extended functionalities, for instance,  $\text{Ta}_4\text{C}_3$ -IONPs, which are very effective theranostic agents for breast cancer.<sup>[314]</sup> Outside of biomedical uses,  $\text{Ta}_4\text{C}_3$  can also provide remarkable conductive qualities<sup>[315]</sup> that have been used and investigated in optoelectronics,<sup>[209,316]</sup> electrodes for supercapacitors (SCs),<sup>[317,318]</sup> and catalysts for water splitting.<sup>[318]</sup> Table 1 provides an overview of other Ta-MXene production and uses.



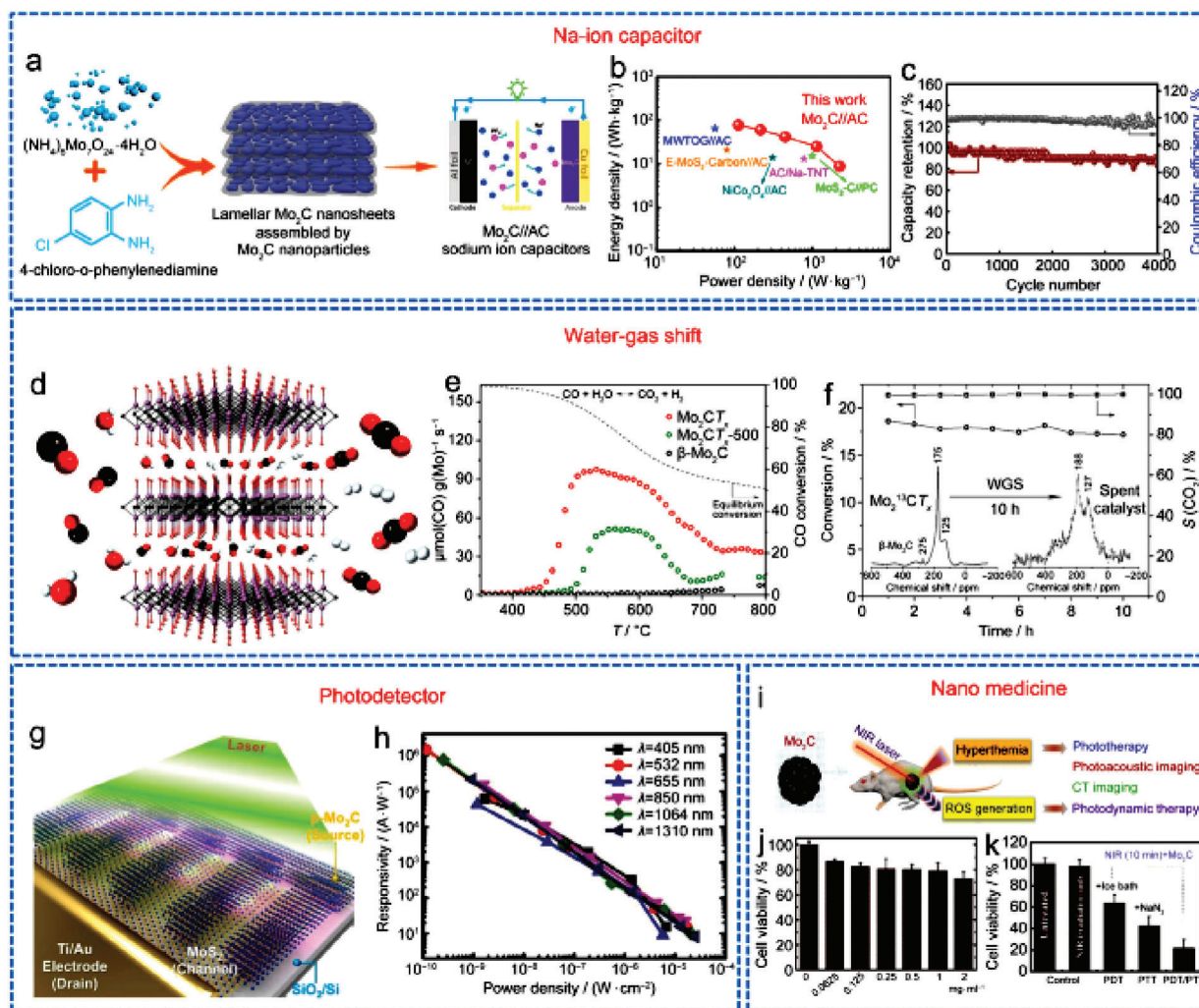


**Figure 30.** a) Scheme of  $\text{Mo}_2\text{CT}_x$  NSs synthesis and with  $\text{Mo}_2\text{CT}_x$  NPs, b) Ragone-plot, c) cycling stability of electrode at  $1\text{ A g}^{-1}$ , d) scheme of water-gas shift (WGS), e) WGS catalytic activity test, f) WGS stability test, g) scheme figure of photodetector device, h) responsivity of  $\text{MoS}_2/\text{multiple periods (mp)}$ - $\text{Mo}_2\text{C}$  hybrid device, i) scheme shows  $\text{Mo}_2\text{C}$ -mediated cancer theranostic, j) cell viability, and k) cell viability after PTT, PDT, and synergistic treatment of PDT/PTT. Reproduced with permission.<sup>[203]</sup> Copyright 2020, Springer.

## 5.10. W-MXene Applications

For use in  $\text{NH}_3$  gas sensing applications, the surface  $\text{T}_x$  of  $\text{W}_2\text{C}$  with O and F are seen and studied.<sup>[218]</sup> Strong physisorption and robust interactions in the substrate and  $\text{NH}_3$  were seen in both systems, giving O/F terminated W-based MXene NMs excellent sensor capabilities at low  $\text{NH}_3$  concentration within a broad temperature window. In order to comprehend the variety of potentials of W-based and other MXene NMs that have not yet been identified, such first-principles research is highly appreciated. Table 1 shows catalogue of the non-Ti 2D MXene NMs, with production, key findings, and various novel devices uses.

## 5.11. Double Transition Metal MXenes Applications

In spite of the fact that novel MAX and MXenes developed continually over the past few years, and computational approaches

were extremely helpful in forecasting their characteristics and performance.<sup>[332]</sup> The chemical formulas  $\text{M}_2\text{MC}_2\text{T}_x$  and  $\text{M}_2'\text{M}_2''\text{C}_3\text{T}_x$  have been shown to have the most stable terminations<sup>[333]</sup> ( $\text{M}'$  and  $\text{M}''$  are two distinct metals;  $\text{M}' = \text{Cr, V, Ti, or Nb}$ ;  $\text{M}'' = \text{Ta, Nb, Ti, or V}$ ; and  $\text{T} = \text{O and/or OH}$ ).  $\text{Mo}_2\text{TiC}_2$  and  $\text{Mo}_2\text{Ti}_2\text{C}_3$  were anticipated to have the lowest formation energies, and they have previously been created experimentally.<sup>[334]</sup>  $\text{Ti}_2\text{ZrC}_2\text{O}_2$ ,  $\text{TiZrCO}_2$ , and  $\text{TiZr}_2\text{C}_2\text{O}_2$  were projected to have theoretical capacities of 586, 441, and 374  $\text{mAh g}^{-1}$ , correspondingly. These materials were shown to outperform their monotitanium- and mono-Zr carbides.<sup>[335]</sup> Theoretically,  $\text{SL Ti}_2\text{Mn}_2\text{C}_2\text{T}_x$ ,  $\text{Hf}_2\text{-Mn}_2\text{C}_2\text{T}_x$ , and  $\text{Hf}_2\text{VC}_2\text{T}_x$  ( $\text{T} = \text{F, OH, O, etc.}$ ) are anticipated to have metallic and semiconducting characteristics.<sup>[260]</sup> Understanding these characteristics it will eventually enable one to comprehend how well they operate in various contexts, including HER,<sup>[333]</sup> Al-,<sup>[336]</sup> and Na-ion batteries.<sup>[337]</sup> The experimentally formed double TM MXene NMs and their uses are listed in Table 2. Mo–O motifs were used to anchor the ordered double transition-metal  $\text{Mo}_2\text{TiC}_2\text{T}_x$

**Table 2.** Experimental synthesis of double transitional metal MXenes NM and their applications.

Origin of MAX precursor	Etchant	Double metal MXene	Applications	Refs.
TiVAIC	LiF, HCl	TiVCT <sub>x</sub>	Dual-functional antibacterial capability	[348]
Ti <sub>x</sub> Ta <sub>4-x</sub> AlC <sub>3</sub>	HF	Ti <sub>x</sub> Ta <sub>4-x</sub> C <sub>3</sub>	LIBs anodes	[349]
TiNbAlC	HF	TiNbCT <sub>x</sub>	LIBs anode	[350]
Mo <sub>4</sub> VAIC <sub>4</sub>	HF	Mo <sub>4</sub> VC <sub>4</sub>	Electrical/optical properties Evaluation	[108]
Mo <sub>2</sub> TiAlC <sub>2</sub>	HF	Mo <sub>2</sub> TiC <sub>3</sub> T <sub>x</sub>	Evaluation of semiconductor properties	[351]
Mo <sub>2</sub> Ti <sub>2</sub> AlC <sub>3</sub>		Mo <sub>2</sub> Ti <sub>2</sub> C <sub>3</sub> T <sub>x</sub>		
Mo <sub>2</sub> TiAlC <sub>2</sub>	HF	Mo <sub>2</sub> TiC <sub>2</sub> T <sub>x</sub>	Flexible memristors	[352]

MXene, which was then transformed into Mo–S bonds using the in situ sulfidation technique.<sup>[338]</sup> For anodes in LIBs, the unique heterostructures of FL MoS<sub>2</sub> on Mo<sub>2</sub>TiC<sub>2</sub>T<sub>x</sub> led to high specific capacities and Columbic efficiencies, high rate capability, and outstanding cycle stability. This in situ conversion method is highly intriguing since it uses the primary metals to produce a secondary material with only a small amount of precursor input. In the same way, serving as an inspiration for subsequent research, metal oxides derived from MOFs,<sup>[339]</sup> multiple metals incorporated in MOF structures<sup>[340,341]</sup> or multiple metal-based oxides,<sup>[342–344]</sup> as well as doping methods<sup>[345]</sup> are all examples of synthesis methods that can use a base material to include additional advantageous compounds. Nevertheless, using MXene NMs as the basis NM still need a better theoretical and experimental comprehension of their characteristics. The inherent magnetism and half-metallic properties of the 2D MXene NMs offer significant promise for spintronic and magnetic devices, such as attaining complete spin-filtering in vdWs magnetic tunnel junctions (MTJs). Cui et al.<sup>[346]</sup> investigated theoretically the spin-dependent transport properties of 2D ScCr<sub>2</sub>C<sub>2</sub>F<sub>2</sub> NMs-based vdWs MTJs, where ScCr<sub>2</sub>C<sub>2</sub>F<sub>2</sub> acts as the spin-filter tunnel barriers, 1T-MoS<sub>2</sub> acts as the electrode, and 2H-MoS<sub>2</sub> acts as the tunnel barrier. They discovered that spin-up electrons in the parallel configuration stage play an important role in transmission behavior. All of built MTJs could maintain significant tunnel magnetoresistance (TMR) ratios greater than  $9 \times 10^5\%$ . Especially, the maximum giant TMR ratio of  $6.95 \times 10^6\%$  can be found in vdWs MTJ with trilayer 2H-MoS<sub>2</sub> as the tunnel barrier. These results indicate that the potential for spintronic applications of vdWs MTJs based on 2D ScCr<sub>2</sub>C<sub>2</sub>F<sub>2</sub>.

### 5.12. Non-IIIB to VIB Metal Group Applications

First-principles calculations revealed that the Lu<sub>2</sub>C(OH)<sub>2</sub> arrangement had an ultralow work function and showed a straight B.G (1.4 eV). In the meanwhile, 4.6 eV was determined as the work function of F-based MXene NMs, like, Lu<sub>2</sub>CF<sub>2</sub>. This expected low work function for lanthanide-MXene NMs has significant potential for use in electrical devices. According to first-principles simulations study of electronic and magnetic characteristics of Mn<sub>2</sub>CT<sub>2</sub> MXene NMs (T = H, Cl, OH, O, and F),<sup>[347]</sup> Mn<sub>2</sub>CF<sub>2</sub> is a half-metal with a large half-metallic gap and RT ferromagnetism. Evolution of MXene NMs migrates to a completely new adventure with the bordering of MXene NMs beyond the IIIB to VIB family. Theoretical research on Mn-MAX precur-

sors and Mn-based MXene NMs, which are members of the VIIIB family, may provide attractive and exciting options for studying well-known battery NMs like nickel, cobalt, etc. Thus, theoretical analyses are highly required to ascertain the likelihood of producing these novel MXene NMs using experimental means. Table 2 shows mostly studied experimental synthesis of double TMs based 2D MXene NMs and their novel technological advanced applications.

## 6. Stability and Advantages of Non-Ti MXenes and Their Challenges

The 2D MXene NMs' stability at high-temperature is determined through their composition and surrounding environments. As a result, many investigations have observed varying high temperature behavior. In the existence of O<sub>2</sub> and H<sub>2</sub>O, MXene NMs based nanoflakes do not remain stable forever.<sup>[353]</sup> In O<sub>2</sub> free degassed water or dry air, however, they are relatively stable. In addition, light can hasten the oxidation of the colloidal MXene solution. Thus, it is advised that MXene colloids are stored in the O<sub>2</sub> free, dark environment. Generally, MXene nanoflakes oxidation begins at the edges, resultant in creation of metal oxide nano-size crystals (e.g., TiO<sub>2</sub>) that decorate the nanoflakes edges, with subsequently spreads throughout the whole surface during nucleation and growth.<sup>[354]</sup> Oxidation resistance of 2D MXene NMs is determined by the production process; higher-quality single nanoflakes MXene have superior oxidation resistance.<sup>[355]</sup> MXenes' high-temperature stability science is continually evolving. Nonstoichiometric TMCs phase diagrams may aid in predicting 2D MXene NMs phase stability.<sup>[247]</sup> The XRD or Raman analysis required to prove if any novel phases have developed, despite the characterization results seem appealing. The Zr<sub>3</sub>C<sub>2</sub>T<sub>x</sub> has been proven for good thermal stability and preserve its 2D nature at about 1000 °C in vacuum. The superior thermal stability of the fact that Zr<sub>3</sub>C<sub>2</sub> has a more energetically advantageous structure than bulk ZrC. Zr<sub>3</sub>C<sub>2</sub>T<sub>x</sub> may be advantageous for high temperature uses because of its increased stability. So far, attempts to synthesize Cr<sub>2</sub>C from Cr<sub>2</sub>AlC have failed.<sup>[356]</sup> One probable explanation is that chromium carbide is less stable than other carbides due to its lower cohesive energy.<sup>[357]</sup> Cr<sub>2</sub>C may develop in aqueous solutions during etching and swiftly convert to other phases, such as chromium oxides. For further details about stability and solution can read our recently published article.<sup>[358]</sup>

Titanium was the focus of MXene NMs research on development since it was first time studied. The outstanding selection



of TM candidates within the group-(III–VI)B family member has demonstrated the viability of replacing Ti in MXene NMs, as addressed above in this paper. In the biomedical area, where safety and toxicity are issues, MXene, rely on Ta, V, and Nb, shown biocompatibility and low-toxicity, which is much appreciated. The electrical characteristics of Nb-, Mo-, Y-, and V-MXene were excellent and suitable for electrocatalytic and energy storage devices. Using untapped non-Ti 2D MXene NMs in particular showed improved characteristics to the conventional Ti-MXene NMs. While  $\text{Ti}_2\text{C}$  showed less theoretical capacity than  $\text{V}_2\text{C}$  and  $\text{Nb}_2\text{C}$ ,  $\text{Mo}_2\text{C}$  showed significantly more HER activity. The study of non-Ti MXene in semiconductors (Sc, Y, and Zr), lasers (Nb, Ta, and Zr), and sensors (V, Nb, and Cr) has also shown encouraging results. Ti-MXene make almost 70%, that has more studied and hence has a strong advantage over other non-Ti MXenes materials because, Mo, Nb, V, Cr, W, Zr, Hf, Ta, Sc, Y, and others make up the remaining 30%. Non-Ti MXene studies are primarily restricted to theoretical research, despite the fact that they are attracting a lot of interest and attention. As a result, there is a significant research void for non-Ti MXene uses. In fact, several non-Ti MXene NMs have not yet been experimentally investigated in SCs, batteries, or catalysis.

Despite this restriction, there is rising interest in studying non-Ti MXenes using theoretical and computational approaches. The formation energies of several MXene types<sup>[33]</sup> provided the best indication of whether or not these MXenes could be synthesized experimentally. It was projected that the  $\text{M}_2\text{N}$  adsorption energies ( $\text{M} = \text{Ti, Zr, Hf, V, Nb, Ta, Cr, Mo, and W}$ ) would function as effective  $\text{CO}_2$  conversion catalysts.<sup>[359]</sup> Because no practical investigations have comprehensively enumerated the benefits of non-Ti or M-based MXene NMs to yet, several papers demonstrated their theoretical qualities that can be associated to their future uses. The various applications that may be influenced by these theoretical qualities can then be connected. In comparison to other  $\text{M}_2\text{C}$ -type MXenes, such as Cr, Nb, Mo, Hf, Ta, and W,  $\text{Sc}_2\text{C}$ ,  $\text{Ti}_2\text{C}$ ,  $\text{V}_2\text{C}$ , and  $\text{Zr}_2\text{C}$  MXene NMs are projected to exhibit rapid charge/discharge rates due to their lower Li diffusion energy barriers.<sup>[360]</sup> The  $\text{Sc}_2\text{CO}_2$ ,  $\text{Ti}_2\text{CO}_2$ ,  $\text{Zr}_2\text{CO}_2$ ,  $\text{Hf}_2\text{CO}_2$ , and  $\text{Mn}_2\text{CO}_2$  turned out to be semiconducting for the catalytic activity of the 2D MXene NMs with  $\text{M}_{n+1}\text{CnO}_2$  ( $n = 1, 2$ ;  $\text{M} = \text{Sc, V, Cr, Mn, Zr, Nb, Mo, Hf, Ta, and W}$ ) configurations. The disadvantages of M-MXene over other alternatives are also known, such as  $\text{Sc}_2\text{C}(\text{OH})_2$  and  $\text{Zr}_2\text{C}(\text{OH})_2$ 's inability to remove Pb in comparison to other  $\text{M}_2\text{X}(\text{OH})_2$  systems ( $\text{M} = \text{V, Cr, Nb, Mo, Hf, Ta, and X} = \text{C or N}$ ).<sup>[361]</sup> Another illustration shows that when compared to  $\text{Ti}_2\text{CO}_2$ ,  $\text{V}_2\text{CO}_4$ ,  $\text{Nb}_2\text{CO}_2$ , and  $\text{Mo}_2\text{CO}_2$ ,  $\text{Sc}_2\text{CO}_2$ ,  $\text{Y}_2\text{CO}_2$ , and  $\text{Cr}_2\text{CO}_2$  did not attain greatest recommended formation energy to produce freestanding 2D MXenes NSs.<sup>[362]</sup> In practice, this might make it challenging and difficult to experimentally synthesize Sc-, Y-, and Cr-based  $\text{M}_2\text{CO}_2$  NMs.<sup>[363]</sup> As compared to other  $\text{M}_2\text{N}$ -type MXene ( $\text{M} = \text{Zr, Hf, V, Nb, Ta, Cr, Mo, and W}$ ),  $\text{Cr}_2\text{N}$ ,  $\text{Mo}_2\text{N}$ , and  $\text{W}_2\text{N}$  are less appropriate materials for possible candidates for  $\text{CO}_2$  reduction.<sup>[359]</sup> The B.Gs of  $\text{Sc}_2\text{C}(\text{OH})_2$  (0.74 eV) and  $\text{Mo}_2\text{CF}_2$  (0.84 eV) are inadequate compared to  $\text{M}_2\text{C}$ -type MXenes like  $\text{Zr}_2\text{CO}_2$ ,  $\text{Hf}_2\text{CO}_2$ ,  $\text{Sc}_2\text{CF}_2$ ,  $\text{Sc}_2\text{CO}_2$ <sup>[283]</sup> to give sufficient energy for water splitting. Even if the majority of these texts have looked into computational analysis of M-type MXene NMs, there is still a strong necessitating supporting theories with experimental data. Unfortunately, 2D MXene

NMs cannot be prepared in a way that allows for a direct comparison of their attributes to those of another MXene. Therefore, theoretical approaches offer a good grasp of the characteristics of various M-MXene to decide whether they are practical in particular applications.

## 7. Summary

MXene is a family of 2D materials composed of TMCs, TMNs, or TM carbonitrides. While Ti-based 2D MXene NMs have been extensively studied, but there are also many non-Ti MXenes that have been discovered and investigated, such as vanadium carbide, niobium-based, molybdenum-titanium carbide, tungsten carbide, etc., MXenes. Many Ti-based MXenes rely on the extraction of titanium, which can be costly and environmentally damaging. By contrast, non-Ti MXenes may be synthesized from more abundant and environmental friendly sources, making them an attractive alternative. These non-Ti MXene NMs exhibit unique properties, such as high electrical conductivity, mechanical strength, thermal stability, and good electrochemical and thermal properties, making them promising candidates for a variety of applications such as energy storage, catalysis, thermal management, and wear-resistant coatings. Further research is needed to fully explore the potential of non-Ti MXenes in various fields. The  $\text{M}_2\text{C}$ -type ( $\text{M} = \text{Sc, V, Zr, Nb, Mo, Hf, Ta}$ ) and  $\text{M}_2\text{N}$ -type ( $\text{M} = \text{Zr, Hf}$ ) with F, O, and OH MXene systems have strong electrical conductivity but weak thermoelectricity.<sup>[231]</sup> Regarding to various technological novel applications of non-Ti MXenes,  $\text{Sc}_2\text{CF}_2$ ,  $\text{Zr}_2\text{CF}_2$ , and  $\text{Mo}_2\text{CF}_2$  are the best acceptable cathode material for asymmetric supercapacitors in aqueous and ionic/organic systems.<sup>[364]</sup> Among 2D vanadium carbide MXenes ( $\text{V}_2\text{C}$ ,  $\text{V}_2\text{CT}_x$ , etc.) the  $\text{V}_2\text{CF}_2$  is the most recommended anode material for asymmetric supercapacitors.<sup>[364]</sup> Theoretically,  $\text{V}_2\text{NS}_2$  demonstrated a larger Na capacity ( $99.8 \text{ mAh g}^{-1}$ ) than  $\text{Ti}_2\text{NS}_2$  ( $84.77 \text{ mAh g}^{-1}$ ).<sup>[365]</sup>

The  $\text{M}_2\text{N}$ -type ( $\text{M} = \text{Zr, Hf}$ ) with F, O, and OH-MXene NMs, V-, Nb-, and Ta-based 2D MXene NMs exhibit high electrical conductivity but relatively subpar thermoelectricity.<sup>[231]</sup> While Zr-, and Hf-MXene NMs with F, O, and OH functionalized, exhibit average thermoelectricity while the finest thermoelectricity exhibited by Mo- and semiconducting nonmagnetic Cr-based MXenes.<sup>[231]</sup> The Ta-, Nb-, and V-based MXenes exhibit strong electrical conductivity but low thermoelectricity.<sup>[231]</sup>

This shows that 2D  $\text{Mo}_2\text{C}$  MXene NMs are preserving with the presence of vacancies have improved structural stability, electrical conductivity, and Li storage capacity.<sup>[366]</sup> Among various  $\text{M}_2\text{C}$  MXene ( $\text{M} = \text{V, Zr, Hf, Nb, Ta, Mo, W}$ ),  $\text{Mo}_2\text{C}$  and  $\text{W}_2\text{C}$  are among the most promising MXenes for  $\text{CO}_2$  collection and posterior release procedures.<sup>[367]</sup> The  $\text{Cr}_3\text{C}_2$ ,  $\text{Mo}_3\text{C}_2$ ,<sup>[368]</sup> and  $\text{W}_2\text{CO}_2$ <sup>[369]</sup> 2D MXene NMs show that they have the most promising  $\text{CO}_2$  to  $\text{CH}_4$  selective conversion capabilities.

As compared to other MXenes  $\text{Sc}_2\text{CO}_2$ , especially  $\text{Zr}_2\text{CO}_2$ ,  $\text{Hf}_2\text{CO}_2$ , has better hazardous  $\text{SO}_2$  gas detection performance.<sup>[370]</sup> The  $\text{Mo}_2\text{CO}_2$  and  $\text{V}_2\text{CO}_2$  are less effective in adsorbing  $\text{NH}_3$  and NO than  $\text{Nb}_2\text{CO}_2$ .<sup>[371,231]</sup> The HER catalytic activity at high H coverage is shown by  $\text{V}_2\text{CO}_2$ ,  $\text{Cr}_3\text{C}_2\text{O}_2$ ,<sup>[372,373]</sup> while at low H coverage, it is catalyzed by  $\text{Zr}_3\text{C}_2\text{O}_2$ ,  $\text{Nb}_2\text{CO}_2$ ,  $\text{W}_2\text{CO}_2$ , and  $\text{W}_3\text{C}_2\text{O}_2$ .<sup>[373]</sup> The  $\text{Nb}_2\text{NO}_2$  also shows promising HER performance.<sup>[374,231]</sup>

The  $\text{Cr}_2\text{C}(\text{OH})_2$ ,  $\text{Cr}_2\text{NF}_2$ ,  $\text{Cr}_2\text{N}(\text{OH})_2$ , and  $\text{Cr}_2\text{NO}_2$  are ferromagnetic,<sup>[373]</sup> while  $\text{Zr}_2\text{C}$  and  $\text{Ti}_2\text{C}$  exhibit spontaneous magnetism.<sup>[361,362]</sup>

$\text{Y}_2\text{CF}_2$  (0.98 eV) and  $\text{Y}_2\text{CCl}_2$  (0.69 eV) are semiconductors with indirect B.G.s, together with  $\text{Sc}_2\text{CF}_2$  (1.06 eV) and  $\text{Sc}_2\text{CCl}_2$  (1.31 eV).<sup>[281]</sup> The  $\text{Zr}_2\text{CO}_2$  and  $\text{Hf}_2\text{CO}_2$  are potential single photocatalysts with excellent photocatalytic efficiency.<sup>[283]</sup>

The 2D niobium-based MXenes NMs (e.g.,  $\text{Nb}_2\text{C}$  and  $\text{Nb}_4\text{C}_3\text{T}_x$ ) are with high mechanical strength and good thermal stability, making them suitable for applications in structural materials and coatings. Only  $\text{Nb}_2\text{NF}_2$  exhibits dynamic and thermal stability in the unique ground state.<sup>[375]</sup>

The 2D tungsten carbide MXene NMs ( $\text{W}_2\text{C}$  and  $\text{W}_2\text{CT}_x$ ) with high mechanical strength and good thermal stability, making them promising for use in wear-resistant coatings and cutting tools. Compared to  $\text{Hf}_2\text{CO}_2$ , the  $\text{W}_2\text{CO}_2$  had greater mechanical strength (592.7 GPa).<sup>[224,362]</sup>

Research on 2D non-Ti MXene NMs is still in its early stages, but the unique properties of these materials suggest that they have great potential for a variety of novel applications.

## 8. Future Prospects of Non-Ti MXene Materials: Problems, Outlook, and Solutions

Increasing metal options exterior of their typical family group has created new opportunities for the prospective use of other M metals with advantageous features. Although the theoretical and electrical characteristics of the non-Ti 2D MXene NMs were discussed in this study and only a little amount of research has been done to determine their practical use. The MXenes facing issues are to be solved about preparation of non-Ti MXenes stoichiometric MAX phase with great purity. Other solution is nonstoichiometric phase preparation such as MAB. The double transition metal MXene and multiple-metal incorporated MXene approach can be utilized to obtain tuned properties. The in situ growth of non-Ti MXenes on other MXenes surface can solve the stability issues. The proposed solutions for non-Ti MXenes are discussed in following section.

### 8.1. Non-Ti MAB

Currently, scientists are working to create and incorporate extra X elements into 2D boride systems. Generally, the MAX phase is a frequent precursor of 2D MXene NMs but there is another phase precursor, which is MAB. The MAB produces when X (carbon and/or nitrogen) successfully replaced with B (boron). It is important to assess effective experimental MAX and MAB phase preparations with excellent phase purity. Thus, effective manufacturing techniques should be researched in order to remove the A-layer successfully exclusively producing side results. Since the discovery of MAB phase will require entirely novel study to explore the novel MAB phase combinations that will yield new MBene phases, such as MXene NMs from MAX precursors.

### 8.2. Double Transition Metal MXene and Multiple-Metal Incorporated MXene

Recent research using computing techniques and first-principles investigations has led to the discovery of double TM MXene

NMs.<sup>[33]</sup> The formation of solid solutions on the M and X sites allows for the synthesis of a sizable number of nonstoichiometric MXenes with precisely controlled characteristics and mixed transition metals or carbon nitrides.

Till now only few experimental studies have demonstrated how to make this double TM MXene. The effective conversion of novel ternary and quaternary MAX phases into equivalent MXenes with excellent purity deserves special emphasis, even though several research have examined these phases.<sup>[376]</sup> Thus, appropriate double-metal-MAX phases and etching methods need to be carefully studied. The Ti was the only metal used in the M layer's initial design of MXene. It took the discovery of double TM MXene to introduce a secondary metal by doping in their MAX precursor.<sup>[309]</sup> In light of the evaluation of trimetallic oxides, it may not be difficult to forecast trimetallic TM 2D MXene NMs.

### 8.3. MXene-Derived NMs

According to intriguing research on in situ sulfurization of Mo-based 2D MXene NMs, like 2D  $\text{MoS}_2$  heterostructures successfully developed on MXene NM.<sup>[377]</sup> Strong heterojunctions between MXene and another material are possible with the aid of in situ manufacturing procedures. The 2D MXene NM has also been used to produce metal oxide<sup>[378]</sup> and carbon,<sup>[379]</sup> with potential applications for the chalcogenides group.<sup>[380]</sup> Even though this discovery has a lot of promise, further theoretical and experimental analysis needed to be done. For instance, it is important to carefully consider customized metal cleaving or accurate metal conversions inside single metal or ordered double-metal 2D MXene NMs, correspondingly. Additionally, core-shells/hollow structures, hybrid composites, derivation to metal chalcogenides, hierarchical structure formation (0D to 3D), flexible and conductive current collectors, and transformation to novel MXene materials with special properties may cater to advance applications that may all serve as inspirations.

While progress was attained in the production of TMCs based 2D MXene NMs and in 2D TMNs and non-Ti MXene still has some limitations. To integrate 2D MXene NMs on chips using current microfabrication device nanotechnologies, vapor phase production is essential. Generally non-Ti based 2D MXene NMs will be used in future additive manufacturing techniques based nanotechnologies if large-scale, environmentally friendly manufacturing techniques are introduced. Defined control configuration and surface chemistry, including defects and strain engineering, should cover the approach for theoretically anticipated intrinsically semiconducting, TIs, and ferromagnetic 2D non-Ti MXene NMs, and additional their physics and chemistry breakthroughs. The non-Ti MXene NMs that are mechanically robust, somehow environmentally stable, and highly conductive may have an important influence on flexible, printable, and wearable self-powered electronics. The use of MXene NMs, especially non-Ti MXene NMs in conjunction with other 2D NMs to self-assemble heterostructures and electronics is very interesting idea. Overall, the exploration of non-Ti MXenes offers an opportunity for the discovery of new materials with unique properties and potential applications, as well as the development of more sustainable materials.



## Acknowledgements

K.K. and A.K.T. contributed equally to this work.

## Conflict of Interest

The authors declare no conflict of interest.

## Keywords

non-Ti MXenes, properties of non-Ti MXenes, M-based MXenes, synthesis of non-Ti MXenes, 2D nanomaterials

Received: June 17, 2023

Revised: September 10, 2023

Published online: June 18, 2024

- [1] A. K. Geim, K. S. Novoselov, *Nat. Mater.* **2007**, 6, 183.
- [2] K. Khan, A. K. Tareen, M. Aslam, R. Wang, Y. Zhang, A. Mahmood, Z. Ouyang, H. Zhang, Z. Guo, *J. Mater. Chem. C* **2020**, 8, 387.
- [3] K. Khan, A. K. Tareen, M. Iqbal, A. Mahmood, N. Mahmood, Z. Shi, J. Yin, D. Qing, C. Ma, H. Zhang, *J. Mater. Chem. B* **2021**, 9, 9461.
- [4] K. Khan, A. K. Tareen, M. Aslam, Y. Zhang, R. Wang, Z. Ouyang, Z. Gou, H. Zhang, *Nanoscale* **2019**, 11, 21622.
- [5] F. Cao, et al., *Adv. Mater.* **2021**, 34, 2107554.
- [6] L. Zhang, K. Khan, J. Zou, H. Zhang, Y. Li, *Adv. Mater. Interfaces* **2019**, 6, 1901329.
- [7] H. Hu, Z. Shi, K. Khan, R. Cao, W. Liang, A. K. Tareen, Y. Zhang, W. Huang, Z. Guo, X. Luo, H. Zhang, *J. Mater. Chem. A* **2020**, 8, 5421.
- [8] K. Khan, A. K. Tareen, M. Iqbal, Z. Shi, H. Zhang, Z. Guo, *Nano Today* **2021**, 39, 101207.
- [9] K. Khan, et al., *Prog. Solid State Chem.* **2021**, 63, 100326.
- [10] A. K. Tareen, K. Khan, M. Aslam, X. Liu, H. Zhang, *Prog. Solid State Chem.* **2021**, 61, 100294.
- [11] L. Wang, C. Dai, L. Jiang, G. Tong, Y. Xiong, K. Khan, Z. Tang, X. Chen, H. Zeng, *Small* **2021**, 17, 2100003.
- [12] K. N. Dinh, P. Zheng, Z. Dai, Y. Zhang, R. Dangol, Y. Zheng, B. Li, Y. Zong, Q. Yan, *Small* **2018**, 14, 1703257.
- [13] A. Vahidmohammadi, A. Hadjikhani, S. Shahbazmohammadi, M. Beidaghi, *ACS Nano* **2017**, 11, 11135.
- [14] Z. Shi, et al., *Nano-Micro Lett.* **2020**, 12, 99.
- [15] Z. Shi, et al., *Nano Res.* **2021**, 15, 1.
- [16] K. Khan, et al., *Prog. Solid State Chem.* **2020**, 59, 100283.
- [17] K. Khan, A. K. Tareen, L. Wang, M. Aslam, C. Ma, N. Mahmood, Z. Ouyang, H. Zhang, Z. Guo, *Adv. Funct. Mater.* **2021**, 31, 2005957.
- [18] K. Khan, A. K. Tareen, M. Aslam, R. U. R. Sagar, B. Zhang, W. Huang, A. Mahmood, N. Mahmood, K. Khan, H. Zhang, Z. Guo, *Nano-Micro Lett.* **2020**, 12, 167.
- [19] A. K. Tareen, K. Khan, M. Aslam, H. Zhang, X. Liu, *Nanoscale* **2021**, 13, 510.
- [20] D. Li, Y. Gong, Y. Chen, J. Lin, Q. Khan, Y. Zhang, Y. Li, H. Zhang, H. Xie, *Nano-Micro Lett.* **2020**, 12, 36.
- [21] H. Chen, L. Gao, Z. Qin, Y. Ge, K. Khan, Y. Song, G. Xie, S. Xu, H. Zhang, *Appl. Mater. Today* **2020**, 21, 100800.
- [22] F. Cao, Y. Zhang, H. Wang, K. Khan, A. K. Tareen, W. Qian, H. Zhang, H. Ågren, *Adv. Mater.* **2021**, 34, 2107554.
- [23] H. Hu, Z. Shi, K. Khan, Z. Guo, H. Zhang, *J. Mater. Chem. A* **2020**, 8, 5421.
- [24] K. Khan, A. K. Tareen, M. Iqbal, Y. Zhang, A. Mahmood, N. Mahmood, J. Yin, R. Khatoun, H. Zhang, *Prog. Solid State Chem.* **2022**, 68, 100370.
- [25] K. Khan, A. K. Tareen, M. Aslam, Q. Khan, S. A. Khan, Q. U. Khan, A. S. Saleemi, R. Wang, Y. Zhang, Z. Guo, H. Zhang, Z. Ouyang, *Front. Chem.* **2019**, 7, 738.
- [26] K. Khan, A. K. Tareen, Q. U. Khan, M. Iqbal, H. Zhang, Z. Guo, *Mater. Chem. Front.* **2021**, 5, 6333.
- [27] A. Shayesteh Zeraati, S. A. Mirkhani, P. Sun, M. Naguib, P. V. Braun, U. Sundararaj, *Nanoscale* **2021**, 13, 3572.
- [28] K. Khan, et al., *Prog. Solid State Chem.* **2019**, 58, 100254.
- [29] A. K. Tareen, K. Khan, M. Aslam, X. Liu, H. Zhang, *Prog. Solid State Chem.* **2020**, 61, 100294.
- [30] K. Khan, A. K. Tareen, M. Aslam, K. H. Thebo, U. Khan, R. Wang, S. S. Shams, Z. Han, Z. Ouyang, *Prog. Solid State Chem.* **2019**, 54, 1.
- [31] C. Ma, et al., *Small* **2021**, 17, 2006891.
- [32] M. Naguib, M. Kurtoglu, V. Presser, J. Lu, J. Niu, M. Heon, L. Hultman, Y. Gogotsi, M. W. Barsoum, *Adv. Mater.* **2011**, 23, 4248.
- [33] B. Anasori, Y. Xie, M. Beidaghi, J. Lu, B. C. Hosler, L. Hultman, P. R. C. Kent, Y. Gogotsi, M. W. Barsoum, *ACS Nano* **2015**, 9, 9507.
- [34] A. Vahidmohammadi, J. Rosen, Y. Gogotsi, *Science* **2021**, 372, 1581.
- [35] Y. Wei, P. Zhang, R. A. Soomro, Q. Zhu, B. Xu, *Adv. Mater.* **2021**, 33, 2103148.
- [36] H.-W. Wang, M. Naguib, K. Page, D. J. Wesolowski, Y. Gogotsi, *Chem. Mater.* **2016**, 28, 349.
- [37] C. Lamie, I. Hussain, J. H. Warner, K. Zhang, *Mater. Today* **2023**, 28, 313.
- [38] M. Naguib, V. N. Mochalin, M. W. Barsoum, Y. Gogotsi, *Adv. Mater.* **2014**, 26, 992.
- [39] V. Kamysbayev, A. S. Filatov, H. Hu, X. Rui, F. Lagunas, D. Wang, R. F. Klie, D. V. Talapin, *Science* **2020**, 369, 979.
- [40] C. Zhang, L. Cui, S. Abdolhosseinzadeh, J. Heier, *InfoMat* **2020**, 2, 613.
- [41] F. Ming, H. Liang, G. Huang, Z. Bayhan, H. N. Alshareef, *Adv. Mater.* **2021**, 33, 2004039.
- [42] Y. Huang, Q. Lu, D. Wu, Y. Jiang, Z. Liu, B. Chen, M. Zhu, O. G. Schmidt, *Carbon Energy* **2022**, 4, 598.
- [43] P. Das, Z.-S. Wu, *J. Phys.: Condens. Matter* **2020**, 2, 032004.
- [44] A. K. Tareen, K. Khan, M. Iqbal, Y. Zhang, J. Long, A. Mahmood, N. Mahmood, Z. Xie, C. Li, H. Zhang, *Energy Storage Mater.* **2022**, 2, 783.
- [45] M. W. Barsoum, *MAX Phases: Properties of Machinable Ternary Carbides and Nitrides*, John Wiley & Sons, New York **2013**.
- [46] Y. Wang, et al., *Adv. Mater.* **2022**, 34, 2108560.
- [47] M. A. Hadi, *J. Phys. Chem. Solids* **2020**, 138, 109275.
- [48] B. Anasori, Y. Gogotsi, *2D Metal Carbides and Nitrides (MXenes)*, Springer, New York, NY, USA **2019**.
- [49] J.-P. Palmquist, S. Li, P. O. Å. Persson, J. Emmerlich, O. Wilhelmsson, H. Höglberg, M. I. Katsnelson, B. Johansson, R. Ahuja, O. Eriksson, L. Hultman, U. Jansson, *Phys. Rev. B* **2004**, 70, 165401.
- [50] M. Sokol, V. N. Natu, S. Kota, M. W. Barsoum, *Trends Chem.* **2019**, 1, 210.
- [51] W. Sohn, K. C. Kwon, J. M. Suh, T. H. Lee, K. C. Roh, H. W. Jang, *Nano Convergence* **2021**, 8, 210.
- [52] S. T. Oyama, *Catal. Today* **1992**, 15, 179.
- [53] E. Wuchina, E. Opila, M. Opeka, B. Fahrenholtz, I. Talmy, *Electrochem. Soc. Interface* **2007**, 16, 30.
- [54] Y. Gogotsi, B. Anasori, *Meml. Serv. Exploit. Ind. Tab. Allumettes, Ser. B* **2019**, 13, 8491.
- [55] J. Zhou, X. Zha, X. Zhou, F. Chen, G. Gao, S. Wang, C. Shen, T. Chen, C. Zhi, P. Eklund, S. Du, J. Xue, W. Shi, Z. Chai, Q. Huang, *ACS Nano* **2017**, 11, 3841.
- [56] B. Anasori, Y. Gogotsi, *2D Metal Carbides and Nitrides (MXenes): Structure, Properties and Applications*, Springer Nature, Switzerland **2019**.
- [57] M. Alhabeb, K. Maleski, B. Anasori, P. Lelyukh, L. Clark, S. Sin, Y. Gogotsi, *Chem. Mater.* **2017**, 29, 7633.

- [58] Y. Li, H. Shao, Z. Lin, J. Lu, L. Liu, B. Duployer, P. O. Å. Persson, P. Eklund, L. Hultman, M. Li, K. Chen, X.-H. Zha, S. Du, P. Rozier, Z. Chai, E. Raymundo-Piñero, P.-L. Taberna, P. Simon, Q. Huang, *Nat. Mater.* **2020**, *19*, 894.
- [59] K. R. Mikeska, S. J. Bennison, S. L. Grise, *J. Am. Ceram. Soc.* **2000**, *83*, 1160.
- [60] R. Khaledialidusti, M. Khazaei, S. Khazaei, K. Ohno, *Nanoscale* **2021**, *13*, 7294.
- [61] A. Gkountaras, Y. Kim, J. Coraux, V. Bouchiat, S. Lisi, M. W. Barsoum, T. Ouisse, *Small* **2020**, *16*, 1905784.
- [62] M. Dahlqvist, J. Rosen, *Nanoscale* **2020**, *12*, 785.
- [63] K. R. G. Lim, M. Shekhirev, B. C. Wyatt, B. Anasori, Y. Gogotsi, Z. W. Seh, *Anti-Cancer Drugs: Nat., Synth. Cell* **2022**, *1*, 601.
- [64] M. Khazaei, A. Ranjbar, K. Esfarjani, D. Bogdanovski, R. Dronskowski, S. Yunoki, *Phys. Chem. Chem. Phys.* **2018**, *20*, 8579.
- [65] P. Urbankowski, B. Anasori, T. Makaryan, D. Er, S. Kota, P. L. Walsh, M. Zhao, V. B. Shenoy, M. W. Barsoum, Y. Gogotsi, *Nanoscale* **2016**, *8*, 11385.
- [66] M. Magnuson, M. Mattesini, *Thin Solid Films* **2017**, *621*, 108.
- [67] D. Johnson, Z. Qiao, E. Uwadiunor, A. Djire, *Small* **2022**, *18*, 2106129.
- [68] S. Kirklin, B. Meredig, C. Wolverton, *Adv. Energy Mater.* **2013**, *3*, 252.
- [69] M. Han, C. E. Shuck, R. Rakhmanov, D. Parchment, B. Anasori, C. M. Koo, G. Friedman, Y. Gogotsi, *ACS Nano* **2020**, *14*, 5008.
- [70] M. Alhabeb, K. Maleski, T. S. Mathis, A. Sarycheva, C. B. Hatter, S. Uzun, A. Levitt, Y. Gogotsi, *Angew. Chem., Int. Ed.* **2018**, *57*, 5444.
- [71] T. Lapauw, B. Tunca, T. Cabioc'h, J. Lu, P. O. Å. Persson, K. Lambrinou, J. Vleugels, *Inorg. Chem.* **2016**, *55*, 10922.
- [72] Z. Sun, Y. Zou, S. Tada, H. Hashimoto, *Scr. Mater.* **2006**, *55*, 1011.
- [73] S. N. Perevislov, T. V. Sokolova, V. L. Stolyarova, *Mater. Chem. Phys.* **2021**, *267*, 124625.
- [74] T. S. Mathis, K. Maleski, A. Goad, A. Sarycheva, M. Anayee, A. C. Foucher, K. Hantanasirisakul, C. E. Shuck, E. A. Stach, Y. Gogotsi, *ACS Nano* **2021**, *15*, 6420.
- [75] W. Chen, J. Tang, X. Shi, N. Ye, Z. Yue, X. Lin, *Int. J. Appl. Ceram. Technol.* **2020**, *17*, 778.
- [76] M. Li, J. Lu, K. Luo, Y. Li, K. Chang, K. Chen, J. Zhou, J. Rosen, L. Hultman, P. Eklund, P. O. Å. Persson, S. Du, Z. Chai, Z. Huang, Q. Huang, *J. Am. Chem. Soc.* **2019**, *141*, 4730.
- [77] A. E. Sychev, M. L. Busurina, N. V. Sachkova, D. Vrel, *Inorg. Mater.* **2019**, *55*, 780.
- [78] D. P. Riley, E. H. Kisi, *J. Am. Ceram. Soc.* **2007**, *90*, 2231.
- [79] C. E. Shuck, M. Han, K. Maleski, K. Hantanasirisakul, S. J. Kim, J. Choi, W. E. B. Reil, Y. Gogotsi, *ACS Appl. Nano Mater.* **2019**, *2*, 3368.
- [80] K. A. Papadopolou, D. Parfitt, A. Chroneos, S.-R. G. Christopoulos, *J. Appl. Phys.* **2021**, *130*, 095101.
- [81] J. Halim, K. M. Cook, M. Naguib, P. Eklund, Y. Gogotsi, J. Rosen, M. W. Barsoum, *Appl. Surf. Sci.* **2016**, *362*, 406.
- [82] V. Natsu, R. Pai, M. Sokol, M. Carey, V. Kalra, M. W. Barsoum, *Chem* **2020**, *6*, 616.
- [83] J. Luo, J. Zheng, J. Nai, C. Jin, H. Yuan, O. Sheng, Y. Liu, R. Fang, W. Zhang, H. Huang, Y. Gan, Y. Xia, C. Liang, J. Zhang, W. Li, X. Tao, *Adv. Funct. Mater.* **2019**, *29*, 1808107.
- [84] O. Mashtalir, M. Naguib, V. N. Mochalin, Y. Dall'agnese, M. Heon, M. W. Barsoum, Y. Gogotsi, *Nat. Commun.* **2013**, *4*, 1716.
- [85] M. Naguib, R. R. Unocic, B. L. Armstrong, J. Nanda, *Dalton Trans.* **2015**, *44*, 9353.
- [86] F. Han, et al., *ACS Appl. Mater. Interfaces* **2019**, *11*, 8443.
- [87] W. Wu, J. Xu, X. Tang, P. Xie, X. Liu, J. Xu, H. Zhou, D. i Zhang, T. Fan, *Chem. Mater.* **2018**, *30*, 5932.
- [88] Y.-E. Shi, F. Han, L. Xie, C. Zhang, T. Li, H. Wang, W.-F. Lai, S. Luo, W. Wei, Z. Wang, Y. Huang, *Microchim. Acta* **2019**, *187*, 38.
- [89] M. Malaki, A. Maleki, R. S. Varma, *J. Mater. Chem. A* **2019**, *7*, 10843.
- [90] Q. Zhang, H. Lai, R. Fan, P. Ji, X. Fu, H. Li, *ACS Nano* **2021**, *15*, 5249.
- [91] L. Bi, Z. Yang, L. Chen, Z. Wu, C. Ye, *J. Mater. Chem. A* **2020**, *8*, 20030.
- [92] Z. Cao, Q. Zhu, S. Wang, D. Zhang, H. Chen, Z. Du, B. Li, S. Yang, *Adv. Funct. Mater.* **2020**, *30*, 1908075.
- [93] W. Sun, Y. Xie, P. R. C. Kent, *Nanoscale* **2018**, *10*, 20030.
- [94] M. Dahlqvist, J. Lu, R. Meshkian, Q. Tao, L. Hultman, J. Rosen, *Sci. Adv.* **2017**, *3*, 1908075.
- [95] Q. Tao, M. Dahlqvist, J. Lu, S. Kota, R. Meshkian, J. Halim, J. Palisaitis, L. Hultman, M. W. Barsoum, P. O. Å. Persson, J. Rosen, *Nat. Commun.* **2017**, *8*, 14949.
- [96] B. Ahmed, A. El Ghazaly, J. Rosen, *Adv. Funct. Mater.* **2020**, *30*, 2000894.
- [97] R. Meshkian, et al., *Adv. Mater.* **2018**, *30*, 1706409.
- [98] I. Persson, A. El Ghazaly, Q. Tao, J. Halim, S. Kota, V. Darakchieva, J. Palisaitis, M. W. Barsoum, J. Rosen, P. O. Å. Persson, *Small* **2018**, *30*, 1703676.
- [99] J. C. Schuster, H. Nowotny, C. Vaccaro, *J. Solid State Chem.* **1980**, *32*, 213.
- [100] D. Pinto, B. Anasori, H. Avireddy, C. E. Shuck, K. Hantanasirisakul, G. Deysher, J. R. Morante, W. Porzio, H. N. Alshareef, Y. Gogotsi, *J. Mater. Chem. A* **2020**, *8*, 8957.
- [101] Z. Liu, L. Zheng, L. Sun, Y. Qian, J. Wang, M. Li, *J. Am. Ceram. Soc.* **2014**, *97*, 67.
- [102] R. Meshkian, Q. Tao, M. Dahlqvist, J. Lu, L. Hultman, J. Rosen, *Acta Mater.* **2017**, *125*, 476.
- [103] Q. Tao, M. Dahlqvist, J. Lu, S. Kota, R. Meshkian, J. Halim, J. Palisaitis, L. Hultman, M. W. Barsoum, P. O. Å. Persson, J. Rosen, *Nat. Commun.* **2017**, *8*, 67.
- [104] M. Dahlqvist, et al., *Sci. Adv.* **2017**, *3*, 1700642.
- [105] J. Halim, J. Palisaitis, J. Lu, J. Thörnberg, E. J. Moon, M. Precner, P. Eklund, P. O. Å. Persson, M. W. Barsoum, J. Rosen, *ACS Appl. Nano Mater.* **2018**, *1*, 2455.
- [106] I. Persson, A. El Ghazaly, Q. Tao, J. Halim, S. Kota, V. Darakchieva, J. Palisaitis, M. W. Barsoum, J. Rosen, P. O. Å. Persson, *Small* **2018**, *14*, 1703676.
- [107] Z. Lin, M. Zhuo, Y. Zhou, M. Li, J. Wang, *J. Am. Ceram. Soc.* **2006**, *89*, 3765.
- [108] G. Deysher, C. E. Shuck, K. Hantanasirisakul, N. C. Frey, A. C. Foucher, K. Maleski, A. Sarycheva, V. B. Shenoy, E. A. Stach, B. Anasori, Y. Gogotsi, *ACS Nano* **2019**, *14*, 204.
- [109] Z. Du, C. Wu, Y. Chen, Z. Cao, R. Hu, Y. Zhang, J. Gu, Y. Cui, H. Chen, Y. Shi, J. Shang, B. Li, S. Yang, *Adv. Mater.* **2021**, *33*, 2101473.
- [110] M. Han, K. Maleski, C. E. Shuck, Y. Yang, J. T. Glazar, A. C. Foucher, K. Hantanasirisakul, A. Sarycheva, N. C. Frey, S. J. May, V. B. Shenoy, E. A. Stach, Y. Gogotsi, *J. Am. Chem. Soc.* **2020**, *142*, 19110.
- [111] B. Soundiraraju, B. K. George, *ACS Nano* **2017**, *11*, 8892.
- [112] A. Djire, A. Bos, J. Liu, H. Zhang, E. M. Miller, N. R. Neale, *ACS Appl. Nano Mater.* **2019**, *2*, 2785.
- [113] B. Anasori, M. R. Lukatskaya, Y. Gogotsi, *Nat. Rev. Mater.* **2017**, *2*, 11385.
- [114] Y. Yoon, A. P. Tiwari, M. Lee, M. Choi, W. Song, J. Im, T. Zyung, H.-K. Jung, S. S. Lee, S. Jeon, K.-S. An, *J. Mater. Chem. A* **2018**, *6*, 20869.
- [115] X. Xiao, H. Yu, H. Jin, M. Wu, Y. Fang, J. Sun, Z. Hu, T. Li, J. Wu, L. Huang, Y. Gogotsi, J. Zhou, *ACS Nano* **2017**, *11*, 2180.
- [116] M. Seredych, C. E. Shuck, D. Pinto, M. Alhabeb, E. Precetti, G. Deysher, B. Anasori, N. Kurra, Y. Gogotsi, *Chem. Mater.* **2019**, *31*, 3324.
- [117] X. Wang, X. i Shen, Y. Gao, Z. Wang, R. Yu, L. Chen, *J. Am. Chem. Soc.* **2015**, *137*, 2715.
- [118] I. Persson, et al., *2D Mater.* **2018**, *11*, 3841.
- [119] K. J. Harris, M. Bugnet, M. Naguib, M. W. Barsoum, G. R. Goward, *J. Phys. Chem. C* **2015**, *119*, 13713.
- [120] T. Schultz, N. C. Frey, K. Hantanasirisakul, S. Park, S. J. May, V. B. Shenoy, Y. Gogotsi, N. Koch, *Chem. Mater.* **2019**, *31*, 6590.



- [121] J. L. Hart, K. Hantanasirisakul, A. C. Lang, B. Anasori, D. Pinto, Y. Pivak, J. T. Van Omme, S. J. May, Y. Gogotsi, M. L. Taheri, *Nat. Commun.* **2019**, *10*, 2715.
- [122] I. Persson, J. Halim, T. W. Hansen, J. B. Wagner, V. Darakchieva, J. Palisaitis, J. Rosen, P. O. Å. Persson, *Adv. Funct. Mater.* **2020**, *30*, 1909005.
- [123] R. Thakur, A. Vahidmohammadi, J. Moncada, W. R. Adams, M. Chi, B. Tatarchuk, M. Beidaghi, C. A. Carrero, *Nanoscale* **2019**, *11*, 10716.
- [124] D. L. Druffel, K. L. Kuntz, A. H. Woormer, F. M. Alcorn, J. Hu, C. L. Donley, S. C. Warren, *J. Am. Chem. Soc.* **2016**, *138*, 16089.
- [125] K. Hantanasirisakul, Y. Gogotsi, *Adv. Mater.* **2018**, *30*, 1804779.
- [126] L. Verger, et al., *Curr. Opin. Solid State Mater. Sci.* **2019**, *23*, 149.
- [127] C. E. Shuck, A. Sarycheva, M. Anayee, A. Levitt, Y. Zhu, S. Uzun, V. Balitskiy, V. Zahorodna, O. Gogotsi, Y. Gogotsi, *Adv. Eng. Mater.* **2020**, *22*, 1901241.
- [128] O. Mashtalir, M. Naguib, B. Dyatkin, Y. Gogotsi, M. W. Barsoum, *Mater. Chem. Phys.* **2013**, *139*, 147.
- [129] X. Sang, Y. Xie, M.-W. Lin, M. Alhabeb, K. L. Van Aken, Y. Gogotsi, P. R. C. Kent, K. Xiao, R. R. Unocic, *ACS Nano* **2016**, *10*, 9193.
- [130] Q. i Meng, C. Yang, X. Tai, K. Cheng, P. Li, H. Li, X. Liu, S. Liu, *J. Phys.: Condens. Matter* **2022**, *34*, 453001.
- [131] M. Naguib, M. W. Barsoum, Y. Gogotsi, *Adv. Mater.* **2021**, *33*, 2103393.
- [132] M. A. Hope, A. C. Forse, K. J. Griffith, M. R. Lukatskaya, M. Ghidui, Y. Gogotsi, C. P. Grey, *Phys. Chem. Chem. Phys.* **2016**, *18*, 5099.
- [133] M. Ghidui, M. R. Lukatskaya, M.-Q. Zhao, Y. Gogotsi, M. W. Barsoum, *Nature* **2014**, *516*, 78.
- [134] Q. Tang, Z. Zhou, P. Shen, *J. Am. Chem. Soc.* **2012**, *134*, 16909.
- [135] W. Sun, S. A. Shah, Y. Chen, Z. Tan, H. Gao, T. Habib, M. Radovic, M. J. Green, *J. Mater. Chem. A* **2017**, *5*, 21663.
- [136] S. Yang, P. Zhang, F. Wang, A. G. Ricciardulli, M. R. Lohe, P. W. M. Blom, X. Feng, *Angew. Chem., Int. Ed.* **2018**, *57*, 15491.
- [137] T. Li, L. Yao, Q. Liu, J. Gu, R. Luo, J. Li, X. Yan, W. Wang, P. Liu, B. Chen, W. Zhang, W. Abbas, R. Naz, D. Zhang, *Angew. Chem., Int. Ed.* **2018**, *57*, 6115.
- [138] J. Zhou, et al., *ACS Nano* **2019**, *13*, 1195.
- [139] Q. Chen, D. Zhang, J. Pan, W. Fan, *Optik* **2020**, *219*, 165046.
- [140] L. Wang, et al., *ACS Appl. Mater. Interfaces* **2016**, *8*, 16396.
- [141] A. Vahidmohammadi, W. Liang, M. Mojtavavi, M. Wanunu, M. Beidaghi, *Energy Storage Mater.* **2021**, *41*, 554.
- [142] Y. Yoon, A. P. Tiwari, M. Choi, T. G. Novak, W. Song, H. Chang, T. Zyung, S. S. Lee, S. Jeon, K.-S. An, *Adv. Funct. Mater.* **2019**, *29*, 1903443.
- [143] P. Kuang, M. He, B. Zhu, J. Yu, K. Fan, M. Jaroniec, *J. Catal.* **2019**, *375*, 8.
- [144] H. Hu, H. Huang, L. Xia, X. Qian, W. Feng, Y. Chen, Y. Li, *Chem. Eng. J.* **2022**, *440*, 135810.
- [145] J. Geng, R. Wu, H. Bai, I.-N. Chan, K. W. Ng, W. F. Ip, H. Pan, *Int. J. Hydrogen Energy* **2022**, *47*, 18725.
- [146] W. Sun, Y. Xie, P. R. C. Kent, *Nanoscale* **2018**, *10*, 11962.
- [147] W. Feng, X. Han, H. Hu, M. Chang, L. Ding, H. Xiang, Y. Chen, Y. Li, *Nat. Commun.* **2021**, *12*, 2203.
- [148] R. Thakur, A. Vahidmohammadi, J. Smith, M. Hoffman, J. Moncada, M. Beidaghi, C. A. Carrero, *ACS Catal.* **2020**, *10*, 5124.
- [149] S. Zada, W. Dai, Z. Kai, H. Lu, X. Meng, Y. Zhang, Y. Cheng, F. Yan, P. Fu, X. Zhang, H. Dong, *Angew. Chem., Int. Ed.* **2020**, *59*, 6601.
- [150] Y. Guan, et al., *2D Mater.* **2020**, *7*, 025010.
- [151] C. Wang, et al., *Adv. Energy Mater.* **2019**, *9*, 1802977.
- [152] C. Si, J. Zhou, Z. Sun, *ACS Appl. Mater. Interfaces* **2015**, *7*, 17510.
- [153] A. Yadav, A. Dashora, N. Patel, A. Miotello, M. Press, D. C. Kothari, *Appl. Surf. Sci.* **2016**, *389*, 88.
- [154] M. Je, Y. Lee, Y.-C. Chung, *Thin Solid Films* **2016**, *619*, 131.
- [155] Q. Sun, Z. Fu, Z. Yang, *J. Magn. Magn. Mater.* **2020**, *514*, 167141.
- [156] I. A. M. Ibrahim, S. Abdel-Azeim, A. M. El-Nahas, O. Kühn, C.-Y. Chung, A. El-Zatahy, M. F. Shibl, *J. Phys. Chem. C* **2022**, *126*, 14886.
- [157] M. Naguib, Y. Gogotsi, M. W. Barsoum, in *Electrochemical Society Meeting Abstracts 227*, The Electrochemical Society, Inc, Philadelphia **2016**, pp. 849–849.
- [158] B. Soundiraraju, R. Raghavan, B. K. George, *ACS Appl. Nano Mater.* **2020**, *3*, 11007.
- [159] X. Zou, H. Liu, H. Xu, X. Wu, X. Han, J. Kang, K. M. Reddy, *Mater. Today Energy* **2021**, *20*, 100668.
- [160] P. Sharma, O. P. Pandey, *J. Therm. Anal. Calorim.* **2021**, *143*, 3997.
- [161] B. Shalini Reghunath, D. Davis, K. R. Sunaja Devi, *Chemosphere* **2021**, *283*, 131281.
- [162] A. M. Abdelkader, *J. Eur. Ceram. Soc.* **2016**, *36*, 33.
- [163] J. M. Schneider, Z. Sun, R. Mertens, F. Uestel, R. Ahuja, *Solid State Commun.* **2004**, *130*, 445.
- [164] J. P. Siebert, L. Bischoff, M. Lepple, A. Zintler, L. Molina-Luna, U. Wiedwald, C. S. Birkel, *J. Mater. Chem. C* **2019**, *7*, 6034.
- [165] M. H. Tran, A. M. Malik, M. Dürschnabel, A. Regoutz, P. Thakur, T.-L. Lee, D. Perera, L. Molina-Luna, K. Albe, J. Rohrer, C. S. Birkel, *Dalton Trans.* **2020**, *49*, 12215.
- [166] N. C. Frey, J. Wang, G. I. Vega Bellido, B. Anasori, Y. Gogotsi, V. B. Shenoy, *ACS Nano* **2019**, *13*, 3031.
- [167] S.-Y. Pang, Y.-T. Wong, S. Yuan, Y. Liu, M.-K. Tsang, Z. Yang, H. Huang, W.-T. Wong, J. Hao, *J. Am. Chem. Soc.* **2019**, *141*, 9610.
- [168] Y.-W. Cheng, J.-H. Dai, Y.-M. Zhang, Y. Song, *J. Mater. Chem. A* **2018**, *6*, 20956.
- [169] A. S. Tarasov, et al., *Processes* **2023**, *11*, 2236.
- [170] G. Zhao, J. Chen, Y. Li, L. Zheng, J. Li, X. Wang, M. Li, *J. Eur. Ceram. Soc.* **2017**, *37*, 83.
- [171] D. L. Druffel, M. G. Lanetti, J. D. Sundberg, J. T. Pawlik, M. S. Stark, C. L. Donley, L. M. Mcrae, K. M. Scott, S. C. Warren, *Chem. Mater.* **2019**, *31*, 9788.
- [172] S. Sun, J. Yang, X. Chen, W. Cui, J. Huang, T. Yang, Z. Zhang, Q. Wang, *Scr. Mater.* **2020**, *181*, 10.
- [173] K. Maeda, H. Wakayama, Y. Washio, A. Ishikawa, M. Okazaki, H. Nakata, S. Matsuishi, *J. Phys. Chem. C* **2020**, *124*, 14640.
- [174] Y.-C. Zhou, L.-F. He, Z.-J. Lin, J.-Y. Wang, *J. Eur. Ceram. Soc.* **2013**, *33*, 2831.
- [175] S. Mikhaleenko, *Damping Multiphase Inorg. Mater., Proc. Damping Multiphase Inorg. Mater. Symp.* **1979**, *15*, 1532.
- [176] J. C. Schuster, H. Nowotny, *Int. J. Mater. Res.* **1980**, *71*, 341.
- [177] J. Zhou, X. Zha, F. Y. Chen, Q. Ye, P. Eklund, S. Du, Q. Huang, *Angew. Chem., Int. Ed.* **2016**, *55*, 5008.
- [178] J. Wang, et al., *ACS Appl. Mater. Interfaces* **2023**, *15*, 3317.
- [179] L. F. He, Y. W. Bao, J. Y. Wang, M. S. Li, Y. C. Zhou, *Acta Mater.* **2009**, *57*, 2765.
- [180] T. Lapauw, et al., *Inorg. Chem.* **2016**, *55*, 10922.
- [181] K. Fukuda, M. Hisamura, T. Iwata, N. Tera, K. Sato, *J. Solid State Chem.* **2007**, *180*, 1809.
- [182] L. F. He, H. Q. Nian, X. P. Lu, Y. W. Bao, Y. C. Zhou, *Scr. Mater.* **2010**, *62*, 427.
- [183] X. Zhang, J. Xu, H. Wang, J. Zhang, H. Yan, B. Pan, J. Zhou, Y. i Xie, *Angew. Chem., Int. Ed.* **2013**, *52*, 4361.
- [184] C. Ougherb, T. Ouahrani, M. Badawi, Á. Morales-García, *Phys. Chem. Chem. Phys.* **2022**, *24*, 7243.
- [185] P. A. Rasheed, R. P. Pandey, F. Banat, S. W. Hasan, *Matter* **2022**, *5*, 546.
- [186] H. Lin, S. Gao, C. Dai, Y. Chen, J. Shi, *J. Am. Chem. Soc.* **2017**, *139*, 16235.
- [187] Y. Wang, Y. Wang, K. Chen, K. Qi, T. Xue, H. Zhang, J. He, S. Xiao, *ACS Nano* **2020**, *14*, 10492.
- [188] L. Gao, C. Ma, S. Wei, A. V. Kuklin, H. Zhang, H. Ågren, *ACS Nano* **2021**, *15*, 954.

- [189] M. Song, S. Y. Pang, F. Guo, M. C. Wong, J. Hao, *Adv. Sci.* **2020**, 7, 2001546.
- [190] W. L. Zhang, J. Tian, H. Zeng, J. Liu, Y. Tian, *Chem. Eng. J.* **2019**, 366, 321.
- [191] S. Y. Pang, W. F. Io, L. W. Wong, J. Zhao, J. Hao, *Adv. Sci.* **2020**, 7, 1903680.
- [192] S. Tu, F. Ming, J. Zhang, X. Zhang, H. N. Alshareef, *Adv. Mater.* **2019**, 31, 1806860.
- [193] A. Byeon, A. M. Glushenkov, B. Anasori, P. Urbankowski, J. Li, B. W. Byles, B. Blake, K. L. Van Aken, S. Kota, E. Pomerantseva, J. W. Lee, Y. Chen, Y. Gogotsi, *J. Power Sources* **2016**, 326, 686.
- [194] Z. Lan, H. Fu, R. Zhao, H. Liu, W. Zhou, H. Ning, J. Guo, *Chem. Eng. J.* **2022**, 431, 133985.
- [195] C. Peng, P. Wei, X. Chen, Y. Zhang, F. Zhu, Y. Cao, H. Wang, H. Yu, F. Peng, *Ceram. Int.* **2018**, 44, 18886.
- [196] G. Li, J. Liu, F. Wang, H. Nie, R. Wang, K. Yang, B. Zhang, J. He, *Adv. Mater. Interfaces* **2021**, 8, 2001805.
- [197] W. Feng, R. Wang, Y. Zhou, L. Ding, X. Gao, B. Zhou, P. Hu, Y. Chen, *Adv. Funct. Mater.* **2019**, 29, 1901942.
- [198] R. Meshkian, L.-Å. Näslund, J. Halim, J. Lu, M. W. Barsoum, J. Rosen, *Scr. Mater.* **2015**, 108, 147.
- [199] J. Halim, S. Kota, M. R. Lukatskaya, M. Naguib, M.-Q. Zhao, E. J. Moon, J. Pitock, J. Nanda, S. J. May, Y. Gogotsi, M. W. Barsoum, *Adv. Funct. Mater.* **2016**, 26, 3118.
- [200] M. Ade, H. Hillebrecht, *Inorg. Chem.* **2015**, 54, 6122.
- [201] W. Xiong, X. Feng, Y. Xiao, T. Huang, X. Li, Z. Huang, S. Ye, Y. Li, X. Ren, X. Wang, X. Ouyang, Q. Zhang, J. Liu, *Chem. Eng. J.* **2022**, 446, 137466.
- [202] J. Jeon, Y. Park, S. Choi, J. Lee, S. S. Lim, B. H. Lee, Y. J. Song, J. H. Cho, Y. H. Jang, S. Lee, *ACS Nano* **2018**, 12, 338.
- [203] L. Zhao, B. Li, *Tungsten* **2020**, 2, 176.
- [204] D. Geng, X. Zhao, Z. Chen, W. Sun, W. Fu, J. Chen, W. Liu, W. Zhou, K. P. Loh, *Adv. Mater.* **2017**, 29, 1700072.
- [205] S. Joshi, Q. Wang, A. Puntambekar, V. Chakrapani, *ACS Energy Lett.* **2017**, 2, 1257.
- [206] G.-D. Sun, H.-Q. Chang, G.-H. Zhang, B.-J. Yan, K.-C. Chou, *J. Am. Ceram. Soc.* **2019**, 102, 7178.
- [207] J. Wang, S. Liu, Y. Wang, T. Wang, S. Shang, W. Ren, *J. Mater. Chem. C* **2020**, 8, 1608.
- [208] R. Syamsai, A. N. Grace, *J. Alloys Compd.* **2019**, 792, 1230.
- [209] B. Gao, Y.-Y. Li, C.-Y. Ma, Y.-Q. Shu, G. Wu, B.-K. Chen, J.-Y. Huo, Y. Han, L. Liu, Y. Zhang, *J. Alloys Compd.* **2022**, 900, 163529.
- [210] A. Rafieerad, W. Yan, K. N. Alagarsamy, A. Srivastava, N. Sareen, R. C. Arora, S. Dhingra, *Adv. Funct. Mater.* **2021**, 31, 2106786.
- [211] Y. Liu, X. Ji, J. Liu, W. W. L. Tong, D. Askhatova, J. Shi, *Adv. Funct. Mater.* **2017**, 27, 1703261.
- [212] M. Cover, O. Warschkow, M. Bilek, D. McKenzie, *J. Phys.: Condens. Matter* **2009**, 21, 305403.
- [213] B. Ahmed, A. E. Ghazaly, J. Rosen, *Adv. Funct. Mater.* **2020**, 30, 2000894.
- [214] M. Dahlqvist, A. Petruhins, J. Lu, L. Hultman, J. Rosen, *ACS Nano* **2018**, 12, 7761.
- [215] Q. Tao, J. Lu, M. Dahlqvist, A. Mockute, S. Calder, A. Petruhins, R. Meshkian, O. Rivin, D. Potashnikov, E. I. N. Caspi, H. Shaked, A. Hoser, C. Opagiste, R.-M. Galera, R. Salikhov, U. Wiedwald, C. Ritter, A. R. Wildes, B. Johansson, L. Hultman, M. Farle, M. W. Barsoum, J. Rosen, *Chem. Mater.* **2019**, 31, 2476.
- [216] R. Meshkian, H. Lind, J. Halim, A. El Ghazaly, J. Thörnberg, Q. Tao, M. Dahlqvist, J. Palisaitis, P. O. Å. Persson, J. Rosen, *ACS Appl. Nano Mater.* **2019**, 2, 6209.
- [217] J. Yang, et al., *Carbon* **2021**, 183, 76.
- [218] R. K. Choudhury, B. R. Bhagat, K. H. Mali, R. Pokar, A. Dashora, *Appl. Surf. Sci.* **2022**, 603, 154426.
- [219] B. Anasori, J. Halim, J. Lu, C. A. Voigt, L. Hultman, M. W. Barsoum, *Scr. Mater.* **2015**, 101, 5.
- [220] Z. Shen, Z. Wang, M. Zhang, M. Gao, J. Hu, F. Du, Y. Liu, H. Pan, *Materialia* **2018**, 1, 114.
- [221] Z. Liu, E. Wu, J. Wang, Y. Qian, H. Xiang, X. Li, Q. Jin, G. Sun, X. Chen, J. Wang, M. Li, *Acta Mater.* **2014**, 73, 186.
- [222] C. M. Hamm, J. D. Bocarsly, G. Seward, U. I. Kramm, C. S. Birkel, *J. Mater. Chem. C* **2017**, 5, 5700.
- [223] Y. Lee, Y. Hwang, Y.-C. Chung, *ACS Appl. Mater. Interfaces* **2015**, 7, 7163.
- [224] X.-H. Zha, K. Luo, Q. Li, Q. Huang, J. He, X. Wen, S. Du, *Europhys. Lett.* **2015**, 111, 26007.
- [225] X. Bai, X.-H. Zha, Y. Qiao, N. Qiu, Y. Zhang, K. Luo, J. He, Q. Li, Q. Huang, J. S. Francisco, C.-T. Lin, S. Du, *Nanoscale* **2020**, 12, 3795.
- [226] A. S. Ingason, A. Petruhins, M. Dahlqvist, F. Magnus, A. Mockute, B. Alling, L. Hultman, I. A. Abrikosov, P. O. Å. Persson, J. Rosen, *Mater. Res. Lett.* **2014**, 2, 89.
- [227] M. Khazaei, A. Ranjbar, M. Arai, T. Sasaki, S. Yunoki, *J. Mater. Chem. C* **2017**, 5, 2488.
- [228] B. Anasori, C. Shi, E. J. Moon, Y. Xie, C. A. Voigt, P. R. C. Kent, S. J. May, S. J. L. Billinge, M. W. Barsoum, Y. Gogotsi, *Nanoscale Horiz.* **2016**, 1, 227.
- [229] N. M. Caffrey, *Nanoscale* **2018**, 10, 13520.
- [230] Y. Liu, H. Xiao, W. A. Goddard, *J. Am. Chem. Soc.* **2016**, 138, 15853.
- [231] M. Khazaei, M. Arai, T. Sasaki, M. Estili, Y. Sakka, *Phys. Chem. Chem. Phys.* **2014**, 16, 7841.
- [232] Michael, et al., *Dalton Trans.* **2015**, 2, 89.
- [233] L. Wu, et al., *Laser Photonics Rev.* **2018**, 12, 1800215.
- [234] K. Maleski, C. E. Ren, M.-Q. Zhao, B. Anasori, Y. Gogotsi, *ACS Appl. Mater. Interfaces* **2018**, 10, 24491.
- [235] K. Hantanasirisakul, B. Anasori, S. Nemsak, J. L. Hart, J. Wu, Y. Yang, R. V. Chopdekar, P. Shafer, A. F. May, E. J. Moon, J. Zhou, Q. Zhang, M. L. Taheri, S. J. May, Y. Gogotsi, *Nanoscale Horiz.* **2020**, 5, 1557.
- [236] Gogotsi, Y. Liu, H. Xiao, W. A. Goddard, Tunable Magnetism and Transport Properties in Nitride MXenes.
- [237] Z. Yong, L. Feng, *J. Magn. Magn. Mater.* **2017**, 433, 222.
- [238] Guoying, et al., *Nanoscale* **2016**, 44, 9353.
- [239] L. Hu, X. Wu, J. Yang, *Nanoscale* **2016**, 12, 12939.
- [240] J. He, P. Lyu, P. Nachtigall, *J. Mater. Chem. C* **2016**, 10, 11143.
- [241] J. L. Hart, K. Hantanasirisakul, A. C. Lang, B. Anasori, D. Pinto, Y. Pivak, J. T. Van Omme, S. J. May, Y. Gogotsi, M. L. Taheri, *Nat. Commun.* **2019**, 10, 1557.
- [242] J. K. El-Demellawi, S. Lopatin, J. Yin, O. F. Mohammed, H. N. Alshareef, *ACS Nano* **2018**, 12, 8485.
- [243] K. Maleski, C. E. Shuck, A. T. Fafarman, Y. Gogotsi, *Adv. Opt. Mater.* **2021**, 9, 2001563.
- [244] C. (J.) Zhang, B. Anasori, A. Seral-Ascaso, S.-H. Park, N. Mcevoy, A. Shmeliov, G. S. Duesberg, J. N. Coleman, Y. Gogotsi, V. Nicolosi, *Adv. Mater.* **2017**, 29, 1702678.
- [245] G. Ying, S. Kota, A. D. Dillon, A. T. Fafarman, M. W. Barsoum, *FlatChem* **2018**, 8, 25.
- [246] J. He, P. Lyu, P. Nachtigall, *Adv. Mater.* **2018**, 4, 11143.
- [247] Y. G. Gogotsi, R. A. Andrievski, *Materials Science of Carbides, Nitrides and Borides*, Springer, Netherlands **1999**.
- [248] J. Zhang, N. Kong, S. Uzun, A. Levitt, S. Seyedin, P. A. Lynch, S. Qin, M. Han, W. Yang, J. Liu, X. Wang, Y. Gogotsi, J. M. Razal, *Adv. Mater.* **2020**, 32, 2001093.
- [249] A. Lipatov, H. Lu, M. Alhabeb, B. Anasori, A. Gruverman, Y. Gogotsi, A. Sinitskii, *Sci. Adv.* **2018**, 4, 0491.
- [250] A. Lipatov, M. Alhabeb, H. Lu, S. Zhao, M. J. Loes, N. S. Vorobeve, Y. Dall'agnese, Y. Gao, A. Gruverman, Y. Gogotsi, A. Sinitskii, *Adv. Electron. Mater.* **2020**, 6, 1702678.
- [251] G. Plummer, B. Anasori, Y. Gogotsi, G. J. Tucker, *Comput. Mater. Sci.* **2019**, 157, 168.

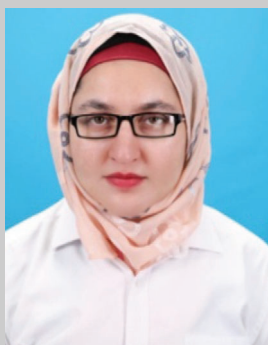
- [252] Y.-L. Hong, Z. Liu, L. Wang, T. Zhou, W. Ma, C. Xu, S. Feng, L. Chen, M.-L. Chen, D.-M. Sun, X.-Q. Chen, H.-M. Cheng, W. Ren, *Science* **2020**, 369, 670.
- [253] N. Zhang, Y. Hong, S. Yazdanparast, M. A. Zaeem, *2D Mater.* **2018**, 5, 045004.
- [254] H. Weng, A. Ranjbar, Y. Liang, Z. Song, M. Khazaei, S. Yunoki, M. Arai, Y. Kawazoe, Z. Fang, X. Dai, *Phys. Rev. B* **2015**, 92, 75436.
- [255] C. Si, K.-H. Jin, J. Zhou, Z. Sun, F. Liu, *Nano Lett.* **2016**, 4, 6584.
- [256] Khazaei, A. Lipatov, M. Alhabeb, H. Lu, S. Zhao, M. J. Loes, N. S. Vorobeve, Y. Dall'Agnese, Y. Gao, A. Gruverman, Y. Gogotsi, A. Sinitskii, Topological insulators in the ordered double transition metals M-2' M" C-2 MXenes, (M'=Mo, W; M"=Ti, Zr, Hf).
- [257] C. Si, J. You, W. Shi, J. Zhou, Z. Sun, *J. Mater. Chem. C* **2016**, 4, 11524.
- [258] Y. Liang, M. Khazaei, A. Ranjbar, M. Arai, S. Yunoki, Y. Kawazoe, H. Weng, Z. Fang, *Phys. Rev. B* **2017**, 96, 195414.
- [259] X. Jiang, A. V. Kuklin, A. Baev, Y. Ge, H. Ågren, H. Zhang, P. N. Prasad, *Phys. Rep.* **2020**, 5, 045004.
- [260] L. Dong, H. Kumar, B. Anasori, Y. Gogotsi, V. B. Shenoy, *J. Phys. Chem. Lett.* **2017**, 8, 422.
- [261] J. He, G. Ding, C. Zhong, S. Li, D. Li, G. Zhang, *Nanoscale* **2019**, 11, 356.
- [262] M. Dahlqvist, B. Alling, J. Rosén, *Phys. Rev. B* **2010**, 81, 220102.
- [263] R. A. Swalin, J. Arents, *J. Electrochem. Soc.* **1962**, 109, 308C.
- [264] Y. F. Ye, Q. Wang, J. Lu, C. T. Liu, Y. Yang, *Mater. Today* **2016**, 19, 349.
- [265] S. K. Nemani, et al., *ACS Nano* **2021**, 15, 12815.
- [266] X.-H. Zha, J.-C. Ren, L. Feng, X. Bai, K. Luo, Y. Zhang, J. He, Q. Huang, J. S. Francisco, S. Du, *Nanoscale* **2018**, 10, 8763.
- [267] L. Zhou, Y. Zhang, Z. Zhuo, A. J. Neukirch, S. Tretiak, *J. Phys. Chem. Lett.* **2018**, 9, 6915.
- [268] C. Wang, Y.-K. Guo, W.-D. Tian, K. Chen, *J. Chem. Phys.* **2019**, 150, 044907.
- [269] S. Bae, et al., *Adv. Funct. Mater.* **2021**, 31, 2100009.
- [270] X.-H. Zha, et al., *Nanoscale* **2016**, 8, 6110.
- [271] M. Naguib, J. Halim, J. Lu, K. M. Cook, L. Hultman, Y. Gogotsi, M. W. Barsoum, *J. Am. Chem. Soc.* **2013**, 135, 15966.
- [272] E. Lee, A. Vahidmohammadi, Y. S. Yoon, M. Beidaghi, D.-J. Kim, *ACS Sens.* **2019**, 4, 1603.
- [273] C.-F. Du, X. Sun, H. Yu, W. Fang, Y. Jing, Y. Wang, S. Li, X. Liu, Q. Yan, *InfoMat* **2020**, 2, 950.
- [274] E. Lee, et al., *ACS Appl. Mater. Interfaces* **2017**, 9, 37184.
- [275] X. Huo, et al., *ACS Appl. Mater. Interfaces* **2021**, 13, 11822.
- [276] R. Venkatarthick, N. Rodthongkum, X. Zhang, S. Wang, P. Pattananuwat, Y. Zhao, R. Liu, J. Qin, *ACS Appl. Energy Mater.* **2020**, 3, 4677.
- [277] Z. Wang, et al., *ACS Appl. Mater. Interfaces* **2019**, 11, 44282.
- [278] C. Wang, S. Wei, S. Chen, D. Cao, L. Song, *Small Methods* **2019**, 3, 1900495.
- [279] X. Wang, H. Li, H. Li, S. Lin, J. Bai, J. Dai, C. Liang, X. Zhu, Y. Sun, S. Dou, *J. Mater. Chem. A* **2019**, 7, 2291.
- [280] Y. Wang, W. Zheng, P. Zhang, W. Tian, J. Chen, Z. Sun, *J. Mater. Sci.* **2019**, 54, 11991.
- [281] A. Mostafaei, M. Abbasnejad, *J. Alloys Compd.* **2021**, 857, 157982.
- [282] J. Hou, K. Tu, Z. Chen, *J. Phys. Chem. C* **2016**, 120, 18473.
- [283] Z. Guo, J. Zhou, L. Zhu, Z. Sun, *J. Mater. Chem. A* **2016**, 4, 11446.
- [284] B. Cai, J. Zhou, D. Li, Z. Ao, *Appl. Surf. Sci.* **2022**, 575, 151777.
- [285] Q. Meng, J. Ma, Y. Zhang, Z. Li, A. Hu, J.-J. Kai, J. Fan, *J. Mater. Chem. A* **2018**, 6, 13652.
- [286] J. Zhu, A. Chronopoulos, J. Eppinger, U. Schwingenschlög, *Appl. Mater. Today* **2016**, 5, 19.
- [287] G. Liang, X. Li, Y. Wang, S. Yang, Z. Huang, Q. i Yang, D. Wang, B. Dong, M. Zhu, C. Zhi, *Nano Res. Energy* **2022**, 1, 9120002.
- [288] X. Li, X. Ma, Y. Hou, Z. Zhang, Y. Lu, Z. Huang, G. Liang, M. Li, Q. Yang, J. Ma, N. Li, B. Dong, Q. Huang, F. Chen, J. Fan, C. Zhi, *Joule* **2021**, 5, 2993.
- [289] S. Sardar, A. Jana, *Matter* **2020**, 3, 1397.
- [290] C. Huang, S. Shi, H. Yu, *ACS Energy Lett.* **2021**, 6, 3464.
- [291] J. Zhang, C. Huang, Y. Sun, H. Yu, *Adv. Funct. Mater.* **2022**, 32, 2113367.
- [292] L. Gao, et al., *Small Methods* **2020**, 4, 2000250.
- [293] G. Yang, J. Zhao, S. Yi, X. Wan, J. Tang, *Sens. Actuators, B* **2020**, 309, 127735.
- [294] C. Yang, Y. Luo, H. Lin, M. Ge, J. Shi, X. Zhang, *ACS Nano* **2020**, 15, 1086.
- [295] X. Ren, M. Huo, M. Wang, H. Lin, X. Zhang, J. Yin, Y. Chen, H. Chen, *ACS Nano* **2019**, 13, 6438.
- [296] C. Liu, J. Zhou, X. Li, Z. Fang, R. Sun, G. Yang, W. Hou, *Chem. Eng. J.* **2022**, 431, 133838.
- [297] Z. Li, Y. Cui, Z. Wu, C. Milligan, L. Zhou, G. Mitchell, B. Xu, E. Shi, J. T. Miller, F. H. Ribeiro, Y. Wu, *Nat. Catal.* **2018**, 1, 349.
- [298] Y. Tan, et al., *Int. J. Hydrogen Energy* **2021**, 46, 1955.
- [299] Z. Liu, J. K. El-Demellawi, O. M. Bakr, B. S. Ooi, H. N. Alshareef, *ACS Nano* **2022**, 16, 7904.
- [300] T. Su, R. Peng, Z. D. Hood, M. Naguib, I. N. Ivanov, J. K. Keum, Z. Qin, Z. Guo, Z. Wu, *ChemSusChem* **2018**, 11, 688.
- [301] C. Cui, R. Guo, H. Xiao, E. Ren, Q. Song, C. Xiang, X. Lai, J. Lan, S. Jiang, *Appl. Surf. Sci.* **2020**, 505, 144595.
- [302] H. Xiang, H. Lin, L. Yu, Y. Chen, *ACS Nano* **2019**, 13, 2223.
- [303] J. Yang, M. Naguib, M. Ghidui, L.-M. Pan, J. Gu, J. Nanda, J. Halim, Y. Gogotsi, M. W. Barsoum, *J. Am. Ceram. Soc.* **2016**, 99, 660.
- [304] P. Cai, Q. He, L. Wang, X. Liu, J. Yin, Y. Liu, Y. Huang, Z. Huang, *Ceram. Int.* **2019**, 45, 5761.
- [305] Z. W. Seh, K. D. Fredrickson, B. Anasori, J. Kibsgaard, A. L. Strickler, M. R. Lukatskaya, Y. Gogotsi, T. F. Jaramillo, A. Vojvodic, *ACS Energy Lett.* **2016**, 1, 589.
- [306] H. Zhou, Z. Chen, E. Kountoupi, A. Tsoukalou, P. M. Abdala, P. Florian, A. Fedorov, C. R. Müller, *Nat. Commun.* **2021**, 12, 5510.
- [307] X. Zhao, W. Sun, D. Geng, W. Fu, J. Dan, Y. Xie, P. R. C. Kent, W. Zhou, S. J. Pennycook, K. P. Loh, *Adv. Mater.* **2019**, 31, 1808343.
- [308] D. A. Kuznetsov, Z. Chen, P. M. Abdala, O. V. Safonova, A. Fedorov, C. R. Müller, *J. Am. Chem. Soc.* **2021**, 143, 5771.
- [309] D. A. Kuznetsov, Z. Chen, P. V. Kumar, A. Tsoukalou, A. Kierzkowska, P. M. Abdala, O. V. Safonova, A. Fedorov, C. R. Müller, *J. Am. Chem. Soc.* **2019**, 141, 17809.
- [310] S. Liu, Z. Lin, R. Wan, Y. Liu, Z. Liu, S. Zhang, X. Zhang, Z. Tang, X. Lu, Y. Tian, *J. Mater. Chem. A* **2021**, 9, 21259.
- [311] H. Pazniak, A. S. Vazhnikov, D. A. Kolosov, I. A. Plugin, A. D. Vito, O. E. Glukhova, P. M. Sheverdyayeva, M. Spasova, I. Kaikov, E. A. Kolesnikov, P. Moras, A. M. Bainyashev, M. A. Solomatin, I. Kiselev, U. Wiedwald, V. V. Sysoev, *Adv. Mater.* **2021**, 33, 2104878.
- [312] D. B. Velusamy, J. K. El-Demellawi, A. M. El-Zohry, A. Giugni, S. Lopatin, M. N. Hedhili, A. E. Mansour, E. D. i Fabrizio, O. F. Mohammed, H. N. Alshareef, *Adv. Mater.* **2019**, 31, 1807658.
- [313] T. Fan, L. Yan, S. He, Q. Hong, F. Ai, S. He, T. Ji, X. Hu, E. Ha, B. Zhang, Z. Li, H. Zhang, X. Chen, J. Hu, *Chem. Soc. Rev.* **2022**, 1, 7732.
- [314] Z. Liu, H. Lin, M. Zhao, C. Dai, S. Zhang, W. Peng, Y. Chen, *Theranostics* **2018**, 8, 1648.
- [315] A. Kis, *Nat Nanotechnol* **2012**, 7, 683.
- [316] L. Dong, H. Chu, Y. Li, X. Ma, H. Pan, S. Zhao, D. Li, *Appl. Mater. Today* **2022**, 26, 101341.
- [317] A. Rafieerad, A. Amiri, G. L. Sequiera, W. Yan, Y. Chen, A. A. Polycarpou, S. Dhingra, *Adv. Funct. Mater.* **2021**, 31, 2100015.
- [318] T. Wu, X. Pang, S. Zhao, S. Xu, Z. Liu, Y. Li, F. Huang, *Small Struct.* **2022**, 3, 2100206.
- [319] Y. Dall'Agnese, P.-L. Taberna, Y. Gogotsi, P. Simon, *J. Phys. Chem. Lett.* **2015**, 6, 2305.
- [320] X. Sun, X. He, Y. Zhu, E. Obeng, B. Zeng, H. Deng, J. Shen, R. Hu, *Chem. Eng. J.* **2023**, 451, 138985.



- [321] Y. Liu, Y. Jiang, Z. Hu, J. Peng, W. Lai, D. Wu, S. Zuo, J. Zhang, B. Chen, Z. Dai, Y. Yang, Y. Huang, W. Zhang, W. Zhao, W. Zhang, L. Wang, S. Chou, *Adv. Funct. Mater.* **2021**, 31, 2008033.
- [322] W. Zhang, J. Peng, W. Hua, Y. Liu, J. Wang, Y. Liang, W. Lai, Y. Jiang, Y. Huang, W. Zhang, H. Yang, Y. Yang, L. Li, Z. Liu, L. Wang, S.-L. Chou, *Adv. Energy Mater.* **2021**, 11, 2100757.
- [323] O. Akinola, I. Chakraborty, H. Celio, D. Akinwande, J. A. C. Incorvia, *J. Mater. Res.* **2021**, 36, 1980.
- [324] S. Liu, R. Lv, J. Wang, Y. Wang, H. Wang, H. Zhang, Y. Wang, *J. Mater. Chem. C* **2021**, 9, 16985.
- [325] A. Lipatov, M. J. Loes, N. S. Vorobeva, S. Bagheri, J. Abourahma, H. Chen, X. Hong, Y. Gogotsi, A. Sinitskii, *ACS Mater. Lett.* **2021**, 3, 1088.
- [326] K. J. Griffith, M. A. Hope, P. J. Reeves, M. Anayee, Y. Gogotsi, C. P. Grey, *J. Am. Chem. Soc.* **2020**, 142, 18924.
- [327] J. Mei, G. A. Ayoko, C. Hu, J. M. Bell, Z. Sun, *Sustainable Mater. Technol.* **2020**, 25, e00156.
- [328] E. B. Deeva, A. Kurllov, P. M. Abdala, D. Lebedev, S. M. Kim, C. P. Gordon, A. Tsoukalou, A. Fedorov, C. R. Müller, *Chem. Mater.* **2019**, 31, 4505.
- [329] P. Urbankowski, B. Anasori, K. Hantanasirisakul, L. Yang, L. Zhang, B. Haines, S. J. May, S. J. L. Billinge, Y. Gogotsi, *Nanoscale* **2017**, 9, 17722.
- [330] H. Lin, Y. Wang, S. Gao, Y. Chen, J. Shi, *Adv. Mater.* **2018**, 30, 1703284.
- [331] B. Zhou, H. Yin, C. Dong, L. Sun, W. Feng, Y. Pu, X. Han, X. Li, D. Du, H. Xu, Y. Chen, *Adv. Sci.* **2021**, 8, 2101043.
- [332] S. Manzoor, M. Abdullah, A. G. Abid, Z. Ahmad, K. M. Katubi, M. S. Al-Buriahi, S. Aman, M. Najam-ul-Haq, M. N. Ashiq, *J. Alloys Compd.* **2022**, 924, 166439.
- [333] D. i Jin, L. R. Johnson, A. S. Raman, X. Ming, Y. u Gao, F. Du, Y. Wei, G. Chen, A. Vojvodic, Y. Gogotsi, X. Meng, *J. Phys. Chem. C* **2020**, 124, 10584.
- [334] R. G. Mendes, H. Q. Ta, X. Yang, W. Li, A. Bachmatiuk, J.-H. Choi, T. Gemming, B. Anasori, L. Lijun, L. Fu, Z. Liu, M. H. Rummeli, *Small* **2020**, 16, 1907115.
- [335] N. Li, Y. Li, J. Fan, *Nanoscale* **2021**, 13, 7234.
- [336] H. Liu, H. Wang, Z. Jing, K. Wu, Y. Cheng, B. Xiao, *J. Phys. Chem. C* **2020**, 124, 25769.
- [337] W. Zhang, J. Chen, X. Wang, H. Huang, M. Yao, *ACS Appl. Nano Mater.* **2022**, 5, 2358.
- [338] C. Chen, X. Xie, B. Anasori, A. Sarycheva, T. Makaryan, M. Zhao, P. Urbankowski, L. Miao, J. Jiang, Y. Gogotsi, *Angew. Chem., Int. Ed.* **2018**, 57, 1846.
- [339] W.-H. Li, J.-J. Wu, L. Wu, B.-D. Zhang, H.-G. Hu, L. Zhao, Z.-B. Li, X.-F. Yu, Y.-M. Li, *Biomaterials* **2021**, 273, 120788.
- [340] I. Hussain, S. Iqbal, T. Hussain, Y. Chen, M. Ahmad, M. S. Javed, A. Alfantazi, K. Zhang, *J. Mater. Chem. A* **2021**, 9, 17790.
- [341] I. Hussain, S. Iqbal, T. Hussain, W. L. Cheung, S. A. Khan, J. Zhou, M. Ahmad, S. A. Khan, C. Lamiel, M. Imran, A. Alfantazi, K. Zhang, *Mater. Today Phys.* **2022**, 23, 100655.
- [342] I. Hussain, S. G. Mohamed, A. Ali, N. Abbas, S. M. Ammar, W. Al Zoubi, *J. Electroanal. Chem.* **2019**, 837, 39.
- [343] I. Hussain, T. Hussain, S. B. Ahmed, T. Kaewmaraya, M. Ahmad, X. i Chen, M. S. Javed, C. Lamiel, K. Zhang, *J. Power Sources* **2021**, 513, 230556.
- [344] I. Hussain, T. Hussain, S. Yang, Y. Chen, J. Zhou, X. Ma, N. Abbas, C. Lamiel, K. Zhang, *Chem. Eng. J.* **2021**, 413, 127570.
- [345] N. Abbas, I. Shaheen, I. Hussain, C. Lamiel, M. Ahmad, X. Ma, A. Qureshi, J. H. Niazi, M. Imran, M. Z. Ansari, K. Zhang, *J. Alloys Compd.* **2022**, 919, 165701.
- [346] Z. Cui, Y. Zhang, R. Xiong, C. Wen, J. Zhou, B. Sa, Z. Sun, *Nanoscale Adv* **2022**, 4, 5144.
- [347] J. He, P. Lyu, P. Nachtigall, *J. Mater. Chem. C* **2016**, 4, 11143.
- [348] Q. He, H. Hu, J. Han, Z. Zhao, *Mater. Lett.* **2022**, 308, 131100.
- [349] R. Syamsai, J. R. Rodriguez, V. G. Pol, Q. Van Le, K. M. Batoo, S. F. Adil, S. Pandiaraj, M. R. Muthumareeswaran, E. H. Raslan, A. N. Grace, *Sci. Rep.* **2021**, 11, 688.
- [350] Q. Ma, Z. Zhang, P. Kou, D. Wang, Z. Wang, H. Sun, R. Zheng, Y. Liu, *J. Colloid Interface Sci.* **2022**, 617, 147.
- [351] R. He, D. Xu, B. Cheng, J. Yu, W. Ho, *Nanoscale Horiz.* **2018**, 3, 464.
- [352] S. Fatima, M. W. Hakim, D. Akinwande, S. Rizwan, *Mater. Today Phys.* **2022**, 26, 100730.
- [353] O. Mashtalir, K. M. Cook, V. N. Mochalin, M. Crowe, M. W. Barsoum, Y. Gogotsi, *J. Mater. Chem. A* **2014**, 2, 14334.
- [354] K. Wang, Y. Zhou, W. Xu, D. Huang, Z. Wang, M. Hong, *Ceram. Int.* **2016**, 4, 8419.
- [355] A. Lipatov, M. Alhabeb, M. R. Lukatskaya, A. Boson, Y. Gogotsi, A. Sinitskii, *Adv. Electron. Mater.* **2016**, 2, 11143.
- [356] M. N. Abdelmalak, *Ph.D. Thesis*, Drexel University, xx xx **2014**.
- [357] M. W. Barsoum, R. Syamsai, J. R. Rodriguez, V. G. Pol, Q. V. Le, K. M. Batoo, S. F. Adil, S. Pandiaraj, M. R. Muthumareeswaran, E. H. Raslan, A. N. Grace **2013**.
- [358] F. Cao, Y. Zhang, H. Wang, K. Khan, A. K. Tareen, W. Qian, H. Zhang, H. Ågren, *Adv. Mater.* **2022**, 34, 2107554.
- [359] R. Morales-Salvador, Á. Morales-García, F. Viñes, F. Illas, *Phys. Chem. Chem. Phys.* **2018**, 20, 17117.
- [360] U. Yorulmaz, İ. Demiroğlu, D. Çakir, O. Gülseren, C. Sevik, *J. Phys.: Condens. Matter* **2020**, 2, 032006.
- [361] J. Guo, H. Fu, G. Zou, Q. Zhang, Z. Zhang, Q. Peng, *J. Alloys Compd.* **2016**, 684, 504.
- [362] Z. Fu, H. Zhang, C. Si, D. Legut, T. C. Germann, Q. Zhang, S. Du, J. S. Francisco, R. Zhang, *J. Phys. Chem. C* **2018**, 122, 4710.
- [363] M. Ashton, K. Mathew, R. G. Hennig, S. B. Sinnott, *J. Phys. Chem. C* **2016**, 120, 3550.
- [364] H.-T. Yan, X.-H. Li, M.-Z. Liu, X.-H. Cui, S.-S. Li, H.-L. Cui, *Vacuum* **2022**, 207, 111094.
- [365] V. Shukla, N. K. Jena, S. R. Naqvi, W. Luo, R. Ahuja, *Nano Energy* **2019**, 58, 877.
- [366] H. Wu, Z. Guo, J. Zhou, Z. Sun, *Appl. Surf. Sci.* **2019**, 488, 578.
- [367] Á. Morales-García, A. Fernández-Fernández, F. Viñes, F. Illas, *J. Mater. Chem. A* **2018**, 6, 3381.
- [368] N. Li, X. Chen, W.-J. Ong, D. R. Macfarlane, X. Zhao, A. K. Cheetham, C. Sun, *ACS Nano* **2017**, 11, 10825.
- [369] A. D. Handoko, K. H. Khoo, T. L. Tan, H. Jin, Z. W. Seh, *J. Mater. Chem. A* **2018**, 6, 21885.
- [370] S. Ma, D. Yuan, Z. Jiao, T. Wang, X. Dai, *J. Phys. Chem. C* **2017**, 121, 24077.
- [371] A. Junkaew, R. Arroyave, *Phys. Chem. Chem. Phys.* **2018**, 20, 6073.
- [372] M. Khazaei, M. Arai, T. Sasaki, C.-Y. Chung, N. S. Venkataraman, M. Estili, Y. Sakka, Y. Kawazoe, *Adv. Funct. Mater.* **2013**, 23, 2185.
- [373] S. Ma, X. Fan, Y. An, D. Yang, Z. Luo, Y. Hu, N. Guo, *J. Mater. Sci.* **2019**, 54, 11378.
- [374] X. Bai, C. Ling, L. Shi, Y. Ouyang, Q. Li, J. Wang, *Sci. Bull.* **2018**, 63, 1397.
- [375] D. Wijethunge, L. Zhang, A. Du, *J. Mater. Chem. C* **2021**, 9, 11343.
- [376] A. S. Ingason, M. Dahlqvist, J. Rosén, *J. Phys.: Condens. Matter* **2016**, 28, 433003.
- [377] B. Unnikrishnan, C.-W. Wu, A. Sangili, Y.-J. Hsu, Y.-T. Tseng, J. Shanker Pandey, H.-T. Chang, C.-C. Huang, *J. Colloid Interface Sci.* **2022**, 628, 849.
- [378] P. Ridley, C. Gallano, R. Andris, C. E. Shuck, Y. Gogotsi, E. Pomerantseva, *ACS Appl. Energy Mater.* **2020**, 3, 10892.
- [379] M. Tao, G. Du, T. Yang, W. Gao, L. Zhang, W. Du, J. Jiang, S. Bao, M. Xu, *J. Mater. Chem. A* **2020**, 8, 3018.
- [380] M. Ahmad, I. Hussain, T. Nawaz, Y. Li, X. Chen, S. Ali, M. Imran, X. Ma, K. Zhang, *J. Power Sources* **2022**, 534, 231414.



**Karim Khan** received his B.Sc. degree (2005) from Gomal University, M.Sc. (2009) in Physics from University of Peshawar, M.Phil. (2012) from University-of-the-Punjab, Pakistan. He obtained his Ph.D. (2016) from Chinese-Academy-of-Sciences and he also served as a postdoctoral-fellow (2017–2021) in Shenzhen university and Dongguan university of Technology, China. His current research focuses on 2D materials applications in energy producing/storage devices and sensors. Total citations of all his 189-publications and 4-patents are more than 5,000-times, and his H-index is 35. He has received several awards and being among the top 2% highly-cited researchers-worldwide.



**Ayesha Khan Tareen** is a post-doctoral fellow in Shenzhen University. She received her Ph.D. (Physical Chemistry/Materials) in 2018 from Ningbo Institute of Material Technology and Engineering, Chinese Academy of Sciences, M.Phil. (Analytical Chemistry) in 2015 from “*The Islamia University of Bahawalpur*” and B.Sc. (Honors) in Chemistry in 2012 from Government College University Lahore, Pakistan. Her Research interests are in 2D-materials and transition metal nitride material synthesis and applications in different directions especially for photo (electro)-catalysts, fuel cell, batteries, and solar cell. The total citations of all his publications are more than 2,600 times, and her H index is 24.



**Waqas Ahmad** is a postdoctoral research associate in the Institute of Fundamental and Frontier Sciences at University of Electronic Science and Technology of China. Subsequently, he is a visiting research fellow in Songshan Lake Materials Laboratory, Dongguan, China. He received his Ph.D. in Optical Engineering from Shenzhen University, Shenzhen, China. During his Ph.D. studies, his research was focused on the 2D/2D vdWs heterostructures and their application in photodetectors. Currently, his research focuses on the interfacial engineering in 2D vdWs heterosystems for next generation optoelectronics.



**Iftikhar Hussain** is a postdoc in the City University of Hong Kong under the supervision of Prof. Kaili Zhang. He received his M.S. degree from Yeungnam University, South Korea and Ph.D. from City University of Hong Kong. He also went as a visiting researcher at Drexel University, USA under the supervision of Prof. Yury Gogotsi. His current research focuses on the development of electrode materials for energy storage/conversions.



**Mujeeb U. Chaudhry** is an associate-professor in Durham University, UK. His Ph.D. was in Organic-Semiconductors and Electronics from Johannes-Kepler University of Linz (2011). He then undertook postdoctoral research positions at University of Linz and then at University of Queensland (light-emitting transistors, charge transport, alignment an order, organic optoelectronics), prior to joining Durham University in 2016 on a junior fellowship (funded through Marie-Curie Actions and Institute of Advanced Studies, Durham University). He has authored more than 55 journal articles, reviews, and book chapters. He is also acting as a referee for numerous high-impact journals as well as national and international grant awarding bodies.



**Asif Mahmood** received his Ph.D. in Materials Science and Engineering from Peking University, and is a Chancellor's Research Fellow at the University of Technology Sydney. His research focuses on nano-materials for electrochemical processes and rechargeable batteries, resulting in over 80 publications in renowned journals. He has received several awards, including recognition as a Higher Education Rising Star in 2020 and being among the top 2% highly cited researchers worldwide.



**Muhammad Farooq Khan** is an assistant professor at Sejong University, Republic of Korea. He earned his Ph.D. (Physics) from Sejong University in 2018. After that, he was a postdoc fellow at Yonsei University in 2019. His research primarily focusing on nanofabrication of electronic, memory, and energy harvesting devices manifested by two-dimensional layered semiconductor materials. His contributions extend beyond academia; he successfully won two research grants from National Research Foundation (NRF) of South Korea and has authored a book chapter on "2D Material Photonics and Optoelectronics." In addition, he is serving as a referee for various scientific journals ensuring the dissemination of high-quality research.



**Han Zhang** received his Ph.D. from Nanyang Technological University (2010). He is currently a director of Shenzhen Key Laboratory of 2D-materials and Devices, and the Shenzhen Engineering Laboratory of Phosphorene and Optoelectronics, Shenzhen University. His current research focuses on the ultrafast and nonlinear photonics of 2D-materials. He is also a Highly Cited Researcher of the Clarivate Analytics (2018–2019). He was awarded Fellow of Optical Society of America (2019). In the past five years, Prof. Han Zhang's group published more than 500-papers, and his total citations of all his publications are more than 79,000 times, and his H-index is 149.





**Zhongjian Xie** is a researcher of Shenzhen Children's Hospital, Clinical Medical College of Southern University of Science and Technology, Shenzhen University. He is an expert on tumor theranostics. He has published over 80 peer-review articles. All of his publications have received >5500 citations, with an H-index of 35. He has been chosen as world top 2% scientist.